Surface Science Reports 73 (2018) 233–264

Contents lists available at ScienceDirect

Surface Science Reports

journal homepage: www.elsevier.com/locate/surfrep

Water confined in two-dimensions: Fundamentals and applications

Pantelis Bampoulis *, Kai Sotthewes, Edwin Dollekamp, Bene Poelsema

Physics of Interfaces and Nanomaterials, MESA+ Institute for Nanotechnology, University of Twente, P.O.Box 217, 7500AE Enschede, the Netherlands

ARTICLE INFO

Article history:
Received 21 June 2018
Revised 30 August 2018
Accepted 31 August 2018
Available online 15 September 2018

2010 MSC:
00-01
99-00

Keywords:
Confined water
Two-dimensional ice
Intercalation
Diffusion
Graphene

ABSTRACT

The behavior of water in close proximity to other materials under ambient conditions is of great significance due to its importance in a broad range of daily applications and scientific research. The structure and dynamics of water at an interface or in a nanopore are often significantly different from those of its bulk counterpart. Until recently, experimental access to these interfacial water structures was difficult to realize. The advent of two-dimensional materials, especially graphene, and the availability of various scanning probe microscopies were instrumental to visualize, characterize and provide fundamental knowledge of confined water. This review article summarizes the recent experimental and theoretical progress in a better understanding of water confined between layered Van der Waals materials. These results reveal that the structure and stability of the hydrogen bonded networks are determined by the elegant balance between water-surface and water-water interactions. The water-surface interactions often lead to structures that differ significantly from the conventional bilayer model of natural ice. Here, we review the current knowledge of water adsorption in different environments and intercalation within various confinements. In addition, we extend this review to cover the influence of interfacial water on the two-dimensional material cover and summarize the use of these systems in potential novel applications. Finally, we discuss emerged issues and identify some flaws in the present understanding.

1. Introduction

Water covers most surfaces under atmospheric conditions. It exists in many states (of aggregation), such as vapor, liquid and several amorphous and crystalline phases [1–4]. Water is also abundant at interfaces and within confined environments. The structure of the first water layer at interfaces defines several microscopic phenomena, including corrosion, fluid flow, catalysis, lubrication and interfacial chemistry [5–9]. Understanding the vast amount of ice phases and the dynamics of ice structures is thus crucial to further advance in many fields including life sciences, environmental sciences, condensed matter physics and nanofluidics. For example, the way water diffuses into nanopores defines the functionality of proteins and membranes [10]. Understanding the boundary slip conditions is of particular interest in nanofluidics [11]. Water trapped between layered two-dimensional (2D) materials, influences the electronic properties and induces doping, which can affect device functionality [12,13].

The physical properties of confined water are often dramatically different from those of their bulk counterpart, owing to perturbations induced by the interface. These properties strongly depend on the confinement dimensions and interface structure as well as temperature and pressure [14]. These properties include nontetrahedral bonding geometries, complex phase behavior and phase transitions, and anomalous self-diffusion [15–28]. For example, inside hydrophobic carbon nanotubes, water exhibits fast motion [29], as well as novel phases that strongly depend on the confinement dimensions [30,31]. Much of the knowledge is based on molecular dynamic (MD) simulations and density functional theory (DFT) calculations. Despite significant efforts, a systematic understanding of the influence of confinement on this rich behavior is still lacking [32,33]. Conflicting results arise from the use of different calculation methods and many of these theoretical observations are still under discussion [21,30,34]. High quality experiments are indispensable to foster this area of research. However, owing to the dynamic nature of water films at ambient conditions, direct visualization remains challenging. For that reason, most experimental knowledge of the molecular structure and properties of water at surfaces has been obtained under ultra-high vacuum (UHV) conditions and at cryogenic temperatures. Several studies have focused on the adsorption of water

* Corresponding author.
E-mail address: p.bampoulis@utwente.nl (P. Bampoulis).

https://doi.org/10.1016/j.surfrep.2018.09.001
0167-5729/

on close-packed metal surfaces and have obtained useful information on ice nucleation and growth processes [35–37]. However, the behavior of water at ambient conditions and especially when confined in nanopores could be significantly different and the existing knowledge might not be transferable [14]. To make things even worse, the confinement walls pose another barrier in imaging and characterizing these water structures.

We distinguish two types of geometric confinement, i.e., one-dimensional, for example water inside carbon nanotubes, and two-dimensional, e.g., when water is trapped between two surfaces that are brought closely together. Two dimensional confinement can be further defined, depending on the hydrophobicity of the two surfaces, i.e., hydrophobic-hydrophobic, hydrophobic-hydrophilic and hydrophilic-hydrophilic. A complete understanding of the structure of water confined between subnanometer spaced flat walls requires information on; the molecular structure of the first water layer, molecular dynamics, identification of multilayer growth mechanisms and knowledge of the influence of other environmental parameters such as temperature and pressure. Before proceeding with the discussion of the growth and structure of water clusters within confined geometries, we briefly discuss the understanding on the water-water intermolecular hydrogen bonding as well as some relevant examples of the adsorption of water on solid substrates.

1.1. The hydrogen bond

The length of the O—H bond of an isolated water molecule amounts to 0.957 Å; the two H-atoms and the two electron lone pairs assume a tetrahedral coordination around the oxygen atom. The H—O—H bond angle is 104.5°. A dipole moment of 1.85 D [38] results from the electron polarization with electron density enhancement on the oxygen atom and reduction on the hydrogen atoms. The electronegative oxygen atom and the electropositive hydrogen atom of nearby water molecules attract each other and form the so called hydrogen bond (H-bond), see Fig. 1a. In contrast to the strength of the covalent O—H bond in water, cf. 5.1 eV, the strength of the intermolecular hydrogen bond is significantly weaker, ranging from 0.1 to 0.3 eV. Its exact value depends on the geometry of the water cluster and the bond length. Typically, a strong hydrogen bond results in shortening of the O—O distance and a small elongation (thus weakening) of the O—H bond [35,39,40].

H_2O molecules in naturally occurring I_h-ice crystals arrange in a tetrahedrally bonded hexagonal close-packed structure. This way the electron-electron repulsion is minimized. Fig. 1b and c show the schematic representation of the molecular structure of natural ice (side and top views). The basal plane of I_h-ice is puckered, forming a bilayer structure. In each bilayer, water molecules that are hydrogen bonded with each other form hexagonal rings. Each molecule forms hydrogen bonds with the three nearest neighbors located, 0.96 Å, below it and a fourth H-bond with an oxygen atom located in the above bilayer, displaced by 2.76 Å. This arrangement of water molecules to form the I_h-ice crystals is the starting point for understanding water adsorption on surfaces.

1.2. Water on close packed metal surfaces

The adsorption of water on solid surfaces has attracted significant interest, owing to its importance across various fields (water is involved in many physical and chemical processes) and its complexity. Relevant information regarding water adsorption and the first ice monolayer on transition metal surfaces has been obtained from ultra-high vacuum (UHV) experiments at cryogenic temperatures by scanning tunneling microscopy (STM) and spectroscopic tools. Extended reviews on this matter can be found for instance in Refs. [9,35–37,41–43]. Here, we limit our discussion on the basic principles that govern the growth and structure of water on metal substrates under UHV and low temperature (LT) conditions, since many of the concepts introduced in this field are relevant to confined water under ambient temperature.

On most metal surfaces the balance between water-metal and water-water interactions defines the form and stability of the water structure [35,36,44]. The adsorption energy of water and kinetic effects can play a prominent role in the determination of the final structure. The adsorption energy is often comparable to the water-water hydrogen bond and kinetic effects can trap water into metastable phases with very long lifetimes. Numerous studies have focused on water adsorption and ice growth on close-packed transition metal surfaces [35,36,41,42,45–47]. Metals with a lattice constant close to that of hexagonal ice were assumed to be ideal templates, based on the conjecture that a lattice match between the

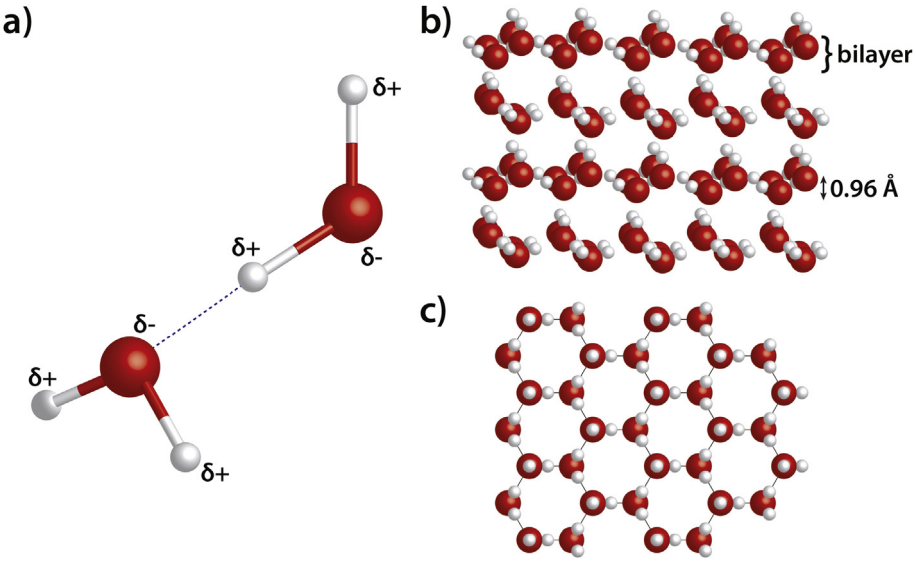

Fig. 1. (a) Hydrogen bond (dotted line) between two water molecules. (b) Side and (c) top view of the structure of I_h-ice (white and red spheres represent hydrogen and oxygen atoms, respectively). (For interpretation of the references to color in this figure legend, the reader is referred to the Web version of this article.)

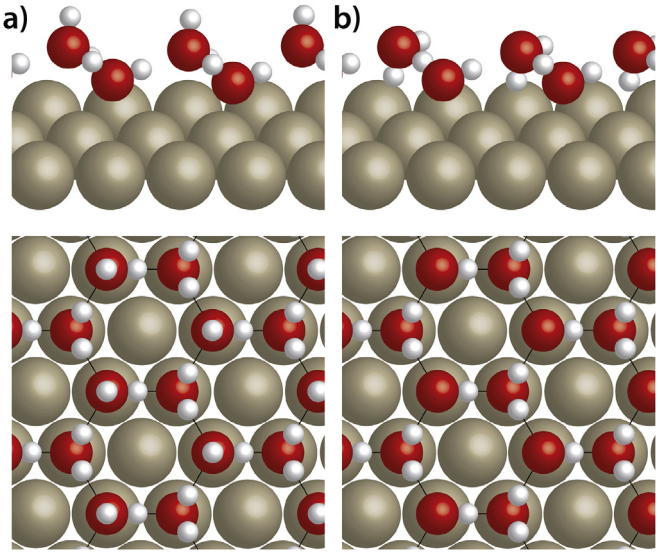

Fig. 2. Side and top views of the (a) H-up and (b) H-down classical $\sqrt{3}$ bilayer models on a close-packed metal surface (white, red and gray spheres represent hydrogen, oxygen and metal atoms, respectively). (For interpretation of the references to color in this figure legend, the reader is referred to the Web version of this article.)

hexagonal ice (0001) plane and the metal surface would facilitate an ice-like water structure [36,42,47].

In an ice-like layer, the water molecules assume a honeycomb configuration with a $(\sqrt{3}\times\sqrt{3})R30°$ (hereby referred as $\sqrt{3}$) arrangement [35]. In such an arrangement, half of the water molecules are bonded to the surface via the oxygen atom. The hydrogen bonded network is completed by the rest of the water molecules that either point their hydrogen toward (H-down) or away (H-up) from the surface, see Fig. 2. In ice-like layers, the oxygen atoms form a bilayer. In order to preserve the tetrahedral bonding motif of I_h-ice, the honeycomb network consists of two hexagonal sublattices that are vertically displaced from each other by 0.96 Å [1]. However, recent progress has called into question whether an ice-like water layer exists. First-principle calculations have revealed that a nontetrahedrally bonded water network is often energetically more favorable than the conventional bilayer ice model [37,48]. In fact, further progress revealed that water adsorption on metal surfaces is a highly complicated progress, where the final structure is influenced by both the surface chemistry and symmetry. Ice geometries that deviate from the typical $\sqrt{3}$ model of Fig. 2 are rather the norm.

A characteristic example where it was initially thought that the first wetting layer adopts an ice-like structure, due to the very small lattice mismatch with the I_h-ice (3.7%), is the Ru(0001) surface [36,47,49]. However, owing to water dissociation on Ru(0001) surface [48] (activation energy of 0.5 eV [50]), the first wetting layer actually consists of coplanar hexagonal rings composed of hydrogen bonded water molecules and hydroxyl groups [48,51,52]. This structure is significantly different from the conventional bilayer model. The extra hydrogen atoms occupy positions at the center of the rings. Another important example is ice grown on a Pt(111) surface (Pt is an important electrode in electrochemical and catalytic processes), where it was initially reported that the first water monolayer forms a $\sqrt{3}$ network [41,53]. Nonetheless, recent studies have revealed that the structure of the first monolayer on Pt(111) depends on the growth conditions. The two most stable phases are the $(\sqrt{37}\times\sqrt{37})R25.3°$ (hereby referred as $\sqrt{37}$) and the $(\sqrt{39}\times\sqrt{39})R16.1°$ (hereby referred as $\sqrt{39}$) [54–61]. Both phases consist of a 'flat-lying' (plane parallel to the surface) hexagonal water ring adsorbed at Pt atop sites, that is surrounded by three heptagonal and three pentagonal water rings. In the case of the $\sqrt{37}$ layer, the unit cell is completed by the adsorption of two additional water molecules [60]. In the $\sqrt{39}$ structure, 4 additional molecules complete the first layer and one extra molecule adsorbs at a specific location in the second layer [58,60]. Interestingly, in these structures, the water molecules form four bonds. They are fully coordinated and thus contain no dangling OH bonds (except for the second layer water molecule of the $\sqrt{39}$ phase), suggesting a hydrophobic character. After all, in hydrophilic surfaces, complete wetting means that a water molecule will prefer to bond with the surface rather than with other water molecules. Therefore, the structure of water near the surface is substantially influenced by the substrate, which results in novel bonding geometries.

In the case of a hydrophobic substrate, the weak interaction of water with the surface and near-surface stratification can also lead to the growth of ice films with a nontetrahedral geometry and remarkable properties [62,63]. For instance, Kimmel et al. [64] observed metastable crystalline ice grown at 100–135 K on the graphene/Pt(111) surface. In this ice phase, two flat hexagonal layers of water molecules are placed on top of each other. Each molecule forms three in-plane hydrogen bonds with its nearest neighbor and one out of plane hydrogen bond with the molecule in the opposite layer. This leads to maximization of the number of hydrogen bonds and a low surface energy. Similar ice films have also been observed on an Au(111) substrate [65] at cryogenic temperatures.

On many metal surfaces, the first water layer has no dangling OH groups sticking out of its surface. The lack of dangling bonds destabilizes further water adsorption on top of the monolayer without restructuring. Therefore, the first water layer does not wet when it tightly bonds to the metal surface [66–68]. Further water adsorption forms 3D clusters on top of the first layer [67,68]. Eventually, it is expected that further water adsorption would lead to a reconstruction of the first monolayer in order to accommodate 3D growth. The restructuring could involve a 'flipping' mechanism of the H-down molecules to an H-up arrangement [69]. This mechanism provides dangling OH bonds that can facilitate layer-by-layer growth. The authors of ref [69] proposed that such a flipping mechanism can be induced by permanent electric multipole moments of the adsorbates.

1.3. Adsorption at ambient conditions

Adsorption of water on solid surfaces and at atmospheric conditions is important in several environmental and industrial processes. The investigation of thin water layers at ambient conditions is a rather challenging task because of the high vapor pressure of water at room temperature. The properties of water structures over large areas have been probed by spatially averaging optical methods [70–73]. However, visualization of the molecular structure of the first water layer on a surface is still a challenging task. This is mainly due to the dynamic nature of water at ambient conditions and the inability of scanning probe techniques to probe such molecular structures without damaging them [41,74,75]. It is thus not surprising that our knowledge on water adsorption on surfaces other than metals is somehow limited. In this section, we will briefly describe water adsorption on key substrates (mica and graphite), that have been used as substrates or covers for confined water studies. For complete and comprehensive reviews on the adsorption of water on solid surfaces under ambient conditions we refer the reader to refs [43,73,76].

1.3.1. Adsorption on mica

A material that has attracted considerable attention for ice nucleation and highly relevant to this review, is mica [77–79]. The most common type of mica is muscovite. Muscovite mica has a layered aluminosilicate structure with the formula $KAl_2(Al,Si_3)O_{10}(OH)_2$. Interlayer potassium cations hold the mica layers together and balance the negative charge of the mica crystal. After cleavage of the mica, half of the potassium ions remain on each of the two created surfaces in order to preserve charge balance.

Mica is hydrophilic and it is covered by a thin water film at ambient conditions. Using ellipsometry at room temperature, Beaglehole et al. [70,80] measured the correlation between the thickness of the adsorbed water film and the relative humidity (RH). They suggested that thicker water films are fluid-like on mica. By utilizing scanning polarization force microscopy (SPFM), Salmeron and co-workers [71,81–83] imaged a thin water film on mica under ambient conditions. They observed metastable island structures that disappeared soon after scanning, due to evaporation. These islands were interpreted as a second water layer on top of a monolayer of water on mica. The islands exhibited crystal-like properties. Their boundaries have polygonal shapes with angles of about 120°. Evidence for epitaxial growth was found by comparing the direction of the ice boundaries to the mica crystallographic orientation.

Odelius et al. [84], using molecular dynamics (MD) simulations, found that the first water monolayer is a fully connected hydrogen bonded network epitaxially grown on mica. Surprisingly, the authors found that the ice structure had no free OH bonds sticking out of the ice surface (the model was later optimized by Feibelman [85] to include the role of the K^+ ions). Their findings were confirmed a year later by Salmeron's group [71], by directly studying D_2O on mica with sum-frequency-generation (SFG) vibrational spectroscopy. In their SFG investigation of D_2O water on mica, they found almost no signal in the free OD stretch region around 2740 cm^{-1}. These results indicate that the ice layer possesses a net dipole moment and the positive side points toward the mica surface. The SPFM investigation revealed that the surface potential of the mica surface covered with a monolayer water film is decreased compared to dry mica, in line with the absence of free OH bonds of the ice surface. Interestingly, multilayer films show a potential increase as well as an appearance of the free OD stretch signal at SFG, indicating the presence of uncoordinated OD/OH bonds.

1.3.2. Adsorption on graphite

The structure of water on hydrophobic surfaces is of fundamental importance for the understanding of hydrophobic interactions and technological relevance in, for instance, the oil industry. In contrast to hydrophilic substrates where a hydrogen bonded water network is often observed, on hydrophobic surfaces, interfacial water molecules form structures with unsaturated H-bonds [5,86]. The non-polar nature of a hydrophobic substrate implies that complete wetting is not allowed. A characteristic hydrophobic substrate that has been widely used for SPM investigations due to both flatness and ease of preparation, is highly oriented pyrolytic graphite (HOPG, i.e., a stack of graphene layers bonded via Van der Waals forces). Water adsorption on HOPG has been explored with the use of several AFM modes [87,88]. Zheng et al. [89] demonstrated that the presence of hydrophilic patches (graphene oxides) on HOPG promotes condensation of water droplets and these act as seeds for ice growth at ambient conditions. Their AFM study revealed several ice phases such as amorphous ice, cubic ice (I_c) and I_h-ice. Gil et al. [90] showed that the AFM tip can induce water condensation on HOPG. They observed the formation of flat and dynamic, 5 nm high, circular islands during scanning at a relative humidity (RH) above 90%. Interestingly these islands transform into 2 nm high layers oriented along the high symmetry directions of HOPG. This height corresponds to six puckered bilayers of I_h-ice and therefore these islands were suggested to be ice-like [90,91]. Yang et al. [92] used 4D ultrafast electron crystallography to study the graphite-water interface. The growth of layered water structures on graphite is thought to be induced by hydrophilic defects on the surface and promoted by scanning with a hydrophilic tip. High resolution AFM images of water on HOPG, taken under ambient conditions, revealed the presence of a layer with a lattice periodicity close to the bilayer ice lattice constant [93]. However, the exact influence of the AFM tip on these structures remains largely unexplored.

2. Graphene template: experimental details

The preparation of atomic layer(s) thick graphitic films, or graphene, by mechanical exfoliation [94–96] and the study of their extraordinary electronic properties has revolutionized the study of 2D materials. Next to its electronic properties, graphene has very remarkable mechanic properties too. The latter are instrumental in the study of confined water structures. Graphene, a single layer of graphite consists of a single atom-thick plane of carbon atoms. The carbon atoms in graphene arrange themselves in a honeycomb network, with a unit cell consisting of two atoms. The s, p_x and p_y orbitals on each carbon atom hybridize to form strong 'sp^2' bonds. The remaining p_z orbital on each atom makes up the π-bond. The hybridization of the π-bonds results in the formation of the π-band (valence band) and the π^*-band (conduction band), which determine the electronic structure of graphene [97].

The electrons in graphene behave as massless relativistic particles (such as photons or neutrinos) that are described by the Dirac equation ($H = u_F \sigma p$, where p is the momentum vector measured from the K-points, $p = \hbar k$, σ the Pauli spin matrices and u_F the Fermi velocity). In graphene the electrons behave similar to photons, their Fermi velocity is of the order of 10^6 m/s, i.e., just 300 times lower than the speed of light. Despite the fact that the charge carriers in graphene act as relativistic particles and are described by the Dirac equation, they have no relativistic nature. Instead, the periodic potential of the graphene lattice interacts with them, creating new quasiparticles. These quasiparticles, can be imagined as electrons losing their rest mass, m_0, and are often called massless Dirac fermions [95,97,98]. The conduction and valence bands of graphene touch at the K and K' points of the Brillouin zone, these points are also referred to as the Dirac points of graphene. Moreover, free-standing, mono-layer graphene has its Fermi level located exactly in the crossing point of its Dirac cones. This results in a fully filled valence band, an empty conduction band and no band gap. Therefore, it can be qualified as a zero-band gap semiconductor or a zero-overlap semimetal.

Owing to its honeycomb lattice and unique electronic structure, graphene has some exceptional properties. It has a very high conductivity parallel to its plane and can sustain current densities that are orders of magnitude higher than metals [95,99]. Furthermore, it is the strongest and at the same time the thinnest known material. Graphene monolayers have a Young's modulus of around 1 TPa and a fracture strength of 130 GPa, while still being extremely flexible [100]. Graphene has also very high in-plane thermal conductivity which can be up to about 5000 $Wm^{-1}K^{-1}$ at room temperature [101]. In addition, it is impermeable to gases and small molecules, making it an ideal membrane [102].

Thanks to these remarkable properties, graphene can be used as an ultrathin coating to cover water films on various solid substrates [103]. The seminal work done by Xu et al. [75] provided the first demonstration that graphene can trap and protect water films when deposited on a supporting mica substrate at ambient condi-

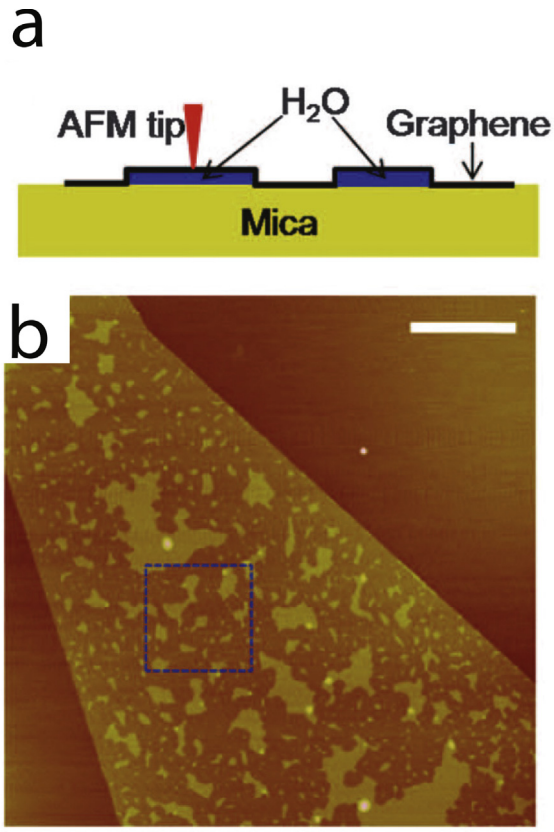

Fig. 3. (A) A schematic of how graphene locks the first water adlayer on mica into fixed patterns and serves as an ultrathin coating for AFM. (B) AFM image of a monolayer graphene sheet deposited on mica at ambient conditions, scale bar indicates 1 μm. Reprinted with permission from Ref. [75]. Copyright 2010, American Association for the Advancement of Science.

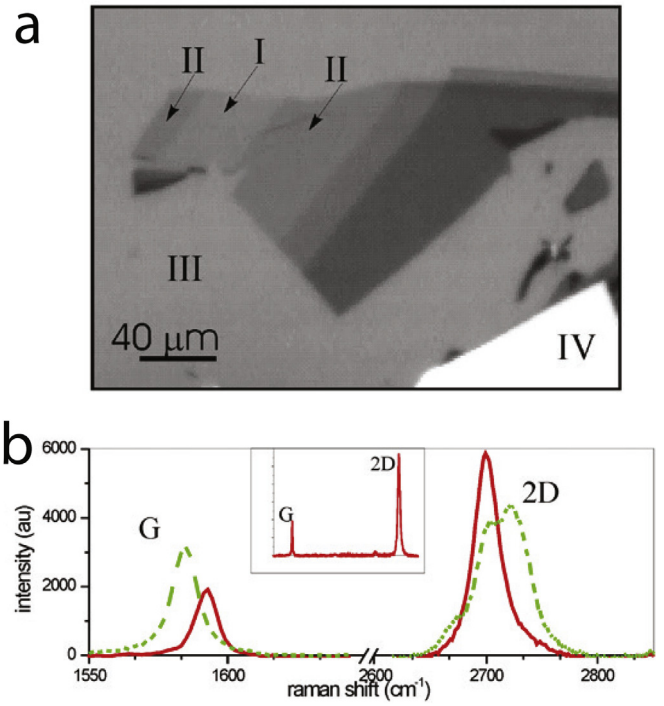

Fig. 4. (a) Optical micrograph of graphene flakes of different thicknesses on a mica substrate. Monolayer (I) and bilayer (II) graphenes appear darker than mica (III). Somewhat thicker graphene flakes appear even darker and much thicker flakes (IV) appear brighter than the background (the white color is due to camera saturation). (b) G and 2D peaks of Raman spectra taken on a monolayer (I-solid line) and bilayer (II-dashed line). The mica background intensity is subtracted. The narrow and symmetric profile of the 2D peak confirms the monolayer thickness. The insert shows the full scale Raman spectrum for the monolayer. Reprinted with permission from Ref. [110]. Copyright 2010, AIP Publishing. (For interpretation of the references to color in this figure legend, the reader is referred to the Web version of this article.)

tions. A schematic of how graphene traps water layers on mica is shown in Fig. 3a. Because of graphene's unusual flexibility, it conforms to these water structures with high precision and allows for direct imaging using scanning probe techniques, see Fig. 3b. Covering water molecules pre-adsorbed on a substrate with graphene allows for direct investigation of their structure and properties by the use of scanning probe microscopies. The impermeability of graphene even to small molecules [102] prohibits direct evaporation and condensation of water from, respectively on the interface and prevents the SPM tip from perturbing the trapped water. In addition, the highly anisotropic nature of graphene's thermal conductivity, in which the in-plane value (2000–5000 W/Km) outweighs by far the out-of-plane (6 W/Km) thermal conductivity [104], provides an extra protection for the confined water from environmental thermal effects.

In the original work done by Xu et al. [75], a monolayer graphene is used as an ultrathin coating to cover water adlayers on a mica substrate and enable an AFM investigation. Subsequent experiments involving variation of the relative humidity and temperature reveal intercalation of water, nucleation of ice and multilayer growth [105–107]. In this approach, the tape method [75,108] and the tape-free method [109] are used for graphene deposition on the supporting substrate. Soon afterwards, Rezania et al. [109] pointed out the need for using tape free methods to investigate confined water structures, such that interfacial contamination due to tape remnants is largely avoided. In the tape free method, loose flakes are picked up from the freshly cleaved surface of HOPG, with the use of a tweezer. The extracted graphite flakes are then gently pressed on top of the substrate of choice, e.g., mica. The flakes are subsequently removed from the substrate using the same method with the tweezer. Small micrometer sized residual graphene and graphite flakes often remain on the substrate's surface. These flakes can then be found by scanning the sample with an optical microscope or an AFM. Tape free exfoliation leads to large and uniform graphene flakes. These flakes can be identified and located by the use of a back-illuminated optical microscope [75] and/or optical reflection microscopy where the sample is flipped over (the backside of the sample faces the objective of the optical microscope) [110]. An example of a graphene flake on mica imaged with optical reflection microscopy is shown in Fig. 4a. The flake consists of monolayer, bilayer, and multilayer graphene.

After imaging of the thinnest graphene flakes, it is required to quantify their thickness. This can be done by the use of Raman spectroscopy. In Raman spectroscopy, the intensity ratio between the G-band and the 2D-band can provide valuable information regarding the thickness of graphene [111,112]. As can be seen in Fig. 4b, the 2D-band has a very sharp and strong peak for monolayer graphene and it broadens for thicker graphene flakes. Moreover, there is a shift of the position of the 2D-band ($\sim 2678.8 \pm 1.0\,cm^{-1}$ for monolayer graphene) to higher wavenumbers for multilayer graphene. Furthermore, the G-band peak becomes higher with increasing thickness of graphene. For monolayer graphene, the intensity ratio of the G-band and 2D band amounts to about 0.3. This ratio increases for up to five layers of graphene and saturates for six graphene layers. Detailed investigation of the Raman spectrum can provide additional information regarding the structure, quality and doping of graphene [12,113].

After optical characterization of the graphene flake and identification of its thickness with Raman spectroscopy, the samples can be investigated further with the use of scanning probe microscopies. A

widespread AFM mode that has been used for the investigation of graphene covered water is dynamic AFM. Dynamic AFM modes use a vibrating tip in order to reduce the lateral force between the tip and the sample surface. Dynamic AFM studies have provided useful information regarding the structure and dynamics of the confined structures, since the tip-surface interactions are significantly reduced and thus tip induced behavior is largely avoided. In addition, other modes such as conductive AFM, Kelvin probe force microscopy (KPFM), scanning tunneling microscopy (STM) and spectroscopy (STS) have been extensively used and have provided information regarding the structural order of the first few layers as well as their influence on the graphene cover. Most of the experimental work reviewed here is focused on scanning probe techniques. We will also refer to studies using other surface science techniques, such as Raman, photoluminescence microscopy and spectroscopy and transmission electron microscopy (TEM). These studies in combination with theoretical methods such as molecular dynamics (MD) and density functional theory (DFT) provide useful information on the structure of confined water and the influence of this interfacial layer on the 2D material cover.

3. Hydrophobic-hydrophilic confinement

3.1. Graphene on mica

Water confined between hydrophobic graphene and hydrophilic muscovite mica has been extensively studied due to its technological importance [114–117], the relative trivial preparation procedure and the flatness of both surfaces, which guarantees smooth SPM imaging. A water film, with a thickness that depends on the RH, covers the mica surface at ambient temperature [41,80,82]. The structure and dynamics of water on mica were recently studied with the use of graphene as a soft protective cover, which allows visualization of these interfacial water structures. In the pioneering work by Xu et al. [75], exfoliated graphene was deposited on a freshly cleaved muscovite mica at room temperature and at various RH. Tapping mode AFM imaging of the deposited graphene flakes at 40% RH revealed island like flat plateaus of water with various sizes (ranging from a few nanometers to several micrometers), see Fig. 5a. These water islands had a well defined thickness of about 0.37 nm ± 0.02 nm (see Fig. 5b) and polygonal shapes with preferred angles of 120°. The size and density of these structures depended on the relative humidity (RH) during sample preparation. The RH dependence of the faceted islands as well as their well-defined thickness, suggests that the structures were ordered water layers. This suggestion is reinforced by the perfect agreement of the obtained height and the interlayer distance of hexagonal I_h-ice. Phase imaging of these islands showed no apparent contrast compared to their surroundings, implying that the AFM tip always interacts with the same surface, i.e., graphene, and that the plateau islands were under the graphene flake, see the inset of Fig. 5a [75,118]. In addition, the water islands were remarkably stable, remaining for weeks when covered with graphene.

The results of Xu et al. [75] opened the doors to a totally new line of research, i.e., the study of water confined between 2D materials. Their initial report gave rise to a lot of new questions that needed to be explored. For example, what is the exact structure of these confined water layers? What is the influence of the environmental humidity, pressure and temperature? Are these systems dynamic and if so under which conditions? What about airborne contamination? Is it absent or present in the system? What is the influence and interaction with the water molecules? How do graphene and mica influence the structure of these interfacial layers? What about multilayer growth? In the following sections, we review the articles that have shed light on these issues and as such have substantially improved our understanding.

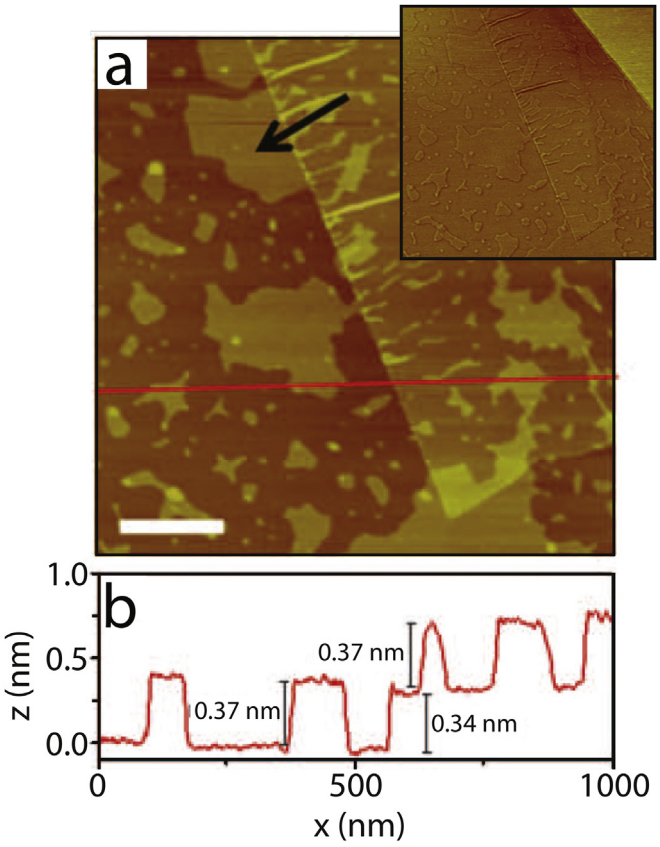

Fig. 5. (a) AFM image of graphene on water on mica, where the edge of a monolayer graphene sheet is folded underneath itself. The arrow points to an island with multiple 120° corners. Inset: The corresponding phase image. A Significant phase difference is observed between the mica (upper right corner) and graphene surfaces, reflecting the difference in surface properties [118]. In contrast, the same phase is observed for the plateaus and other parts of graphene (except for edges, which are always highlighted in phase images), indicating the AFM tip is interacting with the same surface (graphene), and the plateaus are underneath graphene. (b) The height profile along the red line in (a), crossing the folded region. Scale bars indicate 200 nm. The height scale is 4 nm. Reprinted with permission from Ref. [75]. Copyright 2010, American Association for the Advancement of Science. (For interpretation of the references to color in this figure legend, the reader is referred to the Web version of this article.)

3.1.1. Structure: ice-like or fluid?

The interpretation that the first water adlayers on mica are ice-like was based on the observation of the well-defined thickness of 0.37 ± 0.02 nm and faceted edges with angles close to 120°. This interpretation was soon after challenged by Severin and coworkers [105]. Fig. 6a shows a micrometer large and featureless graphene flake deposited on mica at 60% RH. Subsequent imaging over time under low humidity (below 4%), revealed the growth of small fractal shaped depressions, see Fig. 6b–d. These fractal depressions appeared to have a depth of about 0.28 ± 0.05 nm compared to their brighter surroundings. Similar to the observations of Xu et al. [75] these structures were under the graphene flake. The density and size of these structures increased over time and this increase slowed down only after half an hour. A reversal of the RH back to 50% led to the disappearance of these features almost instantly, see Fig. 6e. The fractal depressions immediately fill with water when subjected to high enough RH. Interestingly, repetition of the process and reformation of the fractal depressions at low RH leads to fractals grown at different locations and with different shapes, indicating homogeneous nucleation and that defects do not dominate their growth, see Fig. 6f.

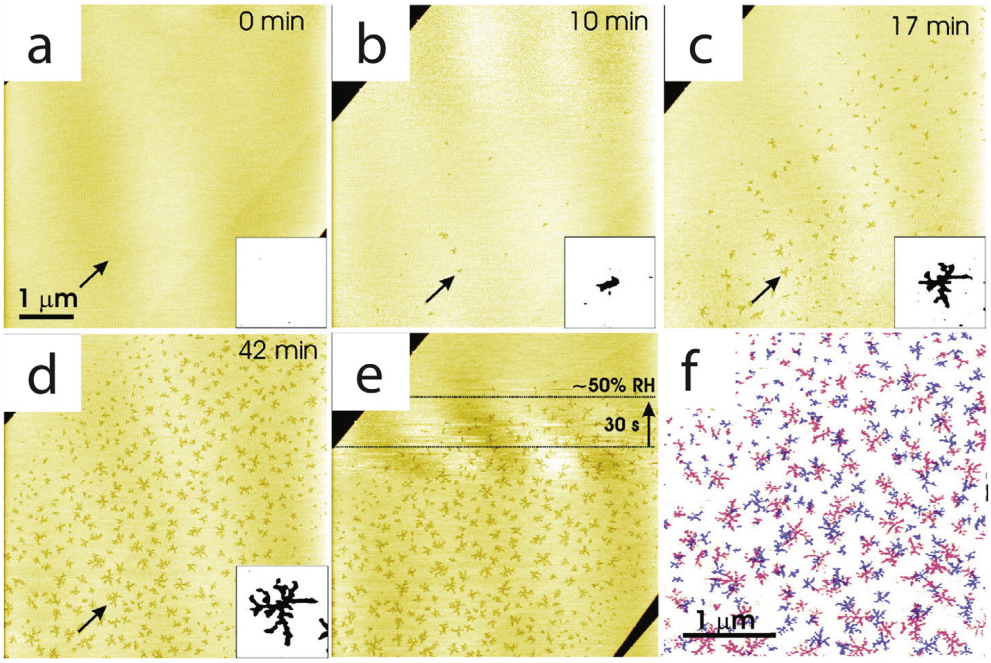

Fig. 6. (a) SFM tapping mode height images of single layer graphene (brighter area) deposited onto mica (darker area) at ambient conditions and imaged during purging of the SFM chamber with dry nitrogen. The time noted at the beginning of each scan is indicated directly on the images; the time required to take one image was 3.2 min. Insets show zooms (400 nm) into the area indicated with the arrow with strongly exaggerated contrast; threshold between black and white is offset by 0.6 Å from the graphene plane. (a) Initially, graphene is homogeneously flat; (b) first depressions appear at RH below 4%, (c, d) existing nuclei grow into fractal structures, and new nuclei appear. (e) Upon increasing the humidity, graphene becomes again atomically flat. The nitrogen flow was redirected to bubble through a water-filled jar at the beginning of the image; the slow scan direction is indicated with the vertical arrow. The lines are guides to the eye, which indicate the erasure of fractals; the time elapsed between the lines is 30 s. A subsequently taken image reveals a flat graphene topography similar to (a). Another decrease of the humidity caused the growth of new fractals. (f) The overlay of the images made on the same graphene area and after the same time of purging with dry nitrogen demonstrates that although visually very similar, new fractals do not correlate with the previous ones. The contrast is strongly exaggerated to leave graphene white and fractals colored; fractals from (d) are colored blue and the others in red. Reprinted with permission from Ref. [105]. Copyright 2012, American Chemical Society. (For interpretation of the references to color in this figure legend, the reader is referred to the Web version of this article.)

Fractals were also found to grow from defects on the graphene cover. An example is shown in Fig. 7a, where a large fractal grows from a graphene fold, suggesting heterogeneous nucleation. Regrowth of fractals from such locations gives rise to different fractal patterns [105,106]. Furthermore, fractals were found to form underneath thicker graphene flakes but with a somewhat coarser appearance. The authors of ref [105] identified that only defects in the cover that are in direct contact with the water film, allow evaporation and condensation of water from and into the interface. The most common form of defects on monolayer and few layer thick graphene flakes that can provide contact to the ambient are step edges. Fig. 7b shows a graphene flake were two types of step edges are found on bilayer graphene. Step edges located at the top (marked with (1)) of the first graphene layer and step edges located at the bottom (marked with (2)), also referred to as B-type step edges, of the flake. The step edges located at the bottom of the graphene flake are in contact with the water film and provide paths for water to escape into the ambient. These locations are the origin of several of the observed fractals. In contrast, step edges at the top of the graphene cover do not initiate the growth of the fractals. A schematic drawing of these two types of defects is shown in Fig. 7c.

The fractals grow initially at a fast rate and their growth slows down over time. After a few hours, the growth rate gets only incremental. The areal growth evolution of the fractal depicted in Fig. 7a is shown in Fig. 7d. In the reverse scenario, i.e., growth of the fractal structures and subsequent increase of the RH with discrete steps, the fractals become initially coarser and smoother. Further increase of the RH leads first to the shrinking of their extremities, followed by that of their trunks and eventually their disappearance and complete restoration of the water film [105,106].

Severin et al. [105] demonstrated that water confined between graphene and mica is in dynamic equilibrium with the environmental humidity and that defects on the graphene cover sheet allow direct communication with the environment. These fractal patterns were initially interpreted as dewetting patterns of the molecularly thin water film between graphene and mica. Based on their dynamic nature, the authors of ref [105] suggested that water confined between graphene and mica is fluid. However, evaporation from an intercalated fluid interface should rather result in circularly depressed areas [119] and not in the highly ramified fractal shapes observed here. In addition, the presence of fluid water cannot explain the dynamics observed in the filling of the fractals (a liquid should radially fill the interface) as well as the faceted hexagonal edges. Furthermore, it is clear that the shape of the fractals is not dominated by defects but it is rather an intrinsic property of the confinement. Li et al. [103] pointed out that the discrepancy between the works of Severin et al. [105] and Xu et al. [75] might be related to differences in the thickness of the confined water film.

Li and Zeng [120] performed ab initio molecular dynamics simulations to explore the structure and stability of the first few layers of water on mica with and without a graphene cover. In line with ref [84], they showed that the first water layer on mica is an epitaxially grown hydrogen bonded network, with no dangling hydrogen bonds sticking out of its surface. The water molecules in this layer form strong bonds with the oxygen atoms of the mica and exhibit little motion, thus forming a solid-like layer. Whereas the second adlayer is liquid-like. In addition, the graphene cover enhances the stability of the water layers. The first two layers becoming solid-like with a thickness of 7.4 Å, or in other words, equal to the thickness of two puckered bilayers of I_h-ice. The final configuration of the monolayer,

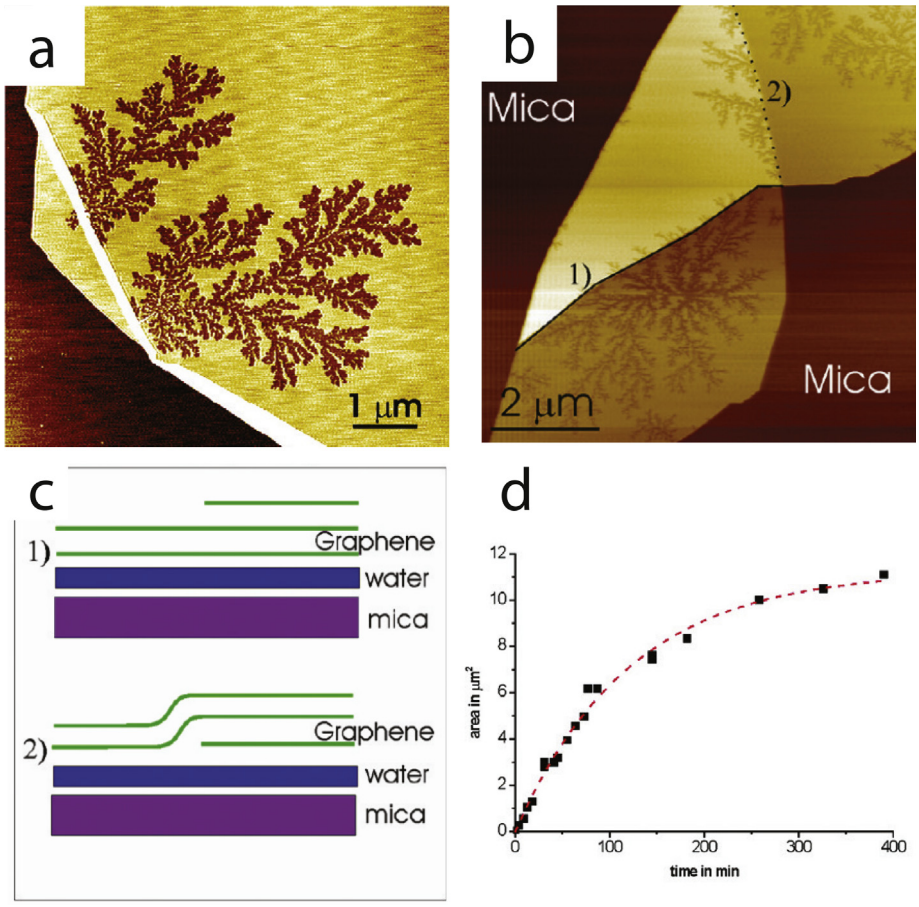

Fig. 7. (a) AFM image of two heterogeneously nucleated fractals grown at 10 ± 1% RH for 6 h. (b) AFM height image of a few layer graphene sample with fractal depressions. (c) Schematics for the proposed difference between the two types of step edges. The faint periodic stripes visible to some extent through all reported images are instrumental artifacts. (d) Growth dynamics characterized by the fractal area as a function of time; the dashed red line is an exponential fit. Reprinted with permission from Ref. [105]. Copyright 2012, American Chemical Society. (For interpretation of the references to color in this figure legend, the reader is referred to the Web version of this article.)

bilayer and trilayer of water between graphene and mica obtained from the calculations of Li and Zeng are shown in Fig. 8.

The structure and growth of the water confined between graphene and mica were further investigated by Song et al. [107]. In their study, they used temperature controlled AFM to investigate in situ the dewetting/rewetting dynamics of the confined water. As they were step-wise increasing the substrate temperature, they observed that at 50 °C fractal depressions (depth of 0.37 nm) started growing with similar dynamics as in Ref. [105]. The authors argued that the first water layer is ice-like at 100 °C, in line with the observations of ref [75]. They also provided evidence of multilayer growth during cooling of the sample from 100 °C to RT. They showed that the first adlayer is fully covered with water at RT and that the second water adlayer was directly aligned with the lattice orientation of mica, indicating that the ice-like water layers grow epitaxially on mica. Further experimental evidence of the epitaxial growth of the first adlayers on mica was also reported by Kim et al. [121]. They reported that the edges of the first water layer on mica not only form angles of about 120°, but also they are aligned with the lattice directions of the mica surface. The growth mechanism of the water adlayers was reported to follow the Stanski-Krastanov model [107].

He et al. [122] used the known height of a carbon nanotube to calibrate the thickness of the water film between graphene and mica with UHV STM. They found that two layers of water are most abundant at the interface. From their measurements, the first water layer was found to be ~0.4 nm, whereas the second was ~0.3 nm, suggesting a less ordered structure in the second water layer. These two water layer thick film was found to cover almost the whole interface. They also showed that the first water layer is crystal-like but without any long range order, as concluded from the absence of moiré patterns on the graphene surface. In addition, the second layer was liquid-like and easy to manipulate with the STM tip. These results confirm the solid-like structure of the first water layer between graphene and mica at RT [75,107,120,121].

This concept was later on adapted by Bampoulis et al. [106] to explain the growth and structure of the fractal depressions, that were reported first by Severin et al. [105]. In this model, a complete two-layer thick water film is confined between graphene and mica at ambient humidity. After the drop of the RH to ~1%, water molecules evaporate from the graphene/mica interface. The evaporation predominantly takes place from defects in the graphene cover, for instance bottom-type step edges, wrinkles and folds [105], see Fig. 7. The growth of fractals was attributed to be a result of the heat extracted from the interface due to the evaporation of water molecules. The fractals are composed of one monolayer thick 2D ice (long range order within the fractal) surrounded by a two layers thick, less ordered, water film (no long range order). The fractal growth was attributed to rotation limited aggregation of ice crystals formed during the de-wetting process (either by reducing the RH [105] or increasing the temperature [107]). Temperature dependent local variations and restrictions of the water molecules in the first adlayer play a crucial role in defining the ultimate shape of the

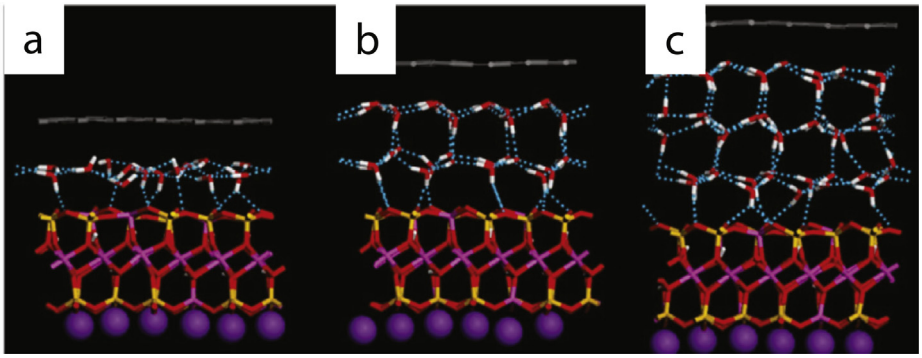

Fig. 8. A side view of the final configuration (at the end of 20–25 ps simulations) of the monolayer (a), bilayer (b), and trilayer (c) ice structure at 300 K. Reprinted with permission from Ref. [120]. Copyright 2012, American Chemical Society.

evolved ice crystal. The growth instability gives rise to fractal shapes, and the low rotational freedom and edge mobility play a crucial role in their appearance [123].

The presence of a monolayer ice at the locations of the fractal depressions was confirmed by the use of STM and STS [106]. First of all, the fractal structures have an overall hexagonal (dendritic) symmetry with faceted edges and angles close to 120°. The density of states of graphene above the fractal structure reveals p-type doping of graphene by 370 meV, whereas graphene above the surrounding double layer is slightly n-doped (50 meV). The large p-type doping of graphene is a result of charge transfer from the underlying substrate [124]. However, mica on average is electroneutral due to the presence of K+ ions [125], that balance the mica's surface charge. Therefore, the charge transfer must originate from the interfacial water. It suggests that this water structure is a long range hydrogen bonded network with a net dipole moment. Indeed earlier theoretical simulations [84,120] showed that the first water layer grows epitaxially on mica, see Fig. 8. This 2D ice, however, has a structure different from that of the puckered bilayer of I_h-ice. The hydrogen bonded network is polarized. The surface of this ice is negatively charged, which could in turn explain the shift of the Dirac point of graphene observed in Ref. [106]. In contrast, there is almost no influence of the graphene by the surrounding water bilayer, which implies disorder in the water layers at these locations. Further evidence of the crystalline nature of the fractals came from the observation of a solid-liquid phase transition induced by a locally applied external pressure [126], see section 3.1.2.

The detachment of the water molecules and removal from the interface is induced by the lowering of the environmental humidity and allowed/assisted by the hydrophobic nature of the 2D ice [106]. The absence of dangling bonds implies that additional water molecules on top of the first layer will be destabilized without reordering of the first layer. The ad-molecules can move across the ice boundaries by following the C—C bonds of graphene for steric reasons [121] and finally evaporate via defects [105] to the environment. This interpretation can explain the seemingly counter intuitive shrinkage and disappearance of the fractals at high relative humidity [105,106]. The water molecules that condensate at the interface when the system is exposed to high RH, are preferably transported to the younger extremities due to a larger temperature gradient at the condensation point and therefore fill the fractal from their extremities to their origin point, by coarsening and smoothing of their edges [106].

3.1.2. The influence of the cover, temperature and pressure

In the previous section, we discussed that water epitaxially grows on mica and its structure is determined by the mica surface and not by the graphene cover. In this section, we discuss the influence of graphene in this confinement. Kim et al. [121] used tapping mode AFM and friction force microscopy (FFM) to investigate the role of graphene on the structure and dynamics of the confined water. They found by comparing the directions of the edges of the water layers with the lattice directions of mica and graphene that the structure of the first layer is indeed crystalline and epitaxially oriented with the mica's lattice orientation. However, additional water intercalation led to the formation of striped patterns, see Fig. 9a. These additional water stripes were aligned with the C—C atomic zig-zag chains of graphene and not with the mica's lattice, Fig. 9b. The histogram of the angles between a particular zig-zag direction of graphene and the edges of the water stripes shows well-defined peaks at 0°, 60° and 120° (see the inset of Fig. 9a). This feature was attributed to kinetic effects. Graphene guides the diffusion of water along the C—C bond direction due to steric effects, while the mica still determines the structure of the water film [121].

Along with guiding water diffusion, graphene influences in another subtle way the intercalated water. As can be seen in Fig. 10, the fractals take on a coarser shape when thick graphene flakes cover them (grown at low RH). The coarsening of the fractals scales with the graphene thickness, see Fig. 10a and b. In order to understand this dependence, Bampoulis et al. [127] studied fractals grown under different graphene thicknesses. They first showed that the growth rate of the fractals depends on the purging rate of the N_2 gas, higher purging rates lead to faster fractal growth, due to faster water evaporation from the interface. This has a significant effect on the fractals' branch thickness. Faster grown fractals have much thinner branches and are more ramified, see Fig. 10c and d. The dependence of their branch thickness on their growth rate suggests kinetic limitations.

Graphene appears to play a prominent role in this mechanism. It was found that for a constant growth rate, the thickness of the fractals is determined by the thickness of the graphene cover and by the temperature. For constant temperature (RT) and growth rates, the thickness of the branches' width is only defined by the thickness of the graphene cover [127]. This observation was attributed to the finite bending energy of graphene that scales with its thickness [128]. Thicker graphene sheets do not conform that well to the edges between ice fractals and the surrounding water layers and thus leave small cavities at these locations. These cavities increase in size with increasing graphene layers and provide enhanced spatial freedom to the molecules that incorporate into the ice crystal. These molecules can diffuse around and rotate more easily and are thus able to find an energetically more favorable site to incorporate into the ice layer. This leads to coarser fractals that preserve their hexagonal symmetry. The authors of ref [127] could also determine the effective viscosity of the water molecules in the confinement to be about 6 orders of

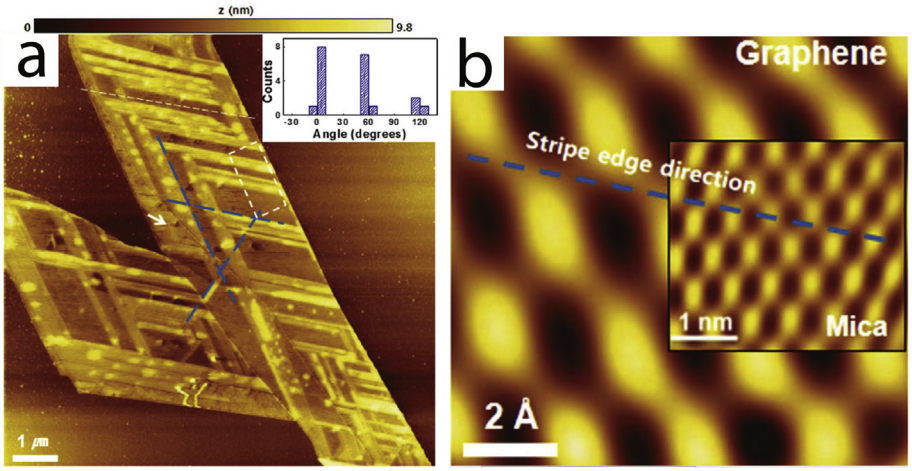

Fig. 9. (a) AFM topographic image obtained after exposure to high RH (~50%) for two weeks. The blue dashed lines delineate the directions of the striped patterns, which form angles of 60° with each other. (b) Low-pass filtered stick-slip image of graphene measured on the flake. The inset in (b) shows a low-pass filtered stick-slip image of mica. The blue dashed line in (b) is copied from the near-horizontal direction of striped patterns in (a). The inset in (a) shows the distribution of the relative angle of the stripe patterns with respect to an arbitrary zigzag direction of graphene in (b). Reprinted with permission from Ref. [121]. Copyright 2013, Springer Nature. (For interpretation of the references to color in this figure legend, the reader is referred to the Web version of this article.)

magnitude larger than the bulk viscosity of water.

The effect of temperature on the graphene confined ice on mica has been explored experimentally [106,107] and theoretically [120]. When the ice crystals were subjected to about 100 °C substrate temperature, they became coarser and acquired smoother edges [106]. This was attributed to pre-melting of the ice crystals that starts first at their edges. The water molecules gain more energy and can more easily diffuse around and find more favorable sites, which leads to coarsening of the fractal structures. Ochedowski et al. [129] showed that a complete removal of the intercalated water between graphene and mica is not possible. Even though small amounts of intercalated water were removed by heating to 600 °C, a complete removal was not possible without the decomposition of mica.

Melting of the confined ice crystals was also induced by the application of an external pressure [126]. Sotthewes et al. [126] have shown that the graphene-ice-mica system is an excellent playground to study classical experiments like Thomson's ice regelation experiment [130,131]. The confined 2D ice crystals melt upon the application of an external pressure locally applied by an AFM tip. The same AFM tip was also used to quantify the applied pressure. The ice crystals transform to quasi liquid layers of water for pressures larger than a critical pressure of 6 GPa. This pressure induced phase transition was found to be completely reversible; upon lifting of the pressure the quasi-liquid layers refreeze. The pressure induced melting of confined ice was attributed to shortening of the O:H nonbond and lengthening of the H—O bond upon compression. The H—O elongation results in energy loss which consequently lowers the melting point [132,133]. In this process, the role of K+ ions was not investigated. The presence of K+ ions [125] can influence the observed dynamics and the threshold of melting [134–137].

Along with additional temperature experiments, this provides the first experimentally obtained phase diagram of confined water between graphene and mica, see Fig. 11. By using the phase coexistence line of the phase diagram and the Clausius-Clapeyron relation [138] $(\ln(\frac{P}{P_0}) = -\frac{L}{k}(\frac{1}{T} - \frac{1}{T_0})$, where L is the specific latent heat of fusion, k is Boltzmann's constant and P_0 is the equilibrium pressure at some temperature T_0), the latent heat of fusion of 2D confined ice was determined to be 0.15 eV/molecule [126]. This value is two times larger than the latent heat of fusion of bulk ice. This minor difference was attributed to the fine details of the confinement.

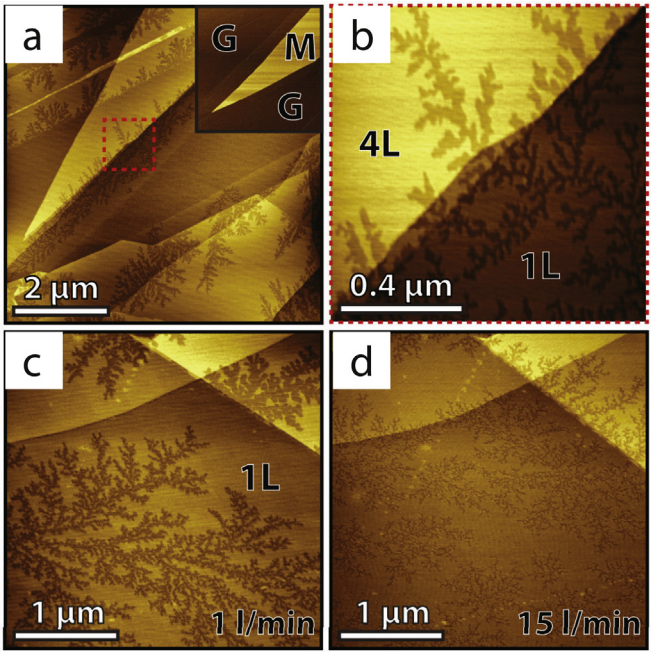

Fig. 10. (a) AFM topographic image of a graphene flake on mica after the growth of ice fractals induced by a drop of the RH. The inset shows the corresponding phase image. A clear contrast is visible between graphene and mica. (b) A small scale AFM image recorded on the red square in Fig. 1(a). Branches of a fractal crossing from 1 (1L) to 4 (4L) layers of graphene, the latter appear coarser. (c) AFM image of a graphene flake after the drop of the RH using a N_2 purging rate of 1 l/min. (d) The same area as in (c) after the drop of the RH using aN_2 purging rate of 15 l/min. Reprinted with permission from Ref. [127]. Copyright 2016, AIP Publishing. (For interpretation of the references to color in this figure legend, the reader is referred to the Web version of this article.)

3.1.3. Contamination and ad-molecules

In the following section, we discuss the influence of contamination on the properties and structure of the confined water. It is no secret that in most cases, exfoliation of graphene is done in air and with the use of adhesive tapes. Therefore, it is expected that airborne

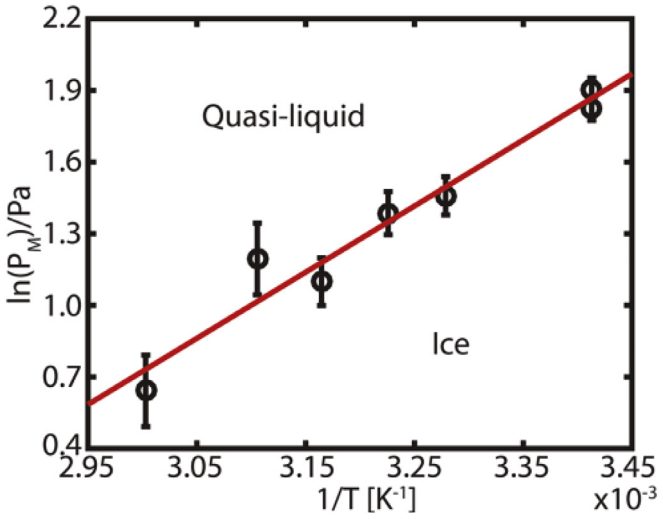

Fig. 11. Phase diagram of confined water in the pressure-temperature ($\ln(P_M)$ per Pa, $1/T_M$) plane. Reprinted with permission from Ref. [126]. Copyright 2017, American Chemical Society.

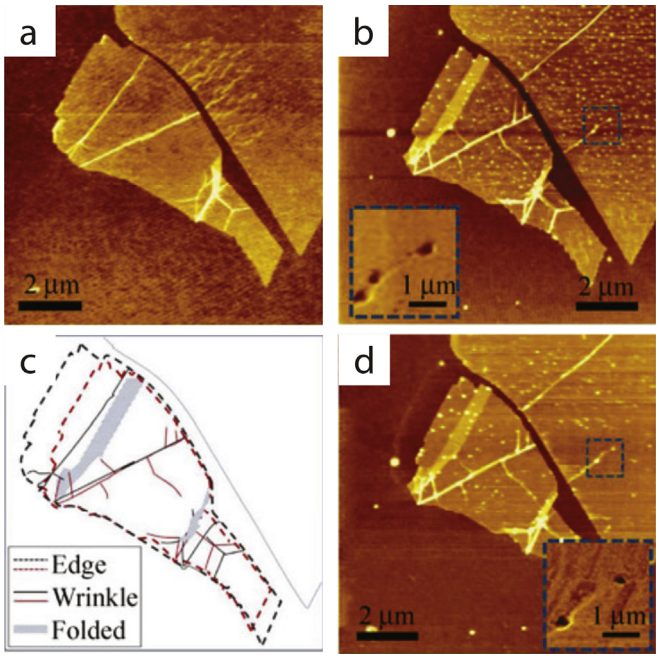

Fig. 12. Changes in monolayer graphene mechanically exfoliated on a SiO_2 substrate after exposure to high humidity. AFM topographic images of monolayer graphene (a) before and (b) after 1 week of exposure to high humidity. (c) An outline overlap of the graphene flakes of (a) and (b). Black and red colors denote graphene before and after high humidity exposure, respectively. Dashed and solid lines show edges and wrinkles, respectively. (d) An AFM topographic image obtained after a larger area scan for the graphene flake shown in (b). The insets in (b) and (d) show phase images simultaneously obtained with topographic images for the areas marked with blue squares. Reprinted with permission from Ref. [158]. Copyright 2012, Springer Nature. (For interpretation of the references to color in this figure legend, the reader is referred to the Web version of this article.)

contamination as well as tape residues to be present at the interface [139,140]. Rezania et al. [109] showed that the cleanest samples could be only obtained when using tape-free methods for the exfoliation and deposition of graphene. Exfoliation with the use of various tapes (three different types) led to samples with increased roughness. In addition, the dynamics of the confined water structures were also significantly influenced by the tape residues. Exposure of the graphene/water/mica system to low RH led to depressions of ill-defined shapes and not to the fractal depressions shown with the tape-free preparation method.

Interestingly, higher concentrations of dissolved molecules in the confined water have the tendency to phase segregate. Severin et al. [141,142] demonstrated that when the graphene/mica/system is exposed to ethanol vapor, ethanol intercalates under graphene. They observed a phase segregation to ethanol regions surrounded by water regions. The ethanol molecules formed well-defined islands. Similar patterns were also observed for other alcohols such as methanol, 2-propanol and 2-butanol [143]. In all the cases, the alcohol molecules were forming alcohol rich islands rather than mixing with the pre-existing water molecules. Interestingly, the alcohol molecules showed to preferentially adsorb at the ice/graphene interface than the graphene/water interface [143]. The observation of the phase segregation confirms theoretical studies [144–147] and shows that the structure and dynamics of confined molecules and molecular mixtures are significantly different from their bulk equivalents. Exposure of the system to water vapor (RH > 90%) leads to partial removal of the intercalated alcohol layers. Alcohol molecules pinned at the interface and unable to evaporate mix with the water molecules [143]. The alcohol contaminated water film behaves similarly to the observations made by Rezania et al. [109]. When exposed to low RH ill-defined irregular depressions are formed, different from the fractal depressions formed in an apparent clean system [105].

3.2. Graphene on SiO_2

Unlike graphene on mica, where graphene is atomically flat over very long distances [114], graphene on SiO_2 substrates is rough [148,149]. The SiO_2 surface is morphologically rough. Its roughness is almost an order of magnitude larger than that of atomically flat mica [114]. Graphene's high conformity allows an almost 99% fidelity of the SiO_2 roughness [150]. However, the performance of graphene depends strongly on its morphology. Large scale corrugations significantly impact graphene's electronic structure, inducing gauge fields [151], pseudomagnetic fields [152,153] and local doping variations [154–157]. Water intercalation, between graphene and SiO_2, has the potential to either surpass this impact by reducing its roughness, or lead to additional structural features such as wrinkles and folds [158]. It also plays an essential role in the further growth of molecular layers [159] suitable for molecular-based devices. Therefore understanding water intercalation between graphene and SiO_2 is key not only for understanding water diffusion mechanisms but also for improving the performance of graphene/SiO_2 devices.

For this purpose, Lee et al. [158] explored water diffusion between graphene and SiO_2 under high RH by AFM, see Fig. 12a. They found that for RH > 90%, water diffuses between the two surfaces forming an ice-like structure up to two-layers thick (~0.8 nm thick). Additional water exposure led to the intercalation of liquid-like water, Fig. 12b. The liquid-like water was stacking over the ice-like structure and could easily evaporate from the interface. Evaporation of water caused graphene to wrinkle and fold, Fig. 12b–d. The formation of folds and wrinkles was argued to be dependent on the hydrophilicity and roughness of the substrate.

In a similar study, Lee et al. [160] immersed Gr/SiO_2 in water. The use of Raman microscopy and AFM proved to be instrumental for real-time visualization of water diffusion between the two surfaces. The thickness of the first layer was found to be ~0.35 nm, very close to the thickness of I_h-ice. In addition, the diffusion dynamics were defined by the hydrophilicity of SiO_2. The diffusion rate was found to range between 0.1 and 3 μm/h among different samples. For strongly hydrophilic SiO_2 samples (formed by exposure to O_2 plasma) the water diffusion was instantaneously leading to fast detachment of the graphene. Kim et al. [121] performed contact mode AFM and FFM to investigate water diffusion between graphene and mica. They

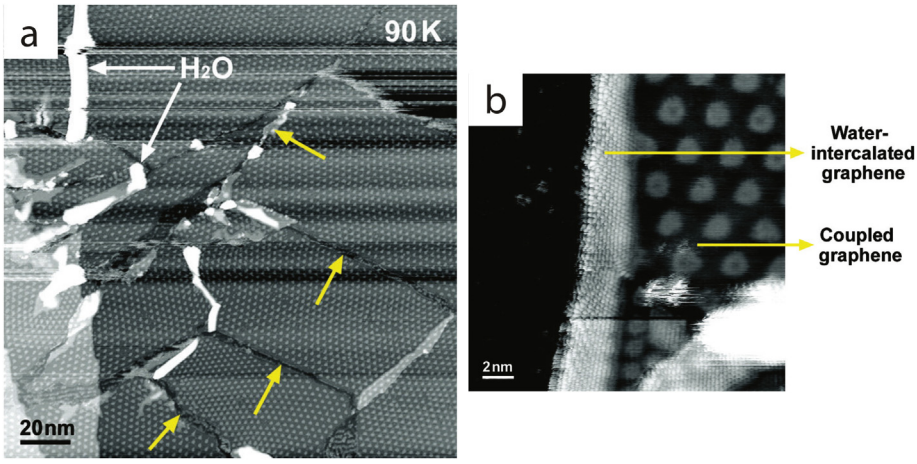

Fig. 13. STM images of the graphene surface on Ru(0001) after water exposure. (a) After annealing to 90 K for 5 min, water stripes are observed decorating some defect lines. The Moiré patterns on each side show different orientations (as indicated by the arrows), indicating a dislocation there. (b) Expanded view image showing the atomic-scale structure of water intercalated graphene at the edge of a fragment. Imaging parameters: $V_s = 1.5$ V, $I_t = 4$ pA (a); $V_s = 16$ mV, $I_t = 0.5$ nA (b). Reprinted with permission from Ref. [162]. Copyright 2012, American Chemical Society.

found that water regions under the graphene act as lubricants reducing the friction of the tip on graphene. Moreover, similar to water diffusion on mica, the water molecules diffuse into the interface by following the lattice directions of graphene.

3.3. Ionic substrates

Along with water between graphene-mica and graphene-SiO_2, other hydrophobic-hydrophilic confinements have been investigated. These studies have furthered our understanding of the role of the hydrophilic substrate with respect to the structure and behavior of the confined water. Recently, Verdaguer et al. [161] studied water intercalation and ice growth at the graphene-BaF_2 and graphene-CaF_2 interfaces. Interestingly, the intercalated water behaves significantly different on the two substrates. At high water coverages on BaF_2, water films of more than 5 layers thick were observed, with thicknesses of multiples of the I_h-ice thickness. At low coverage, two structures were observed for the first monolayer: an ice-like 0.37 nm thick layer and a 0.25 nm thick layer corresponding to the thickness of a planar ice film. On CaF_2, liquid like water films with a thickness of a few nm were reported, the difference was attributed to the large lattice mismatch between CaF_2 and ice. Temmen et al. [119] used AFM to study the dewetting dynamics of a multilayer water film between graphene and CaF_2(111). The samples were prepared at ambient conditions. The authors studied the response of these confined water film to annealing at temperatures up to 750 K. They demonstrated that even though it is possible upon heating to release some water from the interface, complete removal was impossible. Upon heating, the initial water film was separated to water-rich and water-free regions. The separation process was attributed to 2D Ostwald ripening. Further heating led to rupture of thick graphene flakes and the formation of blisters on multilayer graphenes.

3.4. Metals and metal oxides

The interfaces between graphene-metal and graphene-metal oxide bear excellent promise in for instance (photo)catalysis, sensors and batteries [162–165]. The adsorption and reaction of water in these systems is key in defining their functionality and properties. Water intercalation and adsorption were found to affect epitaxially grown graphene on metal substrates. Feng et al. [162] demonstrated by the use of STM that line defects of epitaxial graphene on Ru are fragile. Water can chemically attack these sites and split graphene into many fragments even at cryogenic temperatures (~90 K), see Fig. 13a. Water then proceeds to intercalate under the graphene, decoupling it from the metal substrate, Fig. 13b. The process was far less effective on Cu(111) indicating that the reactivity of the C—C bonds in epitaxial graphene is affected by the substrate. In addition, on defective graphene on Cu, water was shown to be able to break the C—Cu bond formed at the defect site, restoring the weak Van der Waals forces between the two surfaces. The same was not found for graphene on Pt, where the bonds were found to be much stronger [166]. The permeation process occurs through graphene grain boundaries. Yoon et al. [167] showed that the lateral diffusion of water in these systems is considerably suppressed compared to bulk water.

A couple of studies have also focused on intercalation effects and the structure of water between graphene and metal oxides. For instance, Komurasaki et al. [168] investigated water trapped between graphene and sapphire under controlled RH. At low RH, water forms small islands, whilst an increase of the RH leads to a layer by layer growth. The thickness of the first layer amounts to 0.37 nm, suggesting an ice-like structure. Moreover, Datelo et al. [169] showed by the use of dispersion-corrected hybrid density functional calculations that water at the graphene-TiO_2 interface prefers to dissociate. Olson et al. [170] investigated water between graphene and HfO_2. They showed that the intercalation process is reversible with repeated RH cycling. This process could be detected electrically demonstrating the sensing capabilities of graphene and fabricating the first graphene-water based sensor.

4. Hydrophobic-hydrophobic confinement

The behavior of water nanoconfined in a hydrophobic planar geometry has received a lot of attention due to its role in biophysical processes, nanofluidics, energy storage and novel physical properties [31,33,171–177]. For instance, forced intrusion or extrusion of water from and into hydrophobic nanopores leads to dissipation or storage of mechanical energy [178]. The weak interaction of water with the hydrophobic walls leads to the growth of ice layers with unique structure and properties [64,179]. Early experimental investigations of confined water in hydrophobic nanopores already suggested the presence of ordered layers. Liyama et al. [171] showed with X-ray diffraction that water in a hydrophobic nanopore

orders parallel to the pore's walls. Maniwa et al. [180,181], using X-ray diffraction, demonstrated that water fills single-walled carbon nanotubes and crystallizes into a solid, forming the so called 'ice nanotubes'. These ice nanotubes were first predicted by Koga et al. [182] using molecular dynamics. Their simulations revealed the spontaneous formation of a variety of ice phases inside carbon nanotubes, depending on the nanotube's diameter and pressure. Similar observations have been made experimentally by surface sensitive techniques such as vibrational spectroscopy [183], solution nuclear magnetic resonance (NMR) [184] and neutron diffraction [185]. Several ice structures have been reported including square, pentagonal, hexagonal, and octagonal single walled ice nanotubes [19,180–183,185]. Kolesnikov et al. [185] explored the phase diagram of ice and its melting point in single walled carbon nanotubes at ambient pressures. They reported nine different hydrogen bonded phases with different melting points. The highest melting point was reported to correspond to the square ice nanotube.

Computer simulations have revealed a variety of crystalline water phases and water phase behavior in nanoconfined water in between parallel hydrophobic plates [21,186,187]. Water between two hydrophobic parallel plates can form 2D ice structures such as puckered rhombic ice, planar hexagonal and several amorphous phases [16,33,188–192]. Temperature, pressure and the confinement dimensions play a prominent role in defining the state and structure of the confined water [193]. However, experimental investigations of water nanoconfined in parallel hydrophobic pores are scarce [187,194] due to limitations posed by the confinement. Jinesh and Frenken [195] applied friction force microscopy to investigate nanoconfined water between graphite and a tungsten tip. Their results revealed that water condensates between the tip and the surface form ice structures even at room temperature. The stick-slip motion of the tip revealed a period of ~0.38 nm, i.e., different from graphite's lattice periodicity. This phenomenon was interpreted as the consequence of shear-induced fracture and healing of the tip-confined ice. It revealed that after shearing of the ice the molecules rearrange within seconds.

Inspired by the use of graphene on mica to visualize the structure and dynamics of trapped water. Cao et al. [196] used graphene flakes to study adsorbed water on three hydrophobic substrates, i.e., trimethylchorosilane -functionalized mica, graphite and H-terminated Si(111). In these three cases, under ambient conditions, water adsorbs as liquid nanodroplets (10–100 nm). The adsorption took predominantly place at defects and step edges of the surface. The nanodroplets had contact angles of approximately 10° and their size and density were dependent on the relative humidity during the preparation procedure. Similarly, STM on graphene coated water on Au(111), revealed a preference for water adsorption at step edges, for samples prepared at ambient conditions [197]. These studies reveal the importance of surface defects and step edges for water adsorption and nucleation on hydrophobic substrates. At these sites, water might interact more strongly with the surface owing to dangling bonds.

4.1. Water in graphene nanocapillaries

The most unique example of hydrophobic confinement that has recently attracted a lot of attention is water trapped between graphene layers. Understanding graphene-water interactions is not only of fundamental importance for understanding ice nucleation in nanopores but also essential for many physical and chemical processes involving graphene. These interactions define graphene's wettability, permeability and electrical properties [198–203]. Chialvo et al. [204] performed molecular simulations of two graphene plates immersed in water at isobaric-isothermal conditions. Their work revealed that graphene confinement has a severe impact on the water. It increases the isothermal compressibility and isobaric thermal expansivity of water. Furthermore, the water dynamics are suppressed, compared to its bulk counterpart. The exact magnitude was found to be dependent on graphene's corrugation.

Algara-Siller et al. [179] reported evidence for the presence of a 'square-ice' form of water between graphene nanocapillaries. The symmetry of which is different than the tetrahedral geometry of natural ice. The investigation of this apparent 'square-ice' was done by TEM, electron energy loss spectroscopy (EELS) and MD simulations. The samples were fabricated by the deposition of graphene monolayers on a TEM grid. Graphene was then exposed to water and subsequently covered by another graphene layer. Most of the water was consequently squeezed out by the Van der Waals forces between the graphene sheets. The remaining water was visualized by TEM. Graphene played an important role in allowing the visualization and investigation of the confined water structures. Its low atomic number and crystallinity leads to a weak background signal in the TEM images, giving thus strong contrast for the oxygen atoms [205,206]. Essentially, it allows the direct visualization of the water network. Moreover, graphene's high electrical and thermal conductivity, chemical stability, flexibility and mechanical strength further protects the water structures from damage induced by the electron beam [207].

An example of the observed square lattice is shown in Fig. 14. In the Fig. 14, the dark spots represent the oxygen atoms and thus indicate the locations of the H_2O molecules. The image shows a square lattice with a periodicity (obtained by FFT analysis, see the inset of Fig. 14) that amounts to 2.83 ± 0.03 Å. These layers have sharp 90° edges but were not aligned with the lattice of graphene. The authors investigated with EELS regions with and without ice. In contrast to the ice-free regions, square-ice regions display an EELS spec-

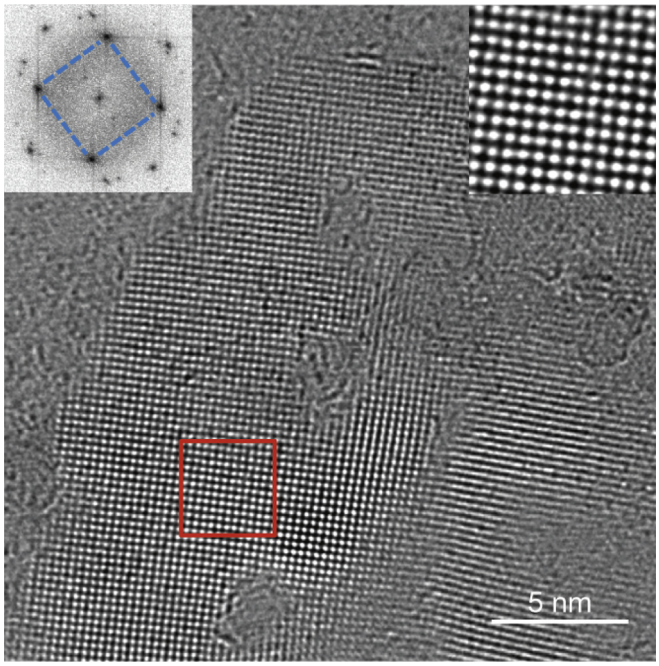

Fig. 14. Part of a large water pocket. Several such pockets were studied. Irregular structures are hydrocarbon contamination. The top right inset shows a magnified image of the area outlined in red. The top left inset shows a Fourier transform of the entire image, with four first-order maxima of the square lattice; the square symmetry is highlighted by the blue lines; the two hexagonal sets come from encapsulating graphene. Reprinted with permission from Ref. [179]. Copyright 2015, Springer Nature. (For interpretation of the references to color in this figure legend, the reader is referred to the Web version of this article.)

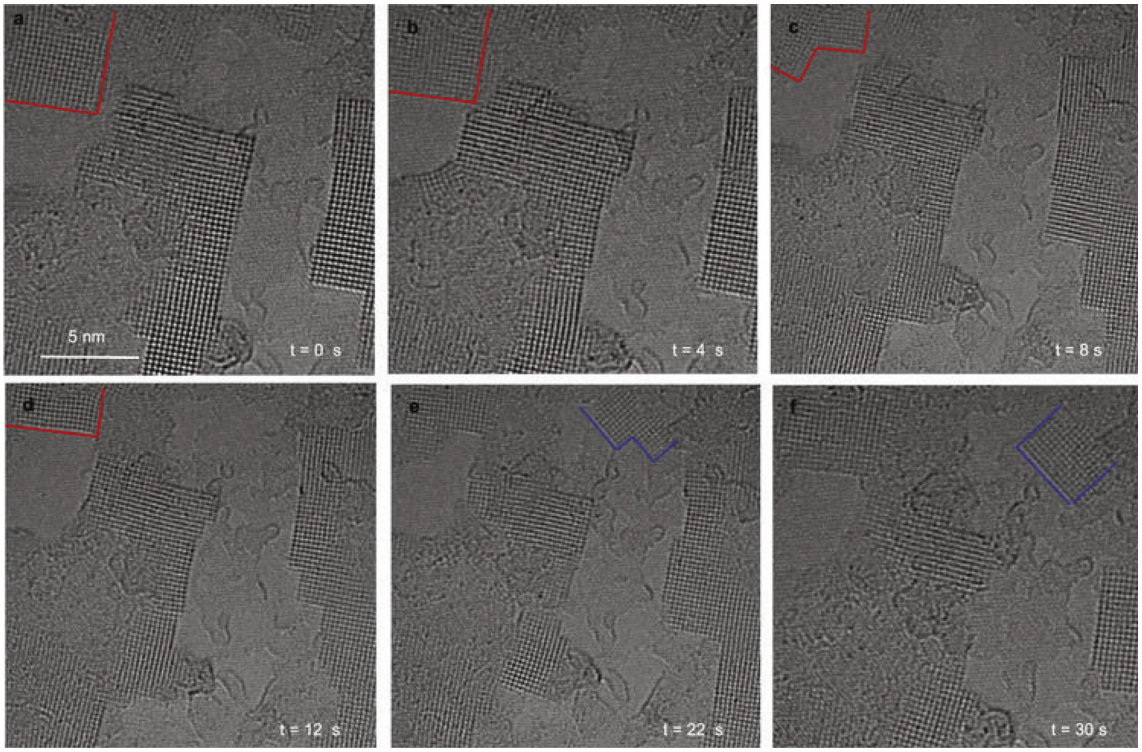

Fig. 15. High-resolution snapshots illustrating continuous reorganization of ice crystallites. Red lines highlight some of the changes: the bilayer crystal in (a) thins down to a monolayer in (b), then splits into two crystals separated by a grain boundary in (c), and a trilayer is formed in the same area in (d). In (e), a new crystallite, outlined in blue, appears in the top right corner, growing and propagating towards the center in (f). Other crystallites also change from panel to panel. Reprinted with permission from Ref. [179]. Copyright 2015, Springer Nature. (For interpretation of the references to color in this figure legend, the reader is referred to the Web version of this article.)

trum that is in qualitative agreement with the EELS spectrum for I_h-ice and I_c-ice (cubic ice) [179,208]. However, some distinct differences were also observed that were ascribed to the nature of the square ice and the influence of the confinement. The square-ice layers were found to be highly mobile and influenced by the electron beam. A rich dynamic behavior was observed including processes such as coalescence, shape modification and splitting of the islands, see Fig. 15. However, their crystallinity was maintained in every case without any signs of melting or amorphization. Square-ice multilayers of maximum three layers were also observed. These multilayers were found to have an AA stacking order.

Even though MD simulations could reproduce an almost square pattern of the water molecules in graphene nanocapillaries at high pressures, they failed to capture the observed AA stacking of the multilayers, even when pressures larger than 1 GPa were considered. Instead, they revealed a preference for an AB stacking order or no interlayer order at all. Moreover, the authors [179] suggested that similar square-ice patterns might be present in other hydrophobic confinements.

The interpretation of the observations of ref [179] as square-ice was soon after questioned by Zhou et al. [209]. They proposed that the reported square lattice [179] is better explained by contaminants such as NaCl present at the interface. Indeed, the lattice observed by Algara-Siller et al. [179] resembles a lot that of NaCl nanoplatelets in a graphene liquid cell. These nanostructures have a square symmetry with a lattice constant of about 2.8 Å [209], matching the periodicity observed in square ice [179]. The observed beam-induced dynamics were also similar. Zhou et al. [209] questioned also the observation of the O_2 peak in the EELS signal as evidence for water. They suggested that the oxygen signal might originate from Si-based contaminants present at the interface. Additionally, they performed DFT calculations and MD simulations on square ice in graphene nanocapillaries. They found that the square lattice relaxes to a more stable rhombic zig zag structure.

The points raised by Zhou et al. [209] were commented by Algara-Siller et al. [210] and Wang et al. [211] Algara-Siller et al. [210] strongly declined the presence of contamination. The authors however agreed that more experiments are required to rule out any influence from contaminants. Wang et al. [211] suggested that the rhombic pattern observed in the simulations will appear as square in TEM images due to time averaging effects. These works pointed that further theoretical and experimental investigations are needed to shed light to the square ice controversy and its stability inside graphene nanocapillaries.

4.2. Stability of square ice

The work of Algara-Siller et al. [179] has led to a plethora of new theoretical studies investigating the stability and properties of square ice in hydrophobic confinements [212–220]. Diffusion Monte Carlo simulations performed by Chen et al. [214] showed that at relatively high pressure, square ice is the phase with the lowest enthalpy inside graphene nanocapillaries. However, due to the insufficient experimental studies and the different theoretical tools and methods used, the presence and stability of the AA stacked bilayer square ice is still under debate. The reproduction by MD simulations of the squared ice monolayer required the inclusion of a high Van der Waals pressure in the order of 1 GPa [179]. Whereas, the AA stacking could not be reproduced in the original MD simulations. DFT calculations and MD simulations performed by Zhou et al. [209] revealed that the most stable phase in the graphene nanocapillaries is a rhombic ice structure. Several recent theoretical works investigated the stability of AA stacked square ice, but the multilayer stacking order could not be consistently reproduced. Mario et al. [221] found by the use

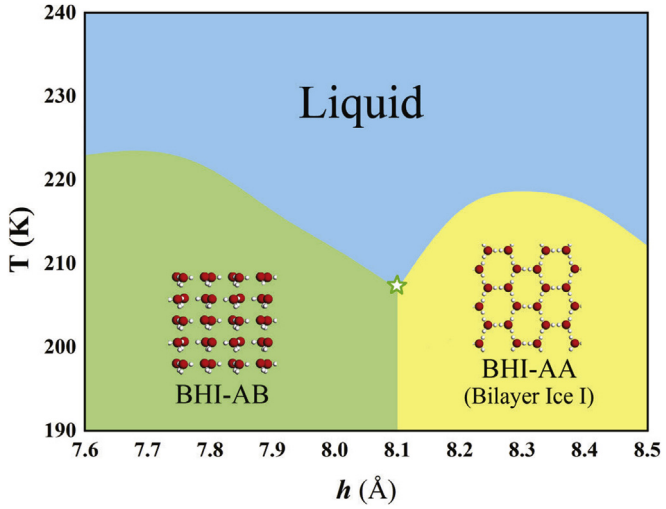

Fig. 16. Phase diagram of BHI-AB and BHI-AA in the temperature (T)- separation(h) plane for P = 450 MPa. The open star is the triple point, estimated to be located between 205 and 210 K and 8.0–8.2 Å. Two solid phases have different symmetries and are thus separated by a phase boundary. The insets illustrate the structures of BHI-AB and BHI-AA, respectively. Each liquid-solid phase boundary exhibits a local maximum. Reprinted with permission from Ref. [224]. Copyright 2018, American Chemical Society.

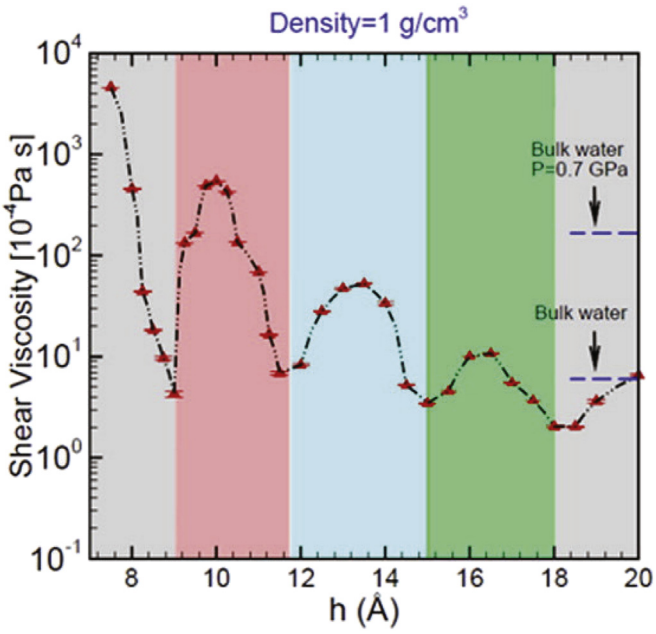

Fig. 17. Variation of the shear viscosity of confined water between two graphene layers, which are separated by a distance h. The result for bulk water is taken from Ref. [228]. The dashed line is a linear interpolation of the data. Reprinted with permission from Ref. [229]. Copyright 2016, American Chemical Society.

of molecular dynamics simulations with the adoptable ReaxFF (reactive force field) interatomic potential that a monolayer of rhombic ice confined between two graphene sheets is nonpolar and nonferroelectric. In addition, they could reproduce the AA stacking by refining the energetics and H-bonding of the ice-network. Application of an in-plane external electric field could polarize the H_2O molecules of the square ice leading to ferroelectricity and electrical hysteresis [222].

Even though Mario et al. [221] could reproduce the AA stacking, DFT calculations suggested that the AA stacked bilayer is unstable compared to the high density phases [223]. MD simulations performed by Zhu et al. [224] suggested that the AA stacked square pattern is rather a rectangular pattern formed by the AB stacking of a stretched hexagonal bilayer ice (BHI-AB). The authors also observed in the temperature-nanoslit gap phase diagram a solid(BHI-AB)-liquid-solid(BHI-AA) triple point, Fig. 16, with the second solid phase, BHI-AA, being the bilayer hexagonal ice with AA stacking order. This transition took place for a 450 MPa pressure, at a temperature of 210 K and gap space of 8.0–8.2 Å. The BHI-AA phase has been observed in older MD simulations [225] and has experimentally confirmed to exist at low temperatures on hydrophobic substrates [64,65] and at room temperature in between graphene and MoS_2 [226]. The structure of the BHI-AA and BHI-AB phases are shown in the insets of Fig. 16. The BHI-AA phase consists of two flat hexagonal H-bonded layers of water molecules in registry with each other. In this arrangement, each molecule forms three hydrogen bonds with neighboring molecules and one out of plane hydrogen bond with the opposite layer [64,225]. The system can be considered to be hydrophobic since there are no dangling OH bonds or electron lone pairs available. The hydrophobicity of BHI-AA ice was explored for ice films between graphene and MoS_2 [226]. Additional water condensation on the confined bilayer resulted in either the lateral expansion of the bilayer or the formation of 3D droplets, suggesting that water does not wet this ice film.

Chen et al. [191] highlighted the sensitivity of the 2D ice for pressure and the width of the confinement. First principles calculations revealed a strong dependence of the ice structure on the pressure. At ambient pressure, pentagonal and hexagonal monolayers have the lowest enthalpy. Compression up to 2 GPa makes the pentagonal phase the most stable. At pressures above 2 GPa, the rhombic and square ice become the most stable.

4.3. Dynamics of water nanoconfined in hydrophobic capillaries

Sharma et al. [227] used MD to investigate the evaporation rate of water in a hydrophobic confinement. They found that the evaporation rate of water depends strongly on the wall's separation distance and the surface area considered. The evaporation rate decreases exponentially with an increasing gap size. Increasing the surface area of the hydrophobic surface leads to an increase of the evaporation rate.

Nek-Amal et al. [229] demonstrated that the viscosity and flow rate of the nanoconfined water within pores, smaller than 2 nm, are dominated by its structure. The shear viscosity of water was found to be sensitive to the size of the separation distance of the confining walls. Decreasing the separation distance by even an Å resulted in an enhancement of the shear viscosity by more than an order of magnitude, see Fig. 17. In addition, the shear viscosity exhibited well-defined oscillations in the viscosity-wall distance graph, Fig. 17, with maxima located at gap sizes, h, of 7.5, 10, 13.5, and 16.5 Å and minima at h = 9, 11.5, 15 and 18 Å. These findings were attributed to originate from the commensurability between the size of the water molecules and the size of the gap. When the water layers are commensurate with the size of the gap the shear viscosity is at a minimum. Contradicting results of earlier works [230,231], where the oscillations were absent, come from the use of different simulation/calculation models. A further increase of the gap size above 2 nm led to viscosity values near that of the bulk viscosity, showing that water in a confinement larger than 2 nm behaves like bulk water. Similarly, Fang et al. [232] reported higher viscosity values for quasi-2D water in graphene channels than that of bulk.

5. Hydrophilic-hydrophilic confinement

While water has been shown to freeze in hydrophobic nanopores, even at room temperature (see section 4), water in hydrophilic

nanopores crystallizes at temperatures much lower than its bulk freezing point [233–239]. For instance, water in cylindrical hydrophilic nanopores of aluminophosphate microporous crystals with a diameter of 1.2 nm freezes at 173 K [240]. Earlier studies of water in hydrophilic confinement include water between mica sheets, silica pores, aluminophosphates, diamond and glass [240–244]. These studies mainly use spectroscopic techniques, molecular simulations and AFM. In these systems, water at the confinement walls orders into layers, but without any lateral order, often being in a liquid-like or a glassy form. This unusual behavior is stemming from an insufficient amount of H-bond formation and curvature induced hindrance [240]. These effects interrupt the formation of ice-like networks and keep the confined water in a liquid-like (or a glassy) state. In addition, the disordered nature of several hydrophilic surfaces destabilizes further the formation of H-bonded crystalline layers [239]. A characteristic example of such a behavior was reported for silica nanopores [245–247], where water crystallizes at temperatures far lower than bulk water does [237,239].

Similar to silica nanopores, water confined between mica surfaces has been reported to remain liquid-like [234–236,238]. This is in contrast to water adsorption on mica, where crystal-like properties have been reported for the first monolayer both experimentally and theoretically, even at room temperature [82,84,248]. The water structure inside mica pores is however disrupted by the presence of K+ ions that interrupt the H-bonds between H_2O molecules in the water film [249]. Fedyanin et al. [250] found that water under 9.2 Å mica confinement sustains shear stress similar to solids, but has liquid-like mobility and lateral order. The liquid-like properties of water in between mica sheets were found to be preserved down to two layers thick films. An increase of the confinement led to the formation of bilayer ice [79]. This ice phase has a lower density than the I_h-ice, which was attributed to the fine details of the confinement and H-bond formation. Interestingly, the diffusion constant of this ice phase was found to be approximately four orders of magnitude lower than that of thick hydration films [79]. AFM investigation of a Si tip approaching a mica surface revealed oscillatory solvation forces, suggesting also the ordering of water at close proximity to the mica surface. For separation distances below 1 nm, the viscosity was orders of magnitude larger than that of bulk water [241]. The interaction of two mica sheets immersed in water based ionic solutions and brought into mechanical contact, was explored by surface force apparatus (SFA) [235,251–254]. At large sheet separations (>2 nm), the interaction obeyed the DLVO theory [5], where Van der Waals interactions and electrostatic double layer repulsion play the dominant role. At smaller separations, short range repulsive forces were observed [251,252,255].

Another system of a hydrophilic confinement that has recently received considerable interest in nanofluidics, water filtration and purification processes [22,256–258], is water diffusion in graphene oxide (GO) membranes. Water permeation through submicrometer thick GO membranes has been reported to be unimpeded [259]. In the seminal work by Nair et al. [259], GO membranes were impermeable to liquids and gases (even to helium) but allowed the rapid flow of water. This anomalous behavior of water permeation across GO membranes has attracted a lot of attention due to its exceptional potential for filtration and sieving applications [260–262] and the intriguing physical mechanism of water transport [23,24,263].

MD simulations have explored various mechanisms for describing this unusual water transport through GO membranes [24,259,264,265]. However, the nonuniform nature of GO poses a significant barrier in computational methods to give a detailed and accurate account of the involved processes. Transport across GO membranes was proposed to follow a capillary driven flow mechanism [259,261]. The anomalous permeation was initially attributed to a nearly frictionless flow of water at regions where graphene remained unoxidized (pristine). The pristine regions provide capillary channels that allow water to flow almost unimpeded. This interpretation suggests clustering of water molecules and collective diffusion. In addition, the GO interlayer distance was also found to be important. Reduction of GO (to graphene) and subsequent decrease of the interlayer distance resulted in the impermeability of the membrane to water [259]. Boukhvalov et al. [263] suggested that indeed the GO interlayer distance controls the water flow. This was based on the formation of hexagonal ice bilayers for only specific interlayer distances of pristine regions and the melting transition of the ice at the edges of the GO sheets. Tuning of the GO interlayer distance can be achieved by pressure, functionalization and annealing [257,266]. This mechanism could account for the observed perfect water permeation and rapid flow. However, the presence of contiguous and linked pristine channels is low for thick membranes [267,268].

TEM imaging of GO membranes revealed that only about 16% of the membrane consists of pristine regions, while the rest is mainly oxidized [267]. Moreover, these regions are expected to be randomly distributed and with hardly any contiguous regions [264,269]. Because of the randomness in the distribution of oxidized and pristine regions, it is unlikely that the reason behind the fast flow is solely the capillary action. Furthermore, the interaction of water within the pristine graphene pores with adjacent oxidized regions can potentially reduce the flow speed [23]. Drag can also be generated by water in the pristine regions interacting via H-bonding with water at oxidized regions [24]. Talyzin et al. [270] proposed that fast water permeation across GO membranes is not only limited to pristine GO regions. Willcox et al. [265] addressed this issue by performing MD to study water flow across sheets of oxidized, pristine and mixed regions (GO-graphene). They found that along with pristine regions, mixed regions show water flow significantly greater than the oxidized regions. It was proposed that these regions could play a significant role in water flow. In addition, defects such as wrinkles might play an important role in water flow [202,271]. Indeed Wei et al. [24] proposed that the rapid flow is mainly the result of porous microstructures such as wrinkles, holes and interedge spaces. This finding provides an alternative and complimentary explanation on the mechanism of the fast water permeation.

Water within the corrugated GO channels has been shown to be disordered [264]. The hydration of the GO bilayer under controlled RH and water immersion was recently visualized with tapping mode AFM [272]. A gradual increase of the RH from 2% to 80% led to a gradual growth of the GO interlayer distance (increase of the height in the AFM images) by about 1 Å, implying water intercalation. The interlayer distance grew by about 3 Å when the GO flakes were immersed into water. The height increase was attributed to the intrusion of a water monolayer in between the GO sheets.

6. Influence of water on the cover material

As 2D materials are in essence all-surface, their properties are extremely sensitive to the environment, i.e., the supporting substrate, adsorbates and intercalates [148,273–278]. Therefore, the adsorption or intercalation of chemical species can influence the electronic, optical and tribological properties of 2D materials [273,274,276,279–281].

Control over the spatial distribution and orientation of the adsorbates/intercalants allows tuning of the 2D material properties. To this extent, interfacial water offers direct control of the electronic structure of 2D materials by altering the local electronic charge, leading to a heterogeneous electronic environment. The same holds for their tribological properties, since they are influenced by the interaction of the 2D material and the underlying intercalants. This can provide a direct pathway for a variety of applications using water

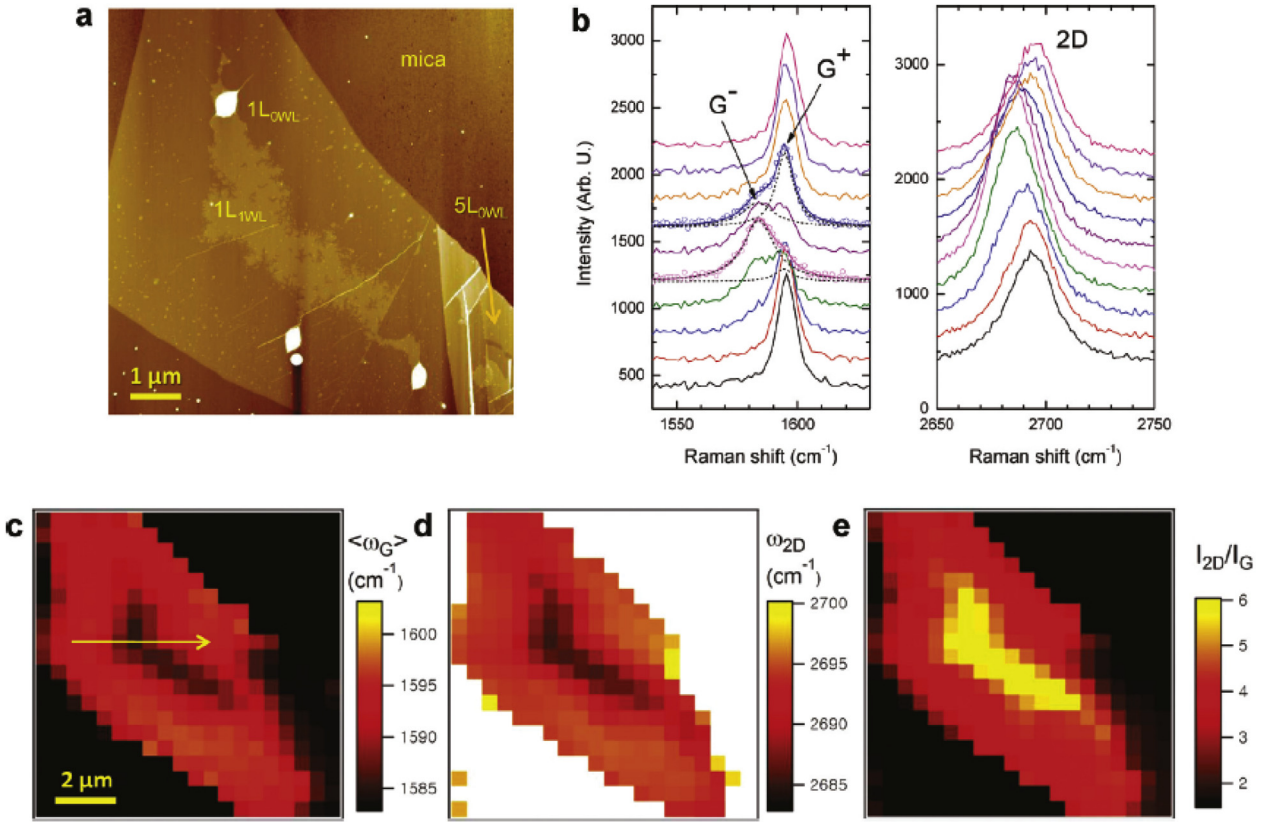

Fig. 18. Raman spectroscopy characterization of water-gated hole doping in graphene on mica. (a) AFM height image of graphene on mica obtained in the noncontact mode. (b) A series of G and 2D band Raman spectra (solid lines) taken for graphene on mica along the arrow in c (from bottom to top). The G band of the fifth and seventh spectra in panel b was fitted with two Lorentzian components, G^- and G^+ (dashed lines): the solid line through the data (circles) is the sum of the two. (c–e) Spatial Raman maps of G and 2D bands taken for graphene on mica substrate: the G-band frequency, ω_G (c); the 2D-band frequency, ω_{2D} (d); the integrated intensity ratio of 2D to G band, I_{2D}/I_G (e). As a representative value for the G band frequency in panel c, the population mean $< \omega_G >$ was used instead of the peak frequency (ω_G) to account for the asymmetry arising from the presence of two components (G^- and G^+). The multilayer areas are not clearly resolved in the Raman maps since their values are out of the specified ranges. The laser excitation wavelength for the Raman measurements was 514.5 nm. Reprinted with permission from Ref. [12]. Copyright 2012 American Chemical Society.

or other organic components to alter the properties of 2D materials, such as nanofluidic transport, local p-n juctions and lubrication at ambient and aqueous environments.

6.1. Electronic doping by intercalated water

Water induced hysteresis was observed in the electrical characteristics of carbon nanotubes. This electrical influence was tunable by altering the amount of water molecules surrounding the carbon nanotube [282]. Several theoretical investigations have explored the influence by simulating the effects of a water layer bound to graphene on its electronic properties [198,283,284]. It was found that water molecules have very little effect on the electronic structure of graphene because their dipole moments tend to be oppositely oriented to cancel out on average [283,285]. However, macroscopic transport measurements revealed changes in the graphene resistance upon the adsorption of gas molecules [274]. For sufficiently high water concentrations, structured water layers can form, e.g., ice-like layers [198]. These water layers have a considerable effect on the electronic properties of graphene, because their dipole moments are aligned in the same direction. The magnitude of the dipole moment of the water layer depends on the regularity and thickness of the structured water layer.

Often, the ordering and distribution of the water molecules in the interfacial layer are determined by the substrate. A change in the doping level and hysteresis behavior was observed in a graphene field effect transistor, when the SiO_2 substrate was coated with a hydrophobic self-assembled monolayer [286]. As the hydrophilic nature of the substrate was altered, it was proposed that there was no interfacial water layer present, reducing the doping and hysteresis behavior within the graphene.

The first direct evidence in favor of charge doping of graphene due to an interfacial water layer was measured and visualized with Raman spectroscopy [12]. Raman spectroscopy is often used to determine the doping and strain within 2D materials by tracking the frequencies of the G (ω_G) and 2D (ω_{2D}) Raman bands [112]. A freshly cleaved mica substrate induces hole-doping on graphene by permanent charge transfer [124]. When an interfacial water film of approximately 4 Å is present, the induced doping is effectively suppressed [12]. The Raman spectrum is similar to that of freestanding graphene. Absence of the H_2O layer led to a clear shift of the G and 2D peaks in the Raman spectrum indicative of p-type doping (Fig. 18a–b). The spatial maps (Fig. 18c–e) of the Raman response show the same consistent correlation between the charge doping in the graphene layer and the absence of interfacial water.

Interfacial water layers do not only suppress the amount of doping within the graphene coating, but also induce doping [197,279]. Trapped nanometer-sized water clusters between graphene and Au(111) induce localized electron doping in graphene (see Fig. 19) [197]. Spatially resolved density of states maps reveal a significant contrast at the locations where water clusters are trapped, Fig. 19a–c. A noticeable shift in the Dirac point toward the negative sample bias was observed when the tip moves across graphene-covered water clusters (Fig. 19d–g). The shift increases sharply and flattens on top of the clusters. The strength of the shift is dependent on the size of the water cluster, indicating that the amount of doping is directly

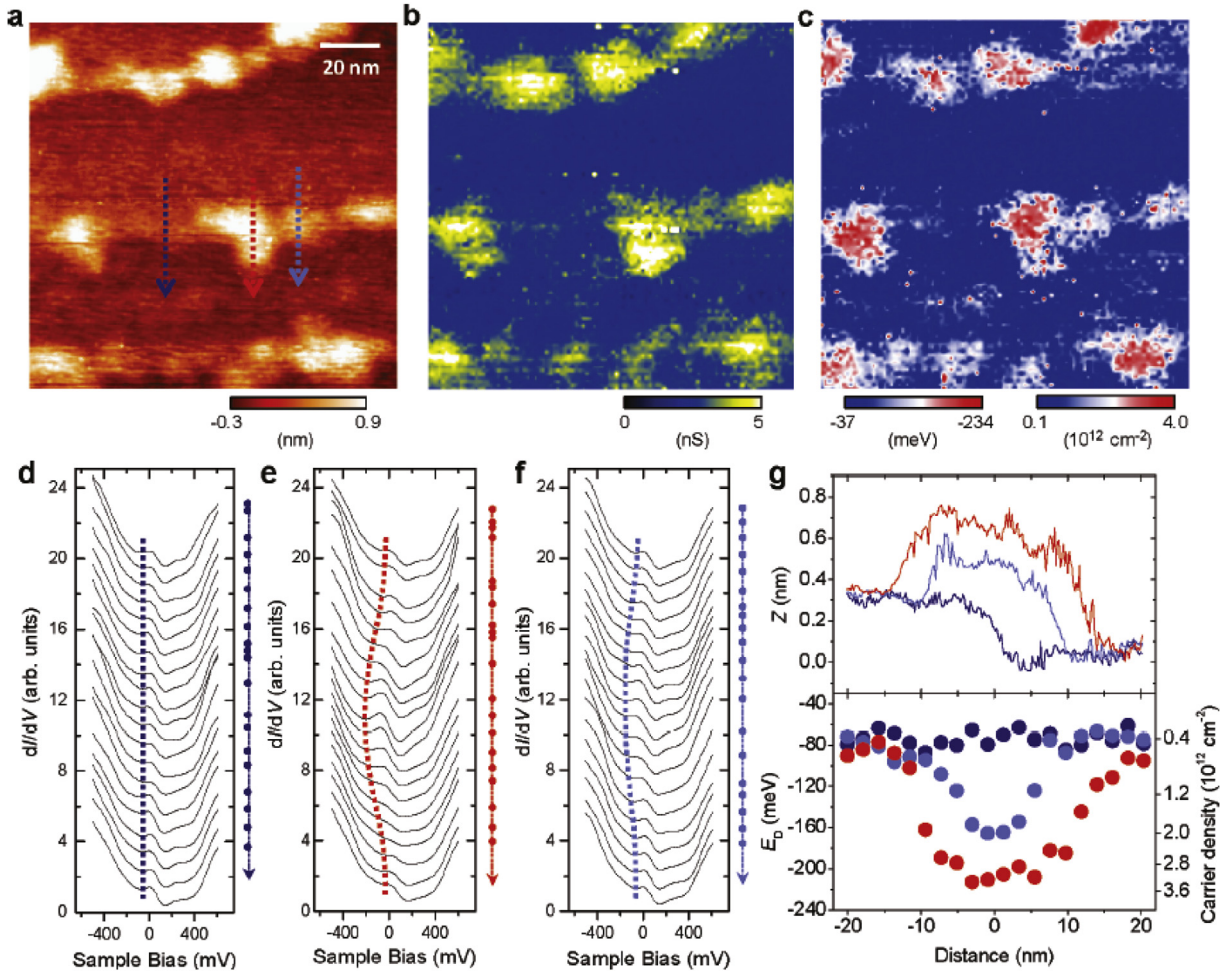

Fig. 19. Water clusters lead to highly localized doping in graphene. (a) STM topograph of a small region of the graphene-covered Au(111) surface. (b) dI/dV map of the same area at a fixed bias voltage of $V_B = 0.36$ V, obtained at 77 K. (c) A map of the same area for the measured energy position of the Dirac point, $E_D = eV_D$ (left color scale) and the extracted local charge carrier density (right color scale). (d) STS spectra along the dark blue arrow in (a), across a graphene-covered Au step where no water cluster was present. The spectra are vertically shifted for clarity. The shift in the Dirac point was minimal, as indicated by the dark blue dotted line. (e) STS spectra along the red arrow in (a), across a large water cluster covered by graphene. The shift in the Dirac point is tracked by the red dotted line. (f) STS spectra along the light blue arrow in (a), across a small water cluster covered by graphene. The shift in the Dirac point is tracked by the light blue dotted line. (g) Upper panel: Height profiles along the three arrows in (a). Bottom panel: E_D along the three arrows in (a). The values of E_D and its errors (smaller than the size of the symbols) were obtained from d–f. The corresponding local doping level is labeled on the right axis. Reprinted with permission from Ref. [197]. Copyright 2012 American Chemical Society. (For interpretation of the references to color in this figure legend, the reader is referred to the Web version of this article.)

controlled by the size of the water cluster. In contrast, no influence of the step edges on the Dirac point was observed.

The local density of water molecules can be controlled by changing the host substrate and the RH during the preparation process [168,279,287]. More hydrophilic substrates were found to induce a larger blue-shift in the frequency of the G Raman band, indicating higher doping of the graphene. As the hydrophilic substrate hosts more water molecules, more doping is induced on the cover, in good agreement with the observations on Au(111) [197].

Adding or removing water has the same effect as altering the substrate. A clear transition in the carrier concentration was found when the SiO_2-graphene system is emerged in water [160]. The recovery of the ω_G peak towards freestanding graphene starts first at the edges, where water enters the SiO_2-graphene interface, and spreads into the interior. When water completely wets the interface, no further changes were observed, even when the sample was moved to ambient conditions.

This process was further investigated with graphene deposited on SiO_2 and plasma cleaned SiO_2 surfaces [287]. On the SiO_2 surface, a blue shift of the ω_G and ω_{2D} band was observed when the interfacial water layer was removed by annealing the substrate. In contrast, on the plasma etched SiO_2 substrate, a red-shift of the Raman peaks was observed. The hydrophilicities of the surfaces are different (70° and 8°, respectively) leading to a different ordering of the water layer. It was suggested that an ordered polarized water layer can form on a plasma etched SiO_2 wafer as it contains Si—OH (silanol) end groups. The polarized layer induces p-doping due to the aligned dipole moment of the water molecules. An untreated SiO_2 substrate contains Si—O—Si (siloxane) groups and does not allow the water to form ordered structures [288]. In the latter case, the water screens the hole-doping from the SiO_2 to the graphene. This screening vanishes after the annealing of the sample and the subsequent removal of the water layer (explaining the blue shift of the ω_G and ω_{2D} Raman peak).

Moreover, the number of H_2O layers plays a crucial role in doping the graphene [119,289]. For two to three hydration layers, hole doping is induced in the graphene, owing to the formation of a net dipole moment in the hydration layers. This draws the graphene electrons slightly toward the hydration layer. When the amount of layers increases further, no noticeable dependence was observed in

the doping level, possibly due to a hydrogen bond disorder in the multilayer films.

Electrostatic force microscopy (EFM) has been deployed to study the influence of intercalated water on the 2D material cover [290–293]. For increasing graphene thickness, the influence of the adsorbed water is screened more effectively [291,293]. EFM measurements of multilayer graphene reveal an increase of the phase shift towards the bulk constant [293,294].

Although the influence of an interfacial water layer on the electronic properties of the 2D material coating is clearly present [12,168,197,279], the exact order and distribution of the water molecules within the clusters, droplets and layers are unknown. The ultraflat nature of mica and the conformity of graphene allow for the direct visualization not only of the interfacial water layer but also of the K^+ ion, which induces local doping variations on the graphene [124,125,295].

Nanoscopic measurements on the graphene-mica system show local doping variations depending on the exact configuration of the potassium ions on the mica surface. Depending on the local K^+ ion concentration the mica has three distinct local surface charge environments: positive, negative and neutral [124]. Two plateaus were found in the topography [295]. One plateau was attributed to a water monolayer and the other to potassium ions. Above the water, the graphene was insulated from charge doping while p-type doping was observed in the surrounding areas. Above potassium ion islands, n-type doping was observed.

Lin et al. [113] demonstrated that when the monolayer of water enters the mica-graphene slit pore, the D' Raman peak of graphene disappears and recurs only when the water film dewets the slit pore. The occurrence of the D' peak was activated by the direct contact of the graphene with the K^+ ions, while the disappearance of the same peak was caused by the intercalated water that decouples the graphene from the mica. From the shifts of the ω_G and ω_{2D} Raman peak positions, it was proposed that the water monolayer reduces doping and strain on graphene, which in the dry state is induced by the K^+ ions.

A Kelvin probe microscopy study shows that it is impossible to completely remove the first layer of water [129]. As the substrate was heated, both water on top of the graphene as well as interfacial water evaporated. This led to a change of the electronic properties of the graphene [129,296]. Water islands on top of the graphene led to a decrease of the surface potential by 200 mV and they were easily removed by heating the substrate to 180 °C. The intercalated water layer was only partly removed at the edges of the single layer graphene. Here the graphene was in direct contact with the mica and the surface potential was increased with 0.17 eV, i.e., the graphene coating is locally p-doped owing to charge transfer from the mica substrate. When the substrate temperature was further increased to 600 °C, the surface potential of the graphene dropped on areas where water was removed as well as on areas where water was still present. The n-type doping was induced by a change of the mica surface toward an electronegative surface by a rearrangement of the potassium ions [124] and by the creation of defects on graphene.

The stability of the first interfacial water layer at high temperatures and low humidity was attributed to its crystalline form [84,106,120,297]. dI/dV spectroscopy performed on the surrounding double layer of water reveals a small shift of the Dirac point of about −50 mV [106]. The double water layer has effectively no net dipole moment due to disorder and consequently zero effect on the electronic properties of the graphene cover [284]. In contrast to the double water layer, the first monolayer induced a large positive shift (+370 mV) of the Dirac point, suggesting a ferroelectric ice-like layer. The p-type doping is a result of the dipole orientation of the 2D ice crystal formed on the mica surface [84,297].

This doping variation on graphene between a monolayer ice and a double water layer was visualized by C-AFM [125,126,298]. The double water layer is substantially less conductive compared to graphene over the crystalline ice layer, owing to the difference in the density of states [106]. As the density of states is higher on the doped graphene, a higher conductance was measured [125,126]. Moreover, on top of the ice layer, small variations in the conductance were observed [125]. This difference was attributed to local variations in charge transfer induced by the presence of potassium ions. The K^+ ions distribute non-uniformly on the mica surface but were aligned with the mica lattice. A coverage of approximately 50% was measured. Graphene above sites without K^+ was effectively more conductive. This was attributed to the accumulative negative charge from both the mica and ice.

When pressure was applied to the ice crystals, the conductivity of the graphene layer decreases [126]. This was attributed to a pressure induced liquid-solid phase transition of the ice layer. At places where the ice melts into a quasi-liquid layer, the measured conductivity drops, as a result of disorder [120]. When the pressure is lifted, the ice crystals reform and the graphene is doped again. C-AFM images can also show features not present in the topographic AFM image. For instance, pinholes within the water layer were observed only in the conductance image while no features were seen within the topography image [298]. These pinholes were attributed to the different tip-graphene electrical contact at specific locations which lead to different junction characteristics.

Besides the electronic properties of 2D materials, also the optical properties alter due to the presence of interfacial water. Using photoluminescence (PL) imaging spectroscopy, the optical response of transition metal dichalcogenides (TMDCs) under the influence of interfacial water was measured [299–301]. For water-free regions of the single layer MoS_2-mica system, a strong fluorescence feature was observed around 1.88 eV and a weaker feature around 1.96 eV [300]. Both features were attributed to spin-orbit splitting of the valence band. For regions in which the MoS_2 covers a water layer, the PL feature at 1.88 eV is reduced in intensity by a factor of 50 and is slightly red-shifted to approximately 1.86 eV. In addition, the peak shape transforms from Lorentzian to Gaussian (heterogeneously broadened). This quenching of the MoS_2 excited states was mainly associated with trion formation [300].

Control over the spatial distribution of the intercalated water leads to local manipulation of the electronic properties of the cover material. Interfacial water offers a direct control of the electronic structure by altering the electronic charge in the neighborhood of the 2D material. A rich array of specific substrate architectures can be envisioned that could be used to tailor the 2D material's electronic properties to a variety of applications, such as local p-n juctions at ambient conditions. However, complete control is still lacking as it is difficult to make stable structures within the interfacial water layer.

6.2. Friction

2D materials are of increasing interest in tribology because of the large reduction of friction forces leading to the thinnest solid-state lubricant and anti-wear coating present today [302]. Together with the relative ease of preparation, the crystalline structure and the inertness with the environment, these materials are an ideal playground for testing basic concepts in tribology and the influence of water on the friction properties [303–305]. The underlying substrate, and therefore interfacial water, plays an important role for the friction properties [303,306–308]. The frictional properties of 2D materials are unique, for instance, exfoliated graphene flakes on silica substrates exhibit flexural deformations that strongly influence friction via puckering effects and out-of-plane deformations [309].

Water molecules intercalated at the interface inevitably alter the friction properties of the system. The interfacial friction of water depends for example on the surface curvature [310], atomic struc-

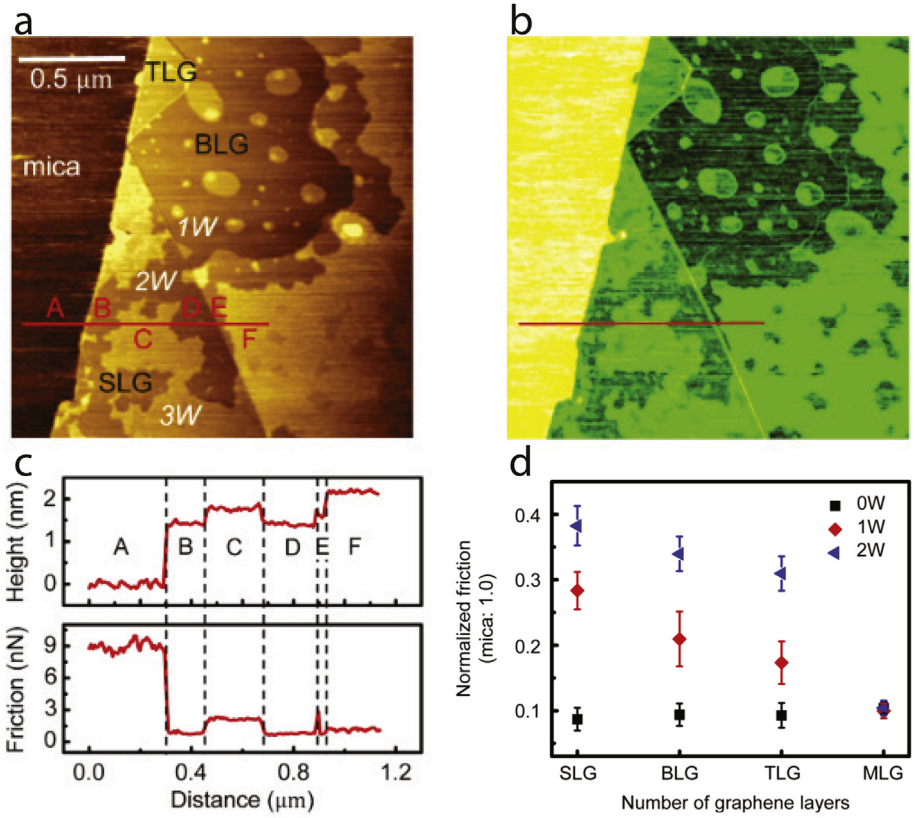

Fig. 20. a) Topography and (b) friction images at an applied force of 9.6 nN (1.8 μm × 1.8 μm) of water intercalated graphene on mica after 81 h of exposure to high RH (above 95%). (c) Line profiles of height and friction along the A-F line in (a) and (b). (d) Plot of the friction force, normalized to the value for bare mica (=1) for zero (0W), one (1W), and two (2W) water layers intercalated between the graphene and mica as a function of the number of graphene layers (i.e., single-layer graphene (SLG), bilayer graphene (BLG), trilayer graphene (TLG), and multi-layer graphene (MLG)). Reprinted with permission from Ref. [316]. Copyright 2017 American Chemical Society.

ture [311] and mechanical strain [312]. Moreover, water alters the resonant frequency of graphene oxide and the mechanical resistance to oscillations is enhanced [313].

The exact configuration of the water layer affects the friction properties of the coating material [126,314]. A reduction in friction is observed when water intercalates between graphene and SiO_2 [121], indicating that the water acts as a subsurface lubricant, as predicted by theory [315]. Ripple-like structures were observed in AFM friction images on graphene above ice crystals. The ripple-like structure is caused by the underlying ion-distribution on the mica surface [124].

The presence of water also enables the possibility to disentangle the excitation of atoms at the interface of the rubbing bodies and the energy transfer process of the vibrational energy from the interface into the bulk [316,317]. Fig. 20a and b show the shapes, heights and friction of various regions of intercalated water between graphene and mica [316]. The friction image shows contrast variations depending on the water and graphene layers. Clear steps were observed in the friction profiles (Fig. 20c) in the different regions. The friction coefficient increases with an increasing number of interfacial water layers. The friction of graphene is sensitive to the underlying water layers, due to two important and fundamental processes responsible for the energy dissipation in the friction process. Firstly, due to the presence of water layers, the graphene sheet is interacting less with the mica substrate, and therefore more vibrational modes are available enhancing the friction. Secondly, the effective energy transfer via the O—H vibrations of the water molecules toward the substrate changes depending on the number of water layers and their exact configuration [316]. For multilayer graphene, no change was observed in the friction force as a function of the number of interfacial water layers. Multilayer graphene effectively screens the water underneath and thus has less effect on heat dissipation [316].

6.3. Nanomanipulation

The structure, formation and manipulation of water films on surfaces play crucial role in wetting, corrosion, nanofluidics and other phenomena. For instance, water films on mica could be perturbed using an AFM/STM tip [83,318,319] or ice structures can form between an AFM tip and HOPG by applying a local pressure [195]. Although the interfacial water layers are protected by a two-dimensional coating, it is still possible to manipulate them. Graphene coating allows to manipulate intercalated water layers with an STM at room temperature [106,122]. Fig. 21a and b show an STM image of one, two and three water layers under graphene before and after manipulation [122]. When a negative voltage pulse was produced, a pinhole was created which penetrated through the third and second layer. The size of the pinholes can be partially controlled by adjusting the electron dose and bias potential. However, the shape and non-uniformity are random. The first water layer could not be manipulated because of its crystalline structure and the strong adhesion with the hydrophilic mica surface. During the manipulation process, the graphene remains undamaged implying that tunneling electrons do not interact with the graphene but directly tunnel into the water hydrogen bond. However, the exact tunnel mechanism is not yet clear.

A way to manipulate the first monolayer is by exposure to elevated temperatures. At 100 °C, the ice crystals become coarser and their edges smoother, indicative of edge melting [106]. Another

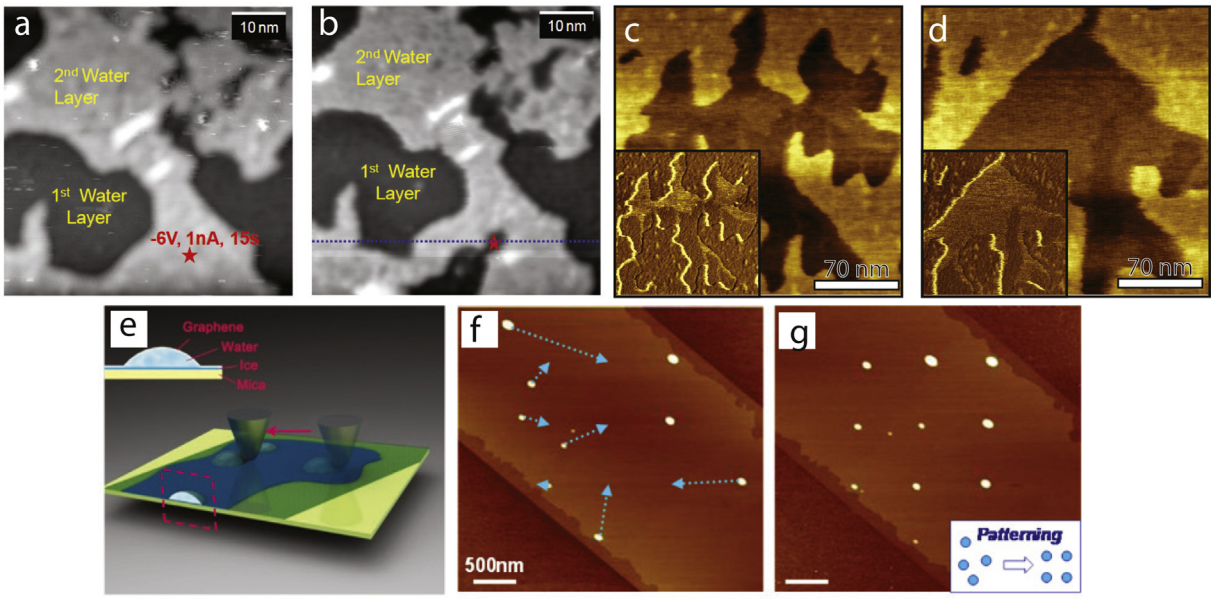

Fig. 21. (a) Topographic image of the second water layer before and (b) after nanomanipulation at negative sample bias. The created pinhole is nonuniform, though it is localized to where the tip was centered. Scanning conditions were −0.35 V sample bias and 1 nA tunneling current. (c–d) A sequence of AFM topographic images ($230 \times 230\,nm^2$) and in the insets the corresponding LFM images showing the dynamic behavior of the ice fractals when there is pressure applied using an AFM tip. The applied pressures are approximately 8.5 and 9.7 GPa. (e) Schematic for the manipulation of a water nanodroplet (WN) by an AFM tip. Inset shows the sandwich structure of graphene/WN/mica. (f–g) With a multistep translation, the disordered nanodroplets are rearranged into an ordered 3×3 array. The blue dotted arrow (the same below) represents the path of the tip we preset. ((a–b) Reprinted with permission from Ref. [122]. Copyright 2012 American Chemical Society. (c–d) Reprinted with permission from Ref. [126]. Copyright 2017 American Chemical Society. (e–g) Reprinted with permission from Ref. [320]. Copyright 2014 American Chemical Society). (For interpretation of the references to color in this figure legend, the reader is referred to the Web version of this article.)

method to manipulate the first monolayer is by applying locally very high pressures. Using an AFM tip in contact mode, water layers on HOPG can turn into an ice-like structure by applying a pressure with the AFM tip [195]. The same principle was used by Sotthewes et al. [126] on the graphene-mica system. Pressures in the order of a few GPa led to melting of the monolayer ice [126]. Fig. 21c–d shows a sequence of AFM images recorded at different applied pressures. Above approximately 6 GPa, a third contrast appeared within the fractal area (the ice crystal). It appeared first at the edges (boundary between the ice crystal and the double water layer) and then spread into the interior. The emerging layer was interpreted to be a quasi-liquid layer of water since no structure was observed (fuzzy appearance in the friction images, insets of Fig. 21c–d). The process was reversible, the quasi-liquid layer transformed back into an ice layer when the applied pressure was lifted.

AFM can be used to manipulate water nanodroplets confined between graphene and mica (see Fig. 21e–g) [320]. These water nanodroplets were present on an ice-like layer and were very stable; no visible changes were observed for a duration of two months at ambient conditions. When a sufficiently high external force was applied by the AFM tip in contact mode, the nanodroplets could be directly moved to form regular arrays. In addition, droplet coalescence and splitting were possible. The nanodroplets can be transported freely to every position, as long as it takes place on top of the ice-like layer. At the border of the ice-like layer, the nanodroplets were pinned. Droplets of the size of yoctoliters can be created and transported around the surface. The authors found that droplets without a 2D-ice layer underneath could not be moved by the AFM tip. This indicates that the 2D-ice layer acts as a lubricant layer. The manipulation of water confined between two surfaces can act as a new route toward nanofluidic transport for various fields including 'lab-on-a-chip' technology.

Manipulation of the 2D material is also a possibility. When the complete graphene-SiO_2 system was emerged in water, the hydrophilicity of the host surface defines whether the coating material remains on or detaches from the surface and often rapidly scrolls [160]. When SiO_2 is used as the host substrate, the graphene-water-substrate system remains intact up to several months. In this case, the graphene sheet was completely surrounded by water. If the confined water layer is rigid, it serves as a solid-like substrate and keeps the graphene sheet in position due to Van der Waals interaction [321]. When the SiO_2 surface was plasma etched, the graphene coating immediately detached or transformed into a scroll. If the intercalated water film is more liquid-like, the graphene sheet is surrounded by water and it is lifted from the surface. Since the graphene is completely surrounded by water, scrolling is strongly favored to minimize the free energy of the system [322]. Wrinkle formation is another phenomenum that can occur after diffusion and evaporation of water from the graphene-SiO_2 interface [158]. When the water evaporates quickly in a dry environment, the graphene coating does not regenerate to its original shape but instead collapses with the subsequent formation of wrinkles. In this process, the substrate plays an important role, as wrinkle formation was not observed for graphene on mica [158]. This was attributed to the lower evaporation rate from the graphene-mica interface owing to mica's hydrophilicity and flatness.

Although a lot of progress is made on the understanding of the influence of interfacial water on the cover material, and the consequence of nanomanipulation, further research is needed to obtain a complete picture of the involved processes. For example, can the number of interfacial layers be controlled by manipulating the cover? And to what extent? Is the process reversible? Can interfacial water be used as a lubricant in non-ambient environments? Can we tune the structure of the interfacial water to obtain well-defined and controlled doping levels on the 2D material cover? Is patterning of the water structure below the cover possible to fabricate novel (opto)electronic devices? In the following section, we explore some

of the possibilities that confined water offers toward novel applications and improvement of known concepts.

7. Applications of confined water

Perhaps one of the most promising applications of confined water is desalination. Desalination is the process of sieving ions using membranes. This can for example be useful for converting salt sea water into drinkable water. 2D materials are a promising class of membrane materials for desalination. Nanoporous graphene can for example be used for water desalination [323–327]. The same holds for a multi-layered stack of graphene-oxide [261,328–330]. Abraham et al. were able to control the interlayer spacing in graphene-oxide, thereby tuning the ion sieving [331]. In this context, the diffusion dynamics of water through these membranes, as we show in section 5, define the membrane functionality. For a more comprehensive and detailed review on this topic we refer to the work of Werber et al. [332].

Another very important application is blue energy. Blue energy is referred to the process of harvesting energy from a salinity gradient, e.g., between sea water and river water. There are two main processes to extract energy from the salinity gradient: pressure retarded osmosis (PRO) and reverse electrodialysis (RED). In PRO, separation of fresh and salt water with a membrane results in an osmotic flow which is used to move a turbine. In RED, anions and cations are separated under a concentration gradient by flowing ions along alternating anion-selective and cation-selective membranes, resulting in a net electric transport. Current harvesting techniques have a low energy efficiency, mainly due to inefficient membranes. 2D materials are a promising class of membrane materials [333,334] and the structure and dynamics of water confined in these 2D membranes define its efficiency. Energy conversion densities three orders of magnitude higher than conventional methods have been obtained [335]. For further information on this topic we refer the reader to the work of Siria et al. [336].

In this section, we discuss other applications of water confined between 2D materials. We start with describing graphene nanobubbles, we continue with explaining how graphene liquid cells work, followed by the introduction of capacitive sensing. After this, we touch on the transfer of graphene facilitated by water intercalation. We conclude this section with a description of the liquid phase exfoliation method.

7.1. Graphene nanobubbles

There are a variety of methods to create small encapsulated gas volumes covered by graphene, the so-called graphene nanobubbles. Lim et al. [337] entrapped water molecules between graphene and diamond. Their graphene-diamond sample was heated to ~1275 K for 45 min, which is the reconstruction temperature of diamond. The graphene then covalently binds to the diamond, resulting in entrapment of the water molecules. The graphene-water-diamond system is called a hydrothermal anvil cell. Graphene nanobubbles with a density of $\sim 8 \times 10^{10}$ cm^{-2} appeared. In situ Fourier-transform infrared spectroscopy (FTIR) was used to confirm the presence of water in these nanobubbles. The water between the graphene and the diamond was found to be in a supercritical state. This supercritical water is very corrosive and etches the diamond surface, resulting in square-shaped voids. The graphene nanobubble has been transformed into a hydrothermal reactor. The pressure inside these graphene nanobubbles was estimated to be ~1 GPa. In a follow-up study, Lim et al. [338] used the graphene-diamond anvil cell to establish high-pressure chemical reactions. With infrared (IR) spectroscopy they observed the polymerization of buckminsterfullerene (C_{60}) in the graphene nanobubbles. This confirmed the high pressure in the nanobubbles since this reaction is only possible under high pressure and at high temperatures.

Kayal et al. [339] did molecular dynamics simulations on the confined water system described by Lim et al. [337]. They found similar vibrational spectral features and high water relaxation times in nanobubbles with a high water density. On the contrary, low water relaxation times were found in low water density nanobubbles.

In the method described by Dollekamp et al. [340], confined water was used to create hydrogen nanobubbles between graphene and mica. They reduced confined water between graphene and mica to hydrogen gas, which resulted in the nucleation of nanobubbles. The authors achieved this reduction of water by placing the sample in an electrochemical cell and applying a voltage to the graphene. The nanobubbles had a typical radius of a few hundred nanometers and a height of a few tens of nanometers. This resulted in pressures in the order of a few MPa inside the bubbles. The nanobubbles grew over time until a dynamic equilibrium was established between hydrogen formation in the nanobubble and hydrogen dissolution into the confined water film. Eventually, the growth of these nanobubbles led to the delamination of graphene. The nanobubbles preferred to nucleate at the locations of bottom (B-type) step edges and defects. At these locations, more water is available to promote ion transport.

A similar method was used by An et al. [341]. They reduced water between layers of highly oriented pyrolytic graphite (HOPG). In their work, 10 mM Na_2CO_3 and NaCl were used as the electrolyte. The pressures they obtained were in the range of 20–50 MPa. Gravimetric hydrogen storage capacity calculations also showed that these graphene nanobubbles have the potential to be used for hydrogen storage. A hydrogen capacity of ~21 wt % was estimated for monolayer graphene nanobubbles.

7.2. Graphene liquid cells

In order to study the growth dynamics of bubbles in water at the nanoscale without perturbing the bubble-water interface, for instance by an AFM tip, encapsulation with graphene is essential. This was demonstrated by Shin et al. [342]. They studied in-situ nanobubbles in water encapsulated between two graphene layers with UHV TEM. A schematic illustration of the graphene liquid cell is given in Fig. 22a–b and UHV-TEM images of the nanobubbles are shown in Fig. 22c-d. The graphene encapsulation prevents the gas dissolution into the UHV-TEM chamber since graphene is impermeable to gases. A critical radius of 6.3 ± 0.8 nm was found for the nanobubbles. Nanobubbles below this size dissolved into the confined water within a minute. Nanobubbles above this size remained stable for ~10 min. Two distinct growth mechanisms were observed: Ostwald ripening and coalescence. During the Ostwald ripening, the smaller nanobubbles shrink, while the larger grow even more. During the coalescence, an ultrathin water membrane appears between two nanobubbles, which results in unhydrated gas transport. In a follow-up study, Park et al. [343] studied this merging process in detail. They discovered that the radius-dependent Laplace pressure and distance-dependent gas density were important factors in determining the merging of nanobubbles. These graphene liquid cells have already been applied, for example, to visualize platinum nanocrystal growth at unprecedented resolution [206]. Furthermore, graphene liquid cells can also be used to study nanocrystal-DNA nanoconjugates, which opens the door toward the study of biological samples [344].

7.3. Capacitive sensing

Olson et al. [170] used a metal-oxide-graphene variable-capacitor (varactor) structure consisting of graphene on HfO_2 to probe water intercalation. When the humidity was increased, water intercalated

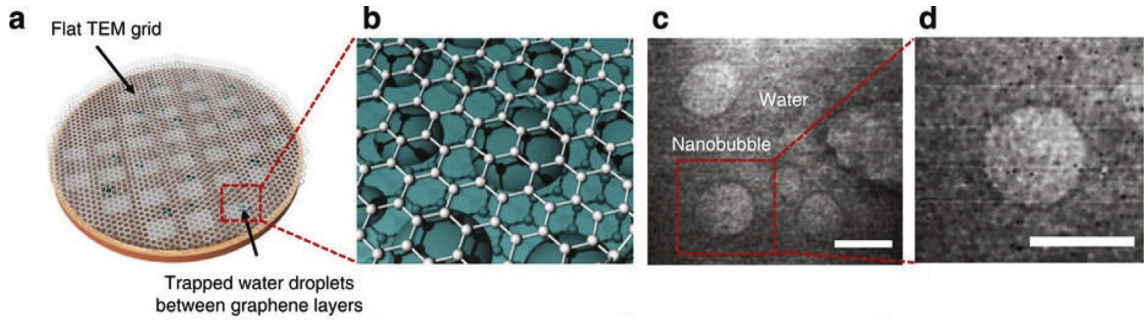

Fig. 22. (a–b) Schematic illustration of the graphene liquid cell. (c–d) In-situ UHV-TEM images of the confined nanobubbles between graphene. Scale bars, 10 nm. Reprinted with permission from Ref. [342]. Copyright 2015 Nature Publishing Group.

between the graphene and HfO_2, which resulted in a difference in capacitance. This process was found to be reversible on a short time scale. At high humidity, an n-type doping shift of the Dirac cone in the capacitance-voltage curve was observed, which indicated water intercalation. The authors further confirmed the water intercalation by using pulsed force mode AFM. They observed an increased separation between graphene and HfO_2. Additional DFT and MD simulations [170] validated their experimental observations. The sensitivity of varactors to water intercalation could potentially lead to graphene-based sensors.

7.4. Transferring graphene by water intercalation

Water plays an important role in the transfer process of graphene from a growth substrate to a target substrate. In this section, we elaborate on how confined water is used in different transfer methods. For a more comprehensive review on this topic, we refer to the recently published work of Seah et al. [345].

Schneider et al. [346] developed a method to transfer mechanically exfoliated graphene on SiO_2 by water intercalation, the so-called wedging transfer technique. In their method, they brought a hydrophobic polymer layer on top of the graphene and then immersed the system in water. After the polymer with the graphene detached from the SiO_2 due to water intercalation, it was positioned on the target substrate. When the polymer is dissolved, the graphene remains on top of the target substrate. A similar method was developed for MoS_2, where water intercalation between MoS_2 and a sapphire substrate resulted in the detachment of a polystyrene coated MoS_2 layer [347].

The bubbling transfer method is another technique to transfer graphene [348]. In this method, electrochemical means are used to detach graphene from a substrate. First, a substrate with CVD graphene is coated with polymethyl methacrylate (PMMA). The use of PMMA prevents the graphene from rolling or tearing during the delamination process. Thereafter, the sample is immersed in water. The water intercalates between graphene and the substrate. When a negative potential is applied to the substrate, the confined water is reduced to hydrogen gas. This results in the nucleation of (nano)bubbles with a high internal pressure. These high-pressure bubbles cause the graphene to delaminate from the substrate. This method does not damage the graphene and is relatively easy to implement. Wang et al. [348] demonstrated the use of this bubbling transfer method on CVD graphene grown on a copper foil. Fig. 23(a) shows a schematic illustration of their setup. The copper foil is used as the negative cathode. Fig. 23(b–d) show the graphene delamination over time. Fig. 23(d) shows the successful detachment of the graphene/PMMA. The graphene/PMMA floats in the $K_2S_2O_8$ (0.05 mM) electrolyte. This method makes the Cu etching step abundant and creates high-quality graphene films. Also, the copper catalyst can be reused and the process can be scaled to an industrial level.

Gao et al. [349] used a similar approach to detach CVD graphene from a platinum foil. Compared to copper, the advantage of platinum is its almost unlimited lifetime. Copper is namely etched away for about 40 nm per cycle [348], making it a less sustainable material for graphene transfer. Using platinum as the substrate, the quality of the delaminated graphene is almost identical to the original CVD graphene on platinum. Their experiment was performed in a NaOH solution. The authors noticed that when using graphene as an anode, the graphene oxidizes. The bubbling transfer method has also been demonstrated for graphene/Ru [350] and h-BN/Pt [351,352] samples.

Gupta et al. [353] developed a method for exfoliating CVD graphene from copper and platinum substrates by only using hot deionized water, the so-called soak-and-peel delamination method. In their method, hot (90 °C) deionized water penetrates into the hydrophobic graphene-hydrophilic Cu/Pt interface and induces separation. This method gives high-quality graphene with reduced doping compared to transferred graphene using an etchant or electrolyte.

Verguts et al. [354] showed that water intercalation is critical to a direct graphene transfer. The authors found that graphene delamination with the bubbling transfer method was only successful when the sample was exposed to water priorly. Graphene delamination of samples unexposed to water, directly after CVD growth, were unsuccessful and resulted in heavy damage to the graphene. With STM, they showed that water layers intercalate between CVD graphene and $Al_2O_3(0001)/Pt(111)$ when the system is exposed to water. An STM image of these water layers between CVD graphene and $Al_2O_3(0001)/Pt(111$ is shown in Fig. 24. Before this STM image was taken, the sample was immersed in 50 °C water for 16 h. The water layers form a meandering pattern. With SEM and Raman spectroscopy the authors additionally confirmed that water intercalates between the graphene and $Al_2O_3(0001)/Pt(111)$.

Dollekamp et al. [355] investigated the dynamics of confined water between charged graphene and mica. They found that a negatively charged graphene surface promotes water intercalation. On the contrary, a positively charged graphene surface resulted in water being expelled from of the graphene-mica slit pore. They attributed this effect to the preferential orientations of the water molecules due to the confinement.

In their most recent work, Verguts et al. [356] looked at the ion intercalation between graphene and platinum. They found that the ion intercalation and not the bubble formation is the driving force for graphene delamination. Graphene delamination was tested in different electrolytes. Ions which resulted in successful delamination at the cathode where: Na^+, K^+, TMA^+, and TEA^+. In contrast, unsuccessful delamination at the cathode was observed with H^+, NH_4^+, and Ce^{4+} ions. The result can be explained by the difference in the electroreductive activity of the ions. The ions that delaminate the graphene have a more negative E^0 (standard reduction potential versus the standard hydrogen electrode) value com-

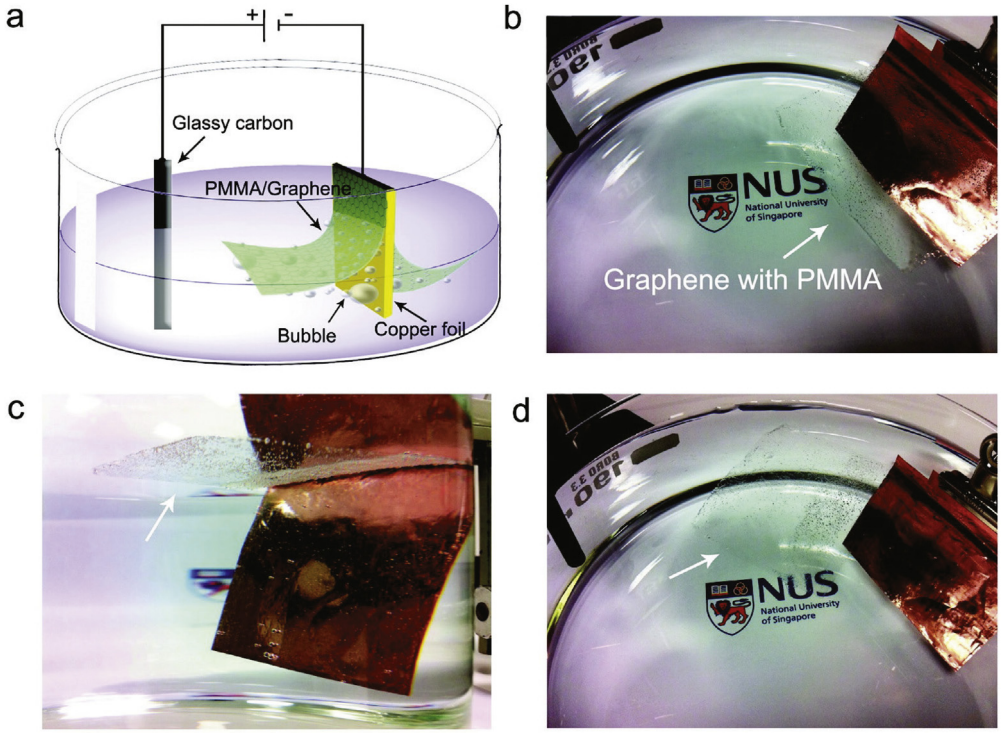

Fig. 23. (a) Schematic illustration of the electrochemical cell used for the electrochemical exfoliation. (b–d) Consecutive optical images of the graphene/PMMA being delaminated from the copper foil. The PMMA covered graphene eventually fully delaminates from the copper foil. Reprinted with permission from Ref. [348]. Copyright 2011 American Chemical Society.

pared to the E^0 value of water. Therefore, the ions can intercalate between the platinum and graphene, resulting in delamination of the graphene. The ions that not delaminate the graphene directly reduce to gases when coming in contact with the cathode. Ions with successful delamination at the anode where: NO_3^-, SO_4^{2-}, Cl^-, and SO_3^{2-}. Unsuccessful delamination at the anode was observed with OH^- ions. Again, the electroreductive activity of the ions is responsible for the difference in successful delamination. When the counter electrode was removed, and thus no current flows, the same successful delamination was achieved. In the situation without the counter electrode, even NH_4^+ causes delamination of the graphene since it cannot reduce to NH_3(g) anymore. The authors also noticed that delamination takes up to three orders of magnitude longer at positively charged electrodes, compared to negatively charged electrodes. This may be explained by water expelled out of the confined space between graphene and the positively charged platinum, similar to the observations made by Dollekamp et al. [355] for water confined between mica and positively charged graphene.

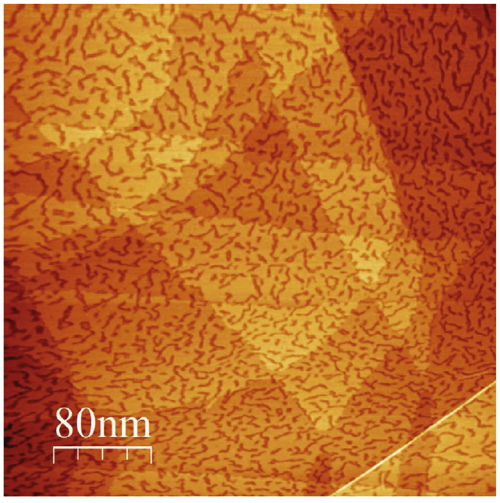

Fig. 24. STM image under ambient conditions of graphene on Al_2O_3(0001)/Pt(111). Meandering water layers are visible. The bias voltage is 105 mV and the current is 0.2 nA [354]. Copyright 2017 American Chemical Society.

7.5. Liquid phase exfoliation

There are several techniques to exfoliate graphene in the liquid phase [357]. Graphene can be exfoliated by oxidizing it with oxidizing chemicals to graphene-oxide, the so-called chemical exfoliation [358]. Its hydrophilicity allows water to intercalate between the graphene-oxide layers. Ultrasonication is then applied to agitate the layers. Afterwards, the graphene-oxide layers are reduced back to graphene. Besides water, also ions can intercalate between 2D materials [359,360]. The intercalation increases the spacing between the layers and thus lowers the interlayer attraction. Ultrasonication or thermal shock [361] can then be used to agitate the layers. This process is schematically depicted in Fig. 25(a). Ions could be exchanged in, e.g., clays, layered double hydroxides, and metal oxides [362]. These materials have counter-ions in between the layers to establish charge neutrality. The ions can then be exchanged for larger ions. This increases the interlayer spacing which is needed to agitate the layers with, e.g., ultrasonication or shear mixing. This process is schematically represented in Fig. 25(b).

Hernandez et al. [363] managed to exfoliate graphene from powdered graphite by means of liquid phase exfoliation. This method is also sometimes called sonication assisted exfoliation. The authors of reference [363] used solvents (e.g. N-methylpyrrolidone) with

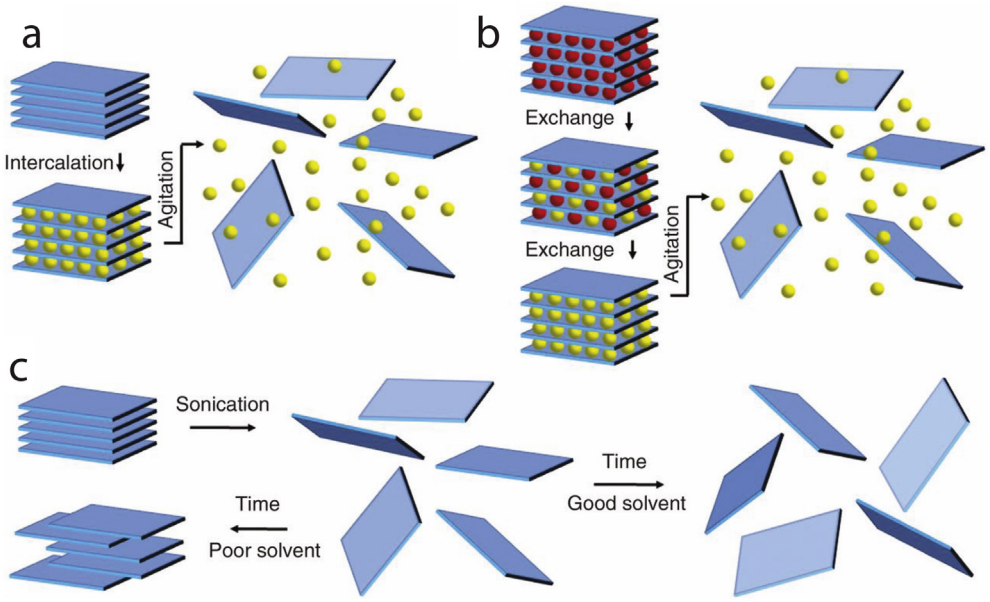

Fig. 25. Different liquid exfoliation methods. (a) Ion intercalation. (b) Ion exchange. (c) Sonication-assisted exfoliation. Reprinted with permission from Ref. [357]. Copyright 2013 American Association for the Advancement of Science.

a similar surface energy as graphene, leading to solvent intercalation between the layers in graphite. This intercalation results in an increased interlayer distance and lowering of the crystal cohesion. With ultrasonication, cavitation bubbles arise which agitate the layers. By choosing the right solvent, the layers are prevented from reaggregation. A monolayer yield of ~1 wt% was achieved. This process is schematically depicted in Fig. 25(c). The method has also been demonstrated to be successful for h-BN, TMD's and TMO's [364].

Su et al. [365] used electrochemistry to exfoliate graphene from graphite. They immersed a graphite electrode in sulfuric acid and then applied a potential to the electrode. This resulted in the intercalation of SO_4^{2-} ions in the graphite. Their obtained graphene sheets have a lateral size of 30 μm and exhibit a modest conductivity with a mobility of 17 $cm^2/V{\cdot}s$.

The influence of chemical, sonication assisted and electrochemical exfoliation on the remaining graphite was studied by Xia et al. [366]. They used AFM, Raman and X-ray diffraction to study the exfoliated graphene and remaining graphite. Sonication assisted exfoliation resulted in the best quality flakes and minimal damage to only the top layers of the remaining graphite. Since this method only exfoliates the top graphene layers, this exfoliation method is rather slow. Chemical and electrochemical assisted exfoliation are faster exfoliation methods and act in depth in the graphite. However, these methods resulted in more defects to the graphene.

8. Conclusions and outlook

The structure and dynamics of water under a two dimensional geometric confinement are of great significance due to its importance in water flow, surface chemistry, environmental sciences and material science in general. We have seen that the physical properties of water at an interface or in a nanopore are dramatically different from bulk water and strongly dependent on the fine details of the confinement. A systematic understanding of the influence of the confinement on this rich behavior was, until recently, poor because of experimental limitations to access interfacial water structures. The discovery that graphene is stable in its two dimensional form has opened new research possibilities and it has proved to be an instrumental tool for the investigation of confined water structures. Graphene's (and other 2D materials) remarkable mechanical and electronic properties combined with scanning probe techniques allow to directly visualize and measure water structures that are confined between graphene/2D material and a variety of supporting substrates. Information regarding the influence of the interface structure and wettability, environmental humidity, temperature, pressure and the presence of foreign species, on the structure and dynamics of confined water can now be experimentally accessed in situ and in real time with scanning probe microscopies.

Because of this, the understanding of two dimensional confined water has advanced greatly. In this review we have summarized several examples that underline the complexity of the structure and dynamics of confined water. The properties of confined water are highly sensitive to the nature of the confinement walls (mainly the surface structure), their separation distance as well as the temperature and pressure. Room temperature scanning probe investigations on 2D material covered water, along with non-invasive averaging techniques and computational models have provided new insights on the behavior and the state of confined water. Previous knowledge of water adsorption on metals obtained from DFT simulations in combination with LT STM investigations have provided a solid background and a starting point for understanding confined water. The original assumption that water assumes an intact $I_h(0001)$ bilayer structure [9,36] on metal surfaces has been already largely discarded [35,37,41,42]. These studies have shown that often the presence of the substrate is enough to destabilize the ice bilayer of natural ice in favor of a more energetically stable structure that optimizes water-water and water-surface interactions.

The earliest works on water between graphene and mica suggested that water assumes an ice-like structure resembling that of the I_h-ice bilayer. However, such a structure could not account for the observation of graphene doping. In addition, the presence of K^+ ions on mica would destabilize it. Therefore, modifications of this picture to an ice structure that follows closely the mica orientation was soon realized. Direct and conclusive evidence of the presence of the I_h-bilayer in two dimensional material confined water is still lacking. Similar to water adsorption on metal surfaces, other structures that optimize H-bonding seem to prevail. Recent evidence suggests that the nature of confined ice is indeed very complicated, with

experimental evidence for square ice, bilayer flat ice, and flattened monolayers further support this claim. This holds in particular for the remarkable observation of square ice in graphene nanocapillaries.

The influence of the first adlayer/monolayer on subsequent water adsorption has also been studied. The structure of the first monolayer has a profound impact to additional water adsorption/intercalation and therefore wetting of the interface. When the water molecules tightly bound to one of the confining surfaces, multilayer water adsorption is destabilized without the rearrangement of the H-bonding in the first monolayer. This could in turn result in 3D water clusters or droplets rather than multilayer growth. Similarly, when water adsorbs in a hydrophobic confinement it was shown to form self-closed H-bonded flat bilayers that destabilize further water adsorption. Square ice multilayers have also been observed and have attracted extended attention due to the observation of AA stacking in bilayer films. Such AA stacked square ice bilayers were not theoretically reproducible without a considerable refinement of the used computational models. In the case were multilayer growth is promoted, the structure of subsequent layers seems to maintain the signature of the first monolayer/surface, but with an increasing degree of disorder. An important aspect to keep in mind is that the nature of the studied confinement should disallow growth beyond a certain thickness, above which delamination of the 2D material cover would occur. Confined water shows a rich variety of dynamics. The mobility of water in hydrophobic-hydrophilic confinement is reported to be suppressed. Even though water within hydrophilic confinements remains disordered down to temperatures much lower than the bulk's melting point, in subnanometer confinements it displays high viscosity. In addition, water between graphene layers has shown to be highly mobile and at the same time keeps its crystalline structure without any sign of melting, even under the influence of a high energy electron beam.

However, even though experimental investigations of confined water have bloomed and some aspects of the underlying physical processes have become clearer, there is still uncertainty about the local hydrogen bonding. With respect to that, direct experimental investigations are extremely difficult to explore due to limitations induced by the confinement. Indirect knowledge comes from only spectroscopic tools, such as scanning tunneling spectroscopy. While there is a good understanding about the average structure of confined water, the local molecular arrangement as well as water-surface and water-water bonding and mixed OH/water are still not clear. This is perhaps the biggest experimental challenge, since the 2D material cover makes it almost impossible the direct visualization of the molecular arrangement and the relevant bonds. New and novel experiments capable of probing and visualizing the local arrangement of water molecules along with refined calculation models are essential for a breakthrough in this problem. Hexagonal boron nitride (h-BN) may provide a solution to this experimental challenge. Covering the water structures with a 2D material with a large band gap, like monolayer h-BN, could be instrumental. Since it can allow for molecular imaging of the confined water by for instance tunneling through it with an STM tip, and at the same time it can still provide the required confinement. In addition, it is necessary to further explore multilayer growth in nanoconfinement and further study the role of the cover. To that extent, new investigations of confined water in between different materials are necessary. The 'pressure-temperature-wall separation' phase space needs to be expanded. Additional experiments are therefore necessary. Luckily graphene and 2D materials allow to explore in situ water structures at a large range of temperatures and pressures without deterioration.

We have also reviewed the influence of interfacial water on the 2D material cover. The structure of the interfacial water which plays a significant role. In the case of a ferroelectric ice film, the cover material is shown to be doped due to charge transfer. For disordered layers, this doping is either absent or significantly less. Disordered films also have the potential to screen charge transfer from the underlying surface. It is not difficult to envision, that direct control of the interfacial water structure could give an extra dimension in controlling locally the electronic landscape of the 2D material cover. We have reviewed examples showing that such manipulation is possible, e.g., tip manipulation with SPM, pressure and temperature induced modifications as well as substrate functionalization. In addition, evaporation and intercalation of water have also shown to induce structural and frictional changes to the cover, with the formation of wrinkles, folds and bubbles.

We have concluded this review by showing a few examples of how confined water can be used in applications. Here, we showed that interfacial water plays a significant role in graphene/2D material delamination and exfoliation as well as transfer processes. Moreover, the growth of nanobubbles with high internal pressures offers a great 'laboratory' for studying reactions at the molecular level. To summarize, confined water between two dimensional materials has already a variety of applications and new possibilities are foreseen in the near future.

We close this review by emphasizing again the complex nature of confined water. A complete understanding requires the proper inclusion of hydrogen bonding and water-surface interactions in the 'pressure-temperature-wall separation' space. STM/AFM/TEM along with DFT and spectroscopic techniques have provided a coherent but still incomplete picture of confined water. The observed phase behavior, phase transitions and dynamics of the confined water structures underline the complexity of the governing physical mechanisms. It is clear that the behavior of the water molecules depends heavily on the confinement characteristics. An all-inclusive picture of the state of water under confinement cannot be drawn yet and the confinement details and conditions should be considered more deeply in future investigations. Further investigation of confined water may reveal different local H-bonding structures, providing additional information and improving our understanding of how water behaves under two-dimensional confinement.

Acknowledgments

P. B. thanks the Netherlands Organisation for Scientific Research, NWO, (FOM, FV157 14TWDO07 and STW 11431) for financial support. E. D. thanks the Netherlands Center for Multiscale Catalytic Energy Conversion, MCEC, an NWO Gravitation programme funded by the Ministry of Education, Culture and Science of the government of the Netherlands.

References

[1] V.F. Petrenko, R.W. Whitworth, Physics of Ice, OUP, Oxford, 1999.
[2] G. Malenkov, Liquid water and ices: understanding the structure and physical properties, J. Phys. Condens. Matter 21 (28) (2009) 283101.
[3] K. Libbrecht, The enigmatic snowflake, Phys. World 21 (1) (2008) 19–23.
[4] K.G. Libbrecht, The physics of snow crystals, Rep. Prog. Phys. 68 (4) (2005) 855–895.
[5] J.N. Israelachvili, Intermolecular and Surface Forces, Academic Press, 2011.
[6] H. Bluhm, T. Inoue, M. Salmeron, Friction of ice measured using lateral force microscopy, Phys. Rev. B 61 (11) (2000) 7760.
[7] K.B. Jinesh, J.W.M. Frenken, Capillary condensation in atomic scale friction: how water acts like a glue, Phys. Rev. Lett. 96 (16) (2006) 166103.
[8] Y. Zhu, S. Granick, Viscosity of interfacial water, Phys. Rev. Lett. 87 (9) (2001) 096104.
[9] M.A. Henderson, The interaction of water with solid surfaces: fundamental aspects revisited, Surf. Sci. Rep. 46 (1–8) (2002) 1–308.
[10] V.V. Chaban, O.V. Prezhdo, Water boiling inside carbon nanotubes: toward efficient drug release, ACS Nano 5 (7) (2011) 5647–5655.
[11] S. Prakash, A. Piruska, E.N. Gatimu, P.W. Bohn, J.V. Sweedler, M.A. Shannon, Nanofluidics: systems and applications, IEEE Sensor. J. 8 (5) (2008) 441–450.

[12] J. Shim, C.H. Lui, T.Y. Ko, Y.J. Yu, P. Kim, T.F. Heinz, S. Ryu, Water-gated charge doping of graphene induced by mica substrates, Nano Lett. 12 (2) (2012) 648–654.
[13] Y. Wang, Z. Xu, Water intercalation for seamless, electrically insulating, and thermally transparent interfaces, ACS Appl. Mater. Interfaces 8 (3) (2016) 1970–1976.
[14] S. Granick, Motions and relaxations of confined liquids, Science 253 (5026) (1991) 1374–1379.
[15] M.-C. Bellissent-Funel, Status of experiments probing the dynamics of water in confinement, Eur. Phys. J. E 12 (1) (2003) 83–92.
[16] W.H. Zhao, L. Wang, J. Bai, L.F. Yuan, J. Yang, X.C. Zeng, Highly confined water: two-dimensional ice, amorphous ice, and clathrate hydrates, Acc. Chem. Res. 47 (8) (2014) 2505–2513.
[17] S. Cambré, B. Schoeters, S. Luyckx, E. Goovaerts, W. Wenseleers, Experimental observation of single-file water filling of thin single-wall carbon nanotubes down to chiral index (5,3), Phys. Rev. Lett. 104 (20) (2010) 207401.
[18] B. Mukherjee, P.K. Maiti, C. Dasgupta, A.K. Sood, Strong correlations and fickian water diffusion in narrow carbon nanotubes, J. Chem. Phys. 126 (12) (2007) 124704.
[19] N. Giovambattista, P.J. Rossky, P.G. Debenedetti, Phase transitions induced by nanoconfinement in liquid water, Phys. Rev. Lett. 102 (5) (2009) 050603.
[20] K. Koga, H. Tanaka, X.C. Zeng, First-order transition in confined water between high-density liquid and low-density amorphous phases, Nature 408 (6812) (2000) 564–567.
[21] G. Cicero, J.C. Grossman, E. Schwegler, F. Gygi, G. Galli, Water confined in nanotubes and between graphene sheets: a first principle study, J. Am. Chem. Soc. 130 (6) (2008) 1871–1878.
[22] H. Huang, Z. Song, N. Wei, L. Shi, Y. Mao, Y. Ying, L. Sun, Z. Xu, X. Peng, Ultrafast viscous water flow through nanostrand-channelled graphene oxide membranes, Nat. Commun. 4 (2013) 2979.
[23] N. Wei, X. Peng, Z. Xu, Breakdown of fast water transport in graphene oxides, Phys. Rev. E 89 (1) (2014) 012113.
[24] N. Wei, X. Peng, Z. Xu, Understanding water permeation in graphene oxide membranes, ACS Appl. Mater. Interfaces 6 (8) (2014) 5877–5883.
[25] M. Chen, W. Shen, X. Lu, R. Zhu, H. He, J. Zhu, Jumping diffusion of water intercalated in layered double hydroxides, J. Phys. Chem. C 120 (23) (2016) 12924–12931.
[26] Q. Li, Y. Xiao, X. Shi, S. Song, Rapid evaporation of water on graphene/graphene-oxide: a molecular dynamics study, Nanomaterials 7 (9) (2017) 265.
[27] L. Ruiz Pestana, L.E. Felberg, T. Head-Gordon, Coexistence of multilayered phases of confined water: the importance of flexible confining surfaces, ACS Nano 12 (1) (2018) 448–454.
[28] T. Kaneko, J. Bai, T. Akimoto, J.S. Francisco, K. Yasuoka, X.C. Zeng, Phase behaviors of deeply supercooled bilayer water unseen in bulk water, Proc. Nat. Acad. Sci. (2018) 201802342.
[29] T.A. Pascal, W.A. Goddard, Y. Jung, Entropy and the driving force for the filling of carbon nanotubes with water, Proc. Natl. Acad. Sci. 108 (29) (2011) 11794–11798.
[30] N. Naguib, H. Ye, Y. Gogotsi, A.G. Yazicioglu, C.M. Megaridis, M. Yoshimura, Observation of water confined in nanometer channels of closed carbon nanotubes, Nano Lett. 4 (11) (2004) 2237–2243.
[31] D. Takaiwa, I. Hatano, K. Koga, H. Tanaka, Phase diagram of water in carbon nanotubes, Proc. Natl. Acad. Sci. 105 (1) (2008) 39–43.
[32] G.A. Somorjai, H. Frei, J.Y. Park, Advancing the frontiers in nanocatalysis, biointerfaces, and renewable energy conversion by innovations of surface techniques, J. Am. Chem. Soc. 131 (46) (2009) 16589–16605.
[33] S. Han, M.Y. Choi, P. Kumar, H.E. Stanley, Phase transitions in confined water nanofilms, Nat. Phys. 6 (9) (2010) 685–689.
[34] J.A. Thomas, A.J.H. McGaughey, Water flow in carbon nanotubes: transition to subcontinuum transport, Phys. Rev. Lett. 102 (18) (2009) 184502.
[35] A. Hodgson, S. Haq, Water adsorption and the wetting of metal surfaces, Surf. Sci. Rep. 64 (9) (2009) 381–451.
[36] P.A. Thiel, T.E. Madey, The interaction of water with solid surfaces: fundamental aspects, Surf. Sci. Rep. 7 (6–8) (1987) 211–385.
[37] P.J. Feibelman, The first wetting layer on a solid, Phys. Today 63 (2) (2010) 34–39.
[38] P.V. Hobbs, Ice Physics, Oxford, 1974.
[39] G.C. Pimentel, A.L. McClellan, Hydrogen bonding, Annu. Rev. Phys. Chem. 22 (1) (1971) 347–385.
[40] R. Ludwig, Water: from clusters to the bulk, Angew. Chem. Int. Ed. 40 (10) (2001) 1808–1827.
[41] A. Verdaguer, G.M. Sacha, H. Bluhm, M. Salmeron, Molecular structure of water at interfaces: wetting at the nanometer scale, Chem. Rev. 106 (4) (2006) 1478–1510.
[42] S. Maier, M. Salmeron, How does water wet a surface? Acc. Chem. Res. 48 (10) (2015) 2783–2790.
[43] O. Björneholm, M.H. Hansen, A. Hodgson, L.-M. Liu, D.T. Limmer, A. Michaelides, P. Pedevilla, J. Rossmeisl, H. Shen, G. Tocci, E. Tyrode, M.-M. Walz, J. Werner, H. Bluhm, Water at interfaces, Chem. Rev. 116 (13) (2016) 7698–7726.
[44] S. Meng, E. Wang, S. Gao, Water adsorption on metal surfaces: a general picture from density functional theory studies, Phys. Rev. B 69 (19) (2004) 195404.
[45] H. Ogasawara, B. Brena, D. Nordlund, M. Nyberg, A. Pelmenschikov, L. Pettersson, A. Nilsson, Structure and bonding of water on Pt (111), Phys. Rev. Lett. 89 (27) (2002) 276102.
[46] J. Carrasco, A. Hodgson, A. Michaelides, A molecular perspective of water at metal interfaces, Nat. Mater. 11 (8) (2012) 667–674.
[47] D.L. Doering, T.E. Madey, The adsorption of water on clean and oxygen-dosed Ru(011), Surf. Sci. 123 (2) (1982) 305–337.
[48] P.J. Feibelman, Partial dissociation of water on Ru(0001), Science 295 (5552) (2002) 99–102.
[49] T. Kondo, S. Mae, H.S. Kato, M. Kawai, Morphological change of D_2O layers on Ru(0001) probed with He atom scattering, Surf. Sci. 600 (18) (2006) 3570–3574.
[50] A. Michaelides, A. Alavi, D.A. King, Different surface chemistries of water on Ru(0001): from monomer adsorption to partially dissociated bilayers, J. Am. Chem. Soc. 125 (9) (2003) 2746–2755.
[51] M. Gallagher, A. Omer, G.R. Darling, A. Hodgson, Order and disorder in the wetting layer on Ru(0001), Faraday Discuss 141 (2009) 231–249.
[52] S. Haq, C. Clay, G.R. Darling, G. Zimbitas, A. Hodgson, Growth of intact water ice on Ru(0001) between 140 and 160 K: Experiment and density-functional theory calculations, Phys. Rev. B 73 (11) (2006) 115414.
[53] L.E. Firment, G.A. Somorjai, Low-energy electron diffraction studies of molecular crystals: the surface structures of vapor-grown ice and naphthalene, J. Chem. Phys. 63 (2) (1975) 1037–1038.
[54] A. Glebov, A.P. Graham, A. Menzel, J.P. Toennies, Orientational ordering of two-dimensional ice on Pt(111), J. Chem. Phys. 106 (22) (1997) 9382–9385.
[55] S. Haq, J. Harnett, A. Hodgson, Growth of thin crystalline ice films on Pt(111), Surf. Sci. 505 (2002) 171–182.
[56] G. Zimbitas, S. Haq, A. Hodgson, The structure and crystallization of thin water films on Pt(111), J. Chem. Phys. 123 (17) (2005) 174701.
[57] M. Morgenstern, J. Müller, T. Michely, G. Comsa, The ice bilayer on Pt(111): nucleation, structure and melting, Z. Phys. Chem. 198 (1–2) (1997) 43–72.
[58] S. Standop, A. Redinger, M. Morgenstern, T. Michely, C. Busse, Molecular structure of the H_2O wetting layer on Pt(111), Phys. Rev. B 82 (16) (2010) 161412.
[59] P.J. Feibelman, G.A. Kimmel, R.S. Smith, N.G. Petrik, T. Zubkov, B.D. Kay, A unique vibrational signature of rotated water monolayers on Pt (111): predicted and observed, J. Chem. Phys. 134 (20) (2011) 204702.
[60] S. Nie, P.J. Feibelman, N.C. Bartelt, K. Thürmer, Pentagons and heptagons in the first water layer on Pt (111), Phys. Rev. Lett. 105 (2) (2010) 026102.
[61] P.J. Feibelman, N.C. Bartelt, S. Nie, K. Thürmer, Interpretation of high-resolution images of the best-bound wetting layers on Pt (111), J. Chem. Phys. 133 (15) (2010) 154703.
[62] J. Carrasco, A. Michaelides, M. Forster, S. Haq, R. Raval, A. Hodgson, A one-dimensional ice structure built from pentagons, Nat. Mater. 8 (5) (2009) 427–431.
[63] J. Carrasco, B. Santra, J. Klimeš, A. Michaelides, To wet or not to wet? dispersion forces tip the balance for water ice on metals, Phys. Rev. Lett. 106 (2) (2011) 026101.
[64] G.A. Kimmel, J. Matthiesen, M. Baer, C.J. Mundy, N.G. Petrik, R.S. Smith, Z. Dohnálek, B.D. Kay, No confinement needed: observation of a metastable hydrophobic wetting two-layer ice on graphene, J. Am. Chem. Soc. 131 (35) (2009) 12838–12844.
[65] D. Stacchiola, J.B. Park, P. Liu, S. Ma, F. Yang, D.E. Starr, E. Muller, P. Sutter, J. Hrbek, Water nucleation on gold: existence of a unique double bilayer, J. Phys. Chem. C 113 (34) (2009) 15102–15105.
[66] G.A. Kimmel, N.G. Petrik, Z. Dohnálek, B.D. Kay, Crystalline ice growth on Pt (111): observation of a hydrophobic water monolayer, Phys. Rev. Lett. 95 (16) (2005) 166102.
[67] S. Haq, A. Hodgson, Multilayer growth and wetting of Ru (0001), J. Phys. Chem. C 111 (16) (2007) 5946–5953.
[68] G. Zimbitas, M.E. Gallagher, G.R. Darling, A. Hodgson, Wetting of mixed OH/H_2O layers on Pt (111), J. Chem. Phys. 128 (7) (2008) 074701.
[69] G.A. Kimmel, T. Zubkov, R.S. Smith, N.G. Petrik, B.D. Kay, Turning things downside up: adsorbate induced water flipping on Pt(111), J. Chem. Phys. 141 (18) (2014) 18C515.
[70] D. Beaglehole, E.Z. Radlinska, B.W. Ninham, H.K. Christenson, Inadequacy of lifshitz theory for thin liquid films, Phys. Rev. Lett. 66 (16) (1991) 2084.
[71] P.B. Miranda, L. Xu, Y.R. Shen, M. Salmeron, Icelike water monolayer adsorbed on mica at room temperature, Phys. Rev. Lett. 81 (26) (1998) 5876.
[72] W. Cantrell, G.E. Ewing, Thin film water on muscovite mica, J. Phys. Chem. B 105 (23) (2001) 5434–5439.
[73] G.E. Ewing, Ambient thin film water on insulator surfaces, Chem. Rev. 106 (4) (2006) 1511–1526.
[74] R.D. Piner, C.A. Mirkin, Effect of water on lateral force microscopy in air, Langmuir 13 (26) (1997) 6864–6868.
[75] K. Xu, P. Cao, J.R. Heath, Graphene visualizes the first water adlayers on mica at ambient conditions, Science 329 (5996) (2010) 1188–1191.
[76] C. Melios, C.E. Giusca, V. Panchal, O. Kazakova, Water on graphene: review of recent progress, 2D Mater. 5 (2) (2018) 022001.
[77] G.R. Edwards, L.F. Evans, A.F. Zippear, Two-dimensional phase changes in water adsorbed on ice-nucleating substrates, Trans. Faraday Soc. 66 (1970) 220–234.
[78] J.L. Caslavsky, K. Vedam, Epitaxial growth of ice crystals on the muscovite cleavage plane and their relation to partial dislocations, J. Appl. Phys. 42 (2) (1971) 516–520.
[79] Y. Leng, P.T. Cummings, Hydration structure of water confined between mica surfaces, J. Chem. Phys. 124 (7) (2006) 074711.

[80] D. Beaglehole, H.K. Christenson, Vapor adsorption on mica and silicon: entropy effects, layering, and surface forces, J. Phys. Chem. 96 (8) (1992) 3395–3403.
[81] J. Hu, D.F. Ogletree, M. Salmeron, The structure of molecularly thin films of water on mica in humid environments, Surf. Sci. 344 (3) (1995) 221–236.
[82] J. Hu, X.D. Xiao, D.F. Ogletree, M. Salmeron, Imaging the condensation and evaporation of molecularly thin films of water with nanometer resolution, Science 268 (5208) (1995) 267–269.
[83] L. Xu, A. Lio, J. Hu, D.F. Ogletree, M. Salmeron, Wetting and capillary phenomena of water on mica, J. Phys. Chem. B 102 (3) (1998) 540–548.
[84] M. Odelius, M. Bernasconi, M. Parrinello, Two dimensional ice adsorbed on mica surface, Phys. Rev. Lett. 78 (14) (1997) 2855.
[85] P.J. Feibelman, K+-hydration in a low-energy two-dimensional wetting layer on the basal surface of muscovite, J. Chem. Phys. 139 (7) (2013) 074705.
[86] D. Chandler, Interfaces and the driving force of hydrophobic assembly, Nature 437 (7059) (2005) 640.
[87] K. Suzuki, N. Oyabu, K. Kobayashi, K. Matsushige, H. Yamada, Atomic-resolution imaging of graphite–water interface by frequency modulation atomic force microscopy, Appl. Phys. Express 4 (12) (2011) 125102.
[88] T. Gowthami, N. Kurra, G. Raina, Interaction and dynamics of ambient water adlayers on graphite probed using AFM voltage nanolithography and electrostatic force microscopy, Nanotechnology 25 (15) (2014) 155304.
[89] Y. Zheng, C. Su, J. Lu, K.P. Loh, Room-temperature ice growth on graphite seeded by nano-graphene oxide, Angew. Chem. Int. Ed. 52 (33) (2013) 8708–8712.
[90] A. Gil, J. Colchero, M. Luna, J. Gómez-Herrero, A.M. Baró, Adsorption of water on solid surfaces studied by scanning force microscopy, Langmuir 16 (11) (2000) 5086–5092.
[91] M. Luna, J. Colchero, A.M. Baró, Study of water droplets and films on graphite by noncontact scanning force microscopy, J. Phys. Chem. B 103 (44) (1999) 9576–9581.
[92] D.-S. Yang, A.H. Zewail, Ordered water structure at hydrophobic graphite interfaces observed by 4D, ultrafast electron crystallography, Proc. Natl. Acad. Sci. 106 (11) (2009) 4122–4126.
[93] O. Teschke, Imaging ice-like structures formed on HOPG at room temperature, Langmuir 26 (22) (2010) 16986–16990.
[94] K.S. Novoselov, A.K. Geim, S.V. Morozov, D. Jiang, Y. Zhang, S.V. Dubonos, I.V. Grigorieva, A.A. Firsov, Electric field in atomically thin carbon films, Science 306 (5696) (2004) 666–669.
[95] K.S. Novoselov, A.K. Geim, S.V. Morozov, D. Jiang, M.I. Katsnelson, I.V. Grigorieva, S.V. Dubonos, A.A. Firsov, Two-dimensional gas of massless Dirac fermions in graphene, Nature 438 (7065) (2005) 197–200.
[96] K.S. Novoselov, D. Jiang, F. Schedin, T.J. Booth, V.V. Khotkevich, S.V. Morozov, A.K. Geim, Two-dimensional atomic crystals, Proc. Natl. Acad. Sci. 102 (30) (2005) 10451–10453.
[97] A.H.C. Neto, F. Guinea, N.M.R. Peres, K.S. Novoselov, A.K. Geim, The electronic properties of graphene, Rev. Mod. Phys. 81 (1) (2009) 109.
[98] Y. Zhang, Y.-W. Tan, H.L. Stormer, P. Kim, Experimental observation of the quantum hall effect and berry's phase in graphene, Nature 438 (7065) (2005) 201–204.
[99] A.K. Geim, K.S. Novoselov, The rise of graphene, Nat. Mater. 6 (3) (2007) 183–191.
[100] C. Lee, X. Wei, J.W. Kysar, J. Hone, Measurement of the elastic properties and intrinsic strength of monolayer graphene, Science 321 (5887) (2008) 385–388.
[101] A.A. Balandin, S. Ghosh, W. Bao, I. Calizo, D. Teweldebrhan, F. Miao, C.N. Lau, Superior thermal conductivity of single-layer graphene, Nano Lett. 8 (3) (2008) 902–907.
[102] J.S. Bunch, S.S. Verbridge, J.S. Alden, A.M. Van Der Zande, J.M. Parpia, H.G. Craighead, P.L. McEuen, Impermeable atomic membranes from graphene sheets, Nano Lett. 8 (8) (2008) 2458–2462.
[103] Q. Li, J. Song, F. Besenbacher, M. Dong, Two-dimensional material confined water, Acc. Chem. Res. 48 (1) (2015) 119–127.
[104] E. Pop, V. Varshney, A.K. Roy, Thermal properties of graphene: fundamentals and applications, MRS Bull. 37 (12) (2012) 1273–1281.
[105] N. Severin, P. Lange, I.M. Sokolov, J.P. Rabe, Reversible dewetting of a molecularly thin fluid water film in a soft graphene-mica slit pore, Nano Lett. 12 (2) (2012) 774–779.
[106] P. Bampoulis, M.H. Siekman, E.S. Kooij, D. Lohse, H.J.W. Zandvliet, B. Poelsema, Latent heat induced rotation limited aggregation in 2D ice nanocrystals, J. Chem. Phys. 143 (3) (2015) 034702.
[107] J. Song, Q. Li, X. Wang, J. Li, S. Zhang, J. Kjems, F. Besenbacher, M. Dong, Evidence of Stranski-Krastanov growth at the initial stage of atmospheric water condensation, Nat. Commun. 5 (4837) (2013) 4837.
[108] K.S. Novoselov, A.K. Geim, S.V. Morozov, D. Jiang, Y. Zhang, S.V. Dubonos, I.V. Grigorieva, A.A. Firsov, Electric field effect in atomically thin carbon films, Science 306 (5696) (2004) 666–669.
[109] B. Rezania, M. Dorn, N. Severin, J. Rabe, Influence of graphene exfoliation on the properties of water-containing adlayers visualized by graphenes and scanning force microscopy, J. Colloid Interface Sci. 407 (2013) 500–504.
[110] M. Dorn, P. Lange, A. Chekushin, N. Severin, J.P. Rabe, High contrast optical detection of single graphenes on optically transparent substrates, J. Appl. Phys. 108 (10) (2010) 106101.
[111] D. Graf, F. Molitor, K. Ensslin, C. Stampfer, A. Jungen, C. Hierold, L. Wirtz, Spatially resolved Raman spectroscopy of single-and few-layer graphene, Nano Lett. 7 (2) (2007) 238–242.
[112] A.C. Ferrari, D.M. Basko, Raman spectroscopy as a versatile tool for studying the properties of graphene, Nat. Nanotechnol. 8 (2013) 235.
[113] H. Lin, A. Schilo, A.R. Kamoka, N. Severin, I.M. Sokolov, J.P. Rabe, Insight into the wetting of a graphene-mica slit pore with a monolayer of water, Phys. Rev. B 95 (19) (2017) 195414.
[114] C.H. Lui, L. Liu, K.F. Mak, G.W. Flynn, T.F. Heinz, Ultraflat graphene, Nature 462 (7271) (2009) 339–341.
[115] M. Breusing, S. Kuehn, T. Winzer, E. Malić, F. Milde, N. Severin, J.P. Rabe, C. Ropers, A. Knorr, T. Elsaesser, Ultrafast nonequilibrium carrier dynamics in a single graphene layer, Phys. Rev. B 83 (15) (2011) 153410.
[116] A. Castellanos-Gomez, M. Wojtaszek, N. Tombros, N. Agraït, B.J. van Wees, G. Rubio-Bollinger, Atomically thin mica flakes and their application as ultrathin insulating substrates for graphene, Small 7 (17) (2011) 2491–2497.
[117] Z. Ben Aziza, Q. Zhang, D. Baillargeat, Graphene/mica based ammonia gas sensors, Appl. Phys. Lett. 105 (25) (2014) 254102.
[118] R. Garcıa, R. Perez, Dynamic atomic force microscopy methods, Surf. Sci. Rep. 47 (6) (2002) 197–301.
[119] M. Temmen, O. Ochedowski, M. Schleberger, M. Reichling, T.R.J. Bollmann, Hydration layers trapped between graphene and a hydrophilic substrate, N. J. Phys. 16 (5) (2014) 053039.
[120] H. Li, X.C. Zeng, Two dimensional epitaxial water adlayer on mica with graphene coating: an ab initio molecular dynamics study, J. Chem. Theor. Comput. 8 (9) (2012) 3034–3043.
[121] J.S. Kim, J.S. Choi, M.J. Lee, B.H. Park, D. Bukhvalov, Y.W. Son, D. Yoon, H. Cheong, J.N. Yun, Y. Jung, J.Y. Park, M. Salmeron, Between scylla and charybdis: hydrophobic graphene-guided water diffusion on hydrophilic substrates, Sci. Rep. 3 (2013) 2309.
[122] K.T. He, J.D. Wood, G.P. Doidge, E. Pop, J.W. Lyding, Scanning tunneling microscopy study and nanomanipulation of graphene-coated water on mica, Nano Lett. 12 (6) (2012) 2665–2672.
[123] J.A. Venables, Introduction to Surface and Thin Film Processes, Cambridge University Press, Cambridge, 2000.
[124] A.N. Rudenko, F.J. Keil, M.I. Katsnelson, A.I. Lichtenstein, Graphene adhesion on mica: role of surface morphology, Phys. Rev. B 83 (4) (2011) 045409.
[125] P. Bampoulis, K. Sotthewes, M.H. Siekman, H.J.W. Zandvliet, B. Poelsema, Graphene visualizes the ion distribution on air-cleaved mica, Sci. Rep. 7 (2017) 43451.
[126] K. Sotthewes, P. Bampoulis, H.J.W. Zandvliet, D. Lohse, B. Poelsema, Pressure-induced melting of confined ice, ACS Nano 11 (12) (2017) 12723–12731.
[127] P. Bampoulis, D. Lohse, H.J.W. Zandvliet, B. Poelsema, Coarsening dynamics of ice fractals intercalated between graphene and mica, Appl. Phys. Lett. 108 (2016) 011601.
[128] P. Koskinen, O.O. Kit, Approximate modeling of spherical membranes, Phys. Rev. B 82 (23) (2010) 235420.
[129] O. Ochedowski, B.K. Bussmann, M. Schleberger, Graphene on mica - intercalated water trapped for life, Sci. Rep. 4 (2014) 6003.
[130] M. Faraday, Note on regelation, Proc. Roy. Soc. Lond. 10 (1859) 440.
[131] J. Thomson, Note on professor Faraday's recent experiments on regelation, Proc. Roy. Soc. Lond. 11 (1860) 198.
[132] C.Q. Sun, X. Zhang, W. Zheng, The hidden force opposing ice compression, Chem. Sci. 3 (5) (2012) 1455–1460.
[133] X. Zhang, Y. Huang, P. Sun, X. Liu, Z. Ma, Y. Zhou, J. Zhou, W. Zheng, C.Q. Sun, Ice regelation: hydrogen-bond extraordinary recoverability and water quasisolid-phase-boundary dispersivity, Sci. Rep. 5 (2015) 13655.
[134] X. Zhang, Y. Huang, Z. Ma, Y. Zhou, W. Zheng, J. Zhou, C.Q. Sun, A common supersolid skin covering both water and ice, Phys. Chem. Chem. Phys. 16 (42) (2014) 22987–22994.
[135] Q. Zeng, T. Yan, K. Wang, Y. Gong, Y. Zhou, Y. Huang, C.Q. Sun, B. Zou, Compression icing of room-temperature NaX solutions (X= F, Cl, Br, I), Phys. Chem. Chem. Phys. 18 (20) (2016) 14046–14054.
[136] Q. Zeng, C. Yao, K. Wang, C.Q. Sun, B. Zou, Room-temperature NaI/H_2O compression icing: solute–solute interactions, Phys. Chem. Chem. Phys. 19 (39) (2017) 26645–26650.
[137] C.Q. Sun, J. Chen, Y. Gong, X. Zhang, Y. Huang, H. Li, Br and LiOH solvation bonding dynamics: molecular nonbond interactions and solute extraordinary capabilities, J. Phys. Chem. B 122 (3) (2018) 1228–1238.
[138] I.V. Markov, Crystal Growth for Beginners: Fundamentals of Nucleation, Crystal Growth and Epitaxy, World Scientific, 2016.
[139] H.K. Christenson, N.H. Thomson, The nature of the air-cleaved mica surface, Surf. Sci. Rep. 71 (2) (2016) 367–390.
[140] D. G. Purdie, N. M. Pugno, T. Taniguchi, K. Watanabe, A. C. Ferrari, A. Lombardo, Cleaning Interfaces in Layered Materials Heterostructures, arXiv preprint arXiv: 1803.00912.
[141] N. Severin, I.M. Sokolov, J.P. Rabe, Dynamics of ethanol and water mixtures observed in a self-adjusting molecularly thin slit pore, Langmuir 30 (12) (2014) 3455–3459.
[142] N. Severin, J. Gienger, V. Scenev, P. Lange, I.M. Sokolov, J.P. Rabe, Nanophase separation in monomolecularly thin water-ethanol films controlled by graphene, Nano Lett. 15 (2) (2015) 1171–1176.
[143] P. Bampoulis, J.P. Witteveen, E.S. Kooij, D. Lohse, B. Poelsema, H.J.W. Zandvliet, Structure and dynamics of confined alcohol-water mixtures, ACS Nano 10 (7) (2016) 6762–6768.
[144] X. Ren, C. Wang, B. Zhou, H. Fang, J. Hu, R. Zhou, Ethanol promotes dewetting transition at low concentrations, Soft Matter 9 (18) (2013) 4655–4660.
[145] M. Zhao, X. Yang, Segregation structures and miscellaneous diffusions for ethanol/water mixtures in graphene-based nanoscale pores, J. Phys. Chem. C 119 (37) (2015) 21664–21673.

[146] Q. Gao, Y. Zhu, Y. Ruan, Y. Zhang, W. Zhu, X. Lu, L. Lu, Effect of adsorbed alcohol layers on the behavior of water molecules confined in a graphene nanoslit: a molecular dynamics study, Langmuir 33 (42) (2017) 11467–11474.

[147] D.D. Borges, C.F. Woellner, P.A.S. Autreto, D.S. Galvao, Insights on the mechanism of water-alcohol separation in multilayer graphene oxide membranes: entropic versus enthalpic factors, Carbon 127 (2018) 280–286.

[148] M. Ishigami, J.H. Chen, W.G. Cullen, M.S. Fuhrer, E.D. Williams, Atomic structure of graphene on SiO_2, Nano Lett. 7 (6) (2007) 1643–1648.

[149] E. Stolyarova, K.T. Rim, S. Ryu, J. Maultzsch, P. Kim, L.E. Brus, T.F. Heinz, M.S. Hybertsen, G.W. Flynn, High-resolution scanning tunneling microscopy imaging of mesoscopic graphene sheets on an insulating surface, Proc. Natl. Acad. Sci. 104 (22) (2007) 9209–9212.

[150] W.G. Cullen, M. Yamamoto, K.M. Burson, J.H. Chen, C. Jang, L. Li, M.S. Fuhrer, E.D. Williams, High-fidelity conformation of graphene to SiO_2 topographic features, Phys. Rev. Lett. 105 (21) (2010) 215504.

[151] S.V. Morozov, K.S. Novoselov, M.I. Katsnelson, F. Schedin, L.A. Ponomarenko, D. Jiang, A.K. Geim, Strong suppression of weak localization in graphene, Phys. Rev. Lett. 97 (1) (2006) 016801.

[152] F. Guinea, M.I. Katsnelson, A.K. Geim, Energy gaps and a zero-field quantum hall effect in graphene by strain engineering, Nat. Phys. 6 (1) (2010) 30.

[153] N. Levy, S.A. Burke, K.L. Meaker, M. Panlasigui, A. Zettl, F. Guinea, A.H.C. Neto, M.F. Crommie, Strain-induced pseudo–magnetic fields greater than 300 tesla in graphene nanobubbles, Science 329 (5991) (2010) 544–547.

[154] Y.-J. Kang, J. Kang, K.J. Chang, Electronic structure of graphene and doping effect on SiO_2, Phys. Rev. B 78 (11) (2008) 115404.

[155] Y. Shi, X. Dong, P. Chen, J. Wang, L.-J. Li, Effective doping of single-layer graphene from underlying SiO_2 substrates, Phys. Rev. B 79 (11) (2009) 115402.

[156] S. Ryu, L. Liu, S. Berciaud, Y.-J. Yu, H. Liu, P. Kim, G.W. Flynn, L.E. Brus, Atmospheric oxygen binding and hole doping in deformed graphene on a SiO_2 substrate, Nano Lett. 10 (12) (2010) 4944–4951.

[157] R.H. Miwa, T.M. Schmidt, W.L. Scopel, A. Fazzio, Doping of graphene adsorbed on the a-SiO_2 surface, Appl. Phys. Lett. 99 (16) (2011) 163108.

[158] M.J. Lee, J.S. Choi, J.S. Kim, I.S. Byun, D.H. Lee, S. Ryu, C. Lee, B.H. Park, Characteristics and effects of diffused water between graphene and a SiO_2 substrate, Nano Res. 5 (10) (2012) 710–717.

[159] M. Chhikara, E. Pavlica, A. Matković, R. Gajić, G. Bratina, Effect of water layer at the SiO_2/graphene interface on pentacene morphology, Langmuir 30 (39) (2014) 11681–11688.

[160] D. Lee, G. Ahn, S. Ryu, Two-dimensional water diffusion at a graphene–silica interface, J. Am. Chem. Soc. 136 (18) (2014) 6634–6642.

[161] A. Verdaguer, J.J. Segura, L. López-Mir, G. Sauthier, J. Fraxedas, Communication: growing room temperature ice with graphene, J. Chem. Phys. 138 (12) (2013) 121101.

[162] X. Feng, S. Maier, M. Salmeron, Water splits epitaxial graphene and intercalates, J. Am. Chem. Soc. 134 (12) (2012) 5662–5668.

[163] Y. Yao, Q. Fu, Y.Y. Zhang, X. Weng, H. Li, M. Chen, L. Jin, A. Dong, R. Mu, P. Jiang, L. Liu, H. Bluhm, Z. Liu, S.B. Zhang, X. Bao, Graphene cover-promoted metal-catalyzed reactions, Proc. Natl. Acad. Sci. 111 (48) (2014) 17023–17028.

[164] D. Deng, K.S. Novoselov, Q. Fu, N. Zheng, Z. Tian, X. Bao, Catalysis with two-dimensional materials and their heterostructures, Nat. Nanotechnol. 11 (3) (2016) 218.

[165] D. Jiao, D. Dehui, B. Xinhe, Robust catalysis on 2D materials encapsulating metals: concept, application, and perspective, Adv. Mater. 29 (43) (2017) 1606967.

[166] L. Ferrighi, D. Perilli, D. Selli, C. Di Valentin, Water at the interface between defective graphene and Cu or Pt (111) surfaces, ACS Appl. Mater. Interfaces 9 (35) (2017) 29932–29941.

[167] T. Yoon, J.H. Mun, B.J. Cho, T.-S. Kim, Penetration and lateral diffusion characteristics of polycrystalline graphene barriers, Nanoscale 6 (1) (2014) 151–156.

[168] H. Komurasaki, T. Tsukamoto, K. Yamazaki, T. Ogino, Layered structures of interfacial water and their effects on Raman spectra in graphene-on-sapphire systems, J. Phys. Chem. C 116 (18) (2012) 10084–10089.

[169] M. Datteo, H. Liu, C. Di Valentin, Water on graphene-coated TiO_2: role of atomic vacancies, ACS Appl. Mater. Interfaces 10 (6) (2018) 5793–5804.

[170] E.J. Olson, R. Ma, T. Sun, M.A. Ebrish, N. Haratipour, K. Min, N.R. Aluru, S.J. Koester, Capacitive sensing of intercalated H_2O molecules using graphene, ACS Appl. Mater. Interfaces 7 (46) (2015) 25804–25812.

[171] T. Iiyama, K. Nishikawa, T. Otowa, K. Kaneko, An ordered water molecular assembly structure in a slit-shaped carbon nanospace, J. Phys. Chem. 99 (25) (1995) 10075–10076.

[172] A. Kalra, S. Garde, G. Hummer, Osmotic water transport through carbon nanotube membranes, Proc. Natl. Acad. Sci. 100 (18) (2003) 10175–10180.

[173] N. Choudhury, B.M. Pettitt, Dynamics of water trapped between hydrophobic solutes, J. Phys. Chem. B 109 (13) (2005) 6422–6429.

[174] N. Desbiens, I. Demachy, A.H. Fuchs, H. Kirsch-Rodeschini, M. Soulard, J. Patarin, Water condensation in hydrophobic nanopores, Angew. Chem. Int. Ed. 44 (33) (2005) 5310–5313.

[175] P. Hirunsit, P.B. Balbuena, Effects of confinement on water structure and dynamics: a molecular simulation study, J. Phys. Chem. C 111 (4) (2007) 1709–1715.

[176] S. Chakraborty, H. Kumar, C. Dasgupta, P.K. Maiti, Confined water: structure, dynamics, and thermodynamics, Acc. Chem. Res. 50 (9) (2017) 2139–2146.

[177] H. Yoshida, V. Kaiser, B. Rotenberg, L. Bocquet, Dripplons as localized and superfast ripples of water confined between graphene sheets, Nat. Commun. 9 (1) (2018) 1496.

[178] V. Eroshenko, R.-C. Regis, M. Soulard, J. Patarin, Energetics: a new field of applications for hydrophobic zeolites, J. Am. Chem. Soc. 123 (33) (2001) 8129–8130.

[179] G. Algara-Siller, O. Lehtinen, F.C. Wang, R.R. Nair, U. Kaiser, H.A. Wu, A.K. Geim, I.V. Grigorieva, Square ice in graphene nanocapillaries, Nature 519 (7544) (2015) 443–445.

[180] Y. Maniwa, H. Kataura, M. Abe, S. Suzuki, Y. Achiba, H. Kira, K. Matsuda, Phase transition in confined water inside carbon nanotubes, J. Phys. Soc. Jpn. 71 (12) (2002) 2863–2866.

[181] Y. Maniwa, H. Kataura, M. Abe, A. Udaka, S. Suzuki, Y. Achiba, H. Kira, K. Matsuda, H. Kadowaki, Y. Okabe, Ordered water inside carbon nanotubes: formation of pentagonal to octagonal ice-nanotubes, Chem. Phys. Lett. 401 (4–6) (2005) 534–538.

[182] K. Koga, G.T. Gao, H. Tanaka, X.C. Zeng, Formation of ordered ice nanotubes inside carbon nanotubes, Nature 412 (6849) (2001) 802.

[183] O. Byl, J.-C. Liu, Y. Wang, W.-L. Yim, J.K. Johnson, J.T. Yates, Unusual hydrogen bonding in water-filled carbon nanotubes, J. Am. Chem. Soc. 128 (37) (2006) 12090–12097.

[184] S. Ghosh, K.V. Ramanathan, A.K. Sood, Water at nanoscale confined in single-walled carbon nanotubes studied by NMR, EPL 65 (5) (2004) 678.

[185] A.I. Kolesnikov, J.-M. Zanotti, C.-K. Loong, P. Thiyagarajan, A.P. Moravsky, R.O. Loutfy, C.J. Burnham, Anomalously soft dynamics of water in a nanotube: a revelation of nanoscale confinement, Phys. Rev. Lett. 93 (3) (2004) 035503.

[186] N. Choudhury, Dynamics of water at the nanoscale hydrophobic confinement, J. Chem. Phys. 132 (6) (2010) 064505.

[187] V. Bianco, G. Franzese, Critical behavior of a water monolayer under hydrophobic confinement, Sci. Rep. 4 (2014) 4440.

[188] R. Zangi, A.E. Mark, Monolayer ice, Phys. Rev. Lett. 91 (2) (2003) 025502.

[189] J. Bai, X.C. Zeng, Polymorphism and polyamorphism in bilayer water confined to slit nanopore under high pressure, Proc. Natl. Acad. Sci. 109 (52) (2012) 21240–21245.

[190] W.-H. Zhao, J. Bai, L.-F. Yuan, J. Yang, X.C. Zeng, Ferroelectric hexagonal and rhombic monolayer ice phases, Chem. Sci. 5 (5) (2014) 1757–1764.

[191] J. Chen, G. Schusteritsch, C.J. Pickard, C.G. Salzmann, A. Michaelides, Two dimensional ice from first principles: structures and phase transitions, Phys. Rev. Lett. 116 (2) (2016) 025501.

[192] K. Kwac, I. Kim, T.A. Pascal, W.A. Goddard, H.G. Park, Y. Jung, Multilayer two-dimensional water structure confined in MoS_2, J. Phys. Chem. C 121 (29) (2017) 16021–16028.

[193] N. Giovambattista, P.J. Rossky, P.G. Debenedetti, Effect of temperature on the structure and phase behavior of water confined by hydrophobic, hydrophilic, and heterogeneous surfaces, J. Phys. Chem. B 113 (42) (2009) 13723–13734.

[194] Y. Zhang, K.-H. Liu, M. Lagi, D. Liu, K.C. Littrell, C.-Y. Mou, S.-H. Chen, Absence of the density minimum of supercooled water in hydrophobic confinement, J. Phys. Chem. B 113 (15) (2009) 5007–5010.

[195] K.B. Jinesh, J.W.M. Frenken, Experimental evidence for ice formation at room temperature, Phys. Rev. Lett. 101 (3) (2008) 036101.

[196] P. Cao, K. Xu, J.O. Varghese, J.R. Heath, The microscopic structure of adsorbed water on hydrophobic surfaces under ambient conditions, Nano Lett. 11 (12) (2011) 5581–5586.

[197] P. Cao, J.O. Varghese, K. Xu, J.R. Heath, Visualizing local doping effects of individual water clusters on gold(111)-supported graphene, Nano Lett. 12 (3) (2012) 1459–1463.

[198] T.O. Wehling, A.I. Lichtenstein, M.I. Katsnelson, First-principles studies of water adsorption on graphene: the role of the substrate, Appl. Phys. Lett. 93 (20) (2008) 202110.

[199] J. Rafiee, X. Mi, H. Gullapalli, A.V. Thomas, F. Yavari, Y. Shi, P.M. Ajayan, N.A. Koratkar, Wetting transparency of graphene, Nat. Mater. 11 (3) (2012) 217.

[200] C.-J. Shih, M.S. Strano, D. Blankschtein, Wetting translucency of graphene, Nat. Mater. 12 (10) (2013) 866.

[201] Z. Li, Y. Wang, A. Kozbial, G. Shenoy, F. Zhou, R. McGinley, P. Ireland, B. Morganstein, A. Kunkel, S.P. Surwade, L. Li, H. Liu, Effect of airborne contaminants on the wettability of supported graphene and graphite, Nat. Mater. 12 (10) (2013) 925.

[202] H.W. Kim, H.W. Yoon, S.-M. Yoon, B.M. Yoo, B.K. Ahn, Y.H. Cho, H.J. Shin, H. Yang, U. Paik, S. Kwon, J.-Y. Choi, H.B. Park, Selective gas transport through few-layered graphene and graphene oxide membranes, Science 342 (6154) (2013) 91–95.

[203] Z. Li, A. Kozbial, N. Nioradze, D. Parobek, G.J. Shenoy, M. Salim, S. Amemiya, L. Li, H. Liu, Water protects graphitic surface from airborne hydrocarbon contamination, ACS Nano 10 (1) (2015) 349–359.

[204] A.A. Chialvo, L. Vlcek, P.T. Cummings, Surface corrugation effects on the water–graphene interfacial and confinement behavior, J. Phys. Chem. C 117 (45) (2013) 23875–23886.

[205] J.C. Meyer, C.O. Girit, M.F. Crommie, A. Zettl, Imaging and dynamics of light atoms and molecules on graphene, Nature 454 (7202) (2008) 319.

[206] J.M. Yuk, J. Park, P. Ercius, K. Kim, D.J. Hellebusch, M.F. Crommie, J.Y. Lee, A. Zettl, A.P. Alivisatos, High-resolution EM of colloidal nanocrystal growth using graphene liquid cells, Science 336 (6077) (2012) 61–64.

[207] G. Algara-Siller, S. Kurasch, M. Sedighi, O. Lehtinen, U. Kaiser, The pristine atomic structure of MoS_2 monolayer protected from electron radiation damage by graphene, Appl. Phys. Lett. 103 (20) (2013) 203107.

[208] K. Kobayashi, M. Koshino, K. Suenaga, Atomically resolved images of I_h ice single crystals in the solid phase, Phys. Rev. Lett. 106 (20) (2011) 206101.

[209] W. Zhou, K. Yin, C. Wang, Y. Zhang, T. Xu, A. Borisevich, L. Sun, J.C. Idrobo, M.F. Chisholm, S.T. Pantelides, R.F. Klie, A.R. Lupini, The observation of square ice in graphene questioned, Nature 528 (7583) (2015) E1.
[210] G. Algara-Siller, O. Lehtinen, U. Kaiser, Algara-Siller et al. reply, Nature 528 (7583) (2015) E3.
[211] F.C. Wang, H.A. Wu, A.K. Geim, Wang et al. reply, Nature 528 (7583) (2015) E3.
[212] Y. Zhu, F. Wang, J. Bai, X.C. Zeng, H. Wu, Compression limit of two-dimensional water constrained in graphene nanocapillaries, ACS Nano 9 (12) (2015) 12197–12204.
[213] F. Corsetti, P. Matthews, E. Artacho, Structural and configurational properties of nanoconfined monolayer ice from first principles, Sci. Rep. 6 (2016) 18651.
[214] J. Chen, A. Zen, J.G. Brandenburg, D. Alfè, A. Michaelides, Evidence for stable square ice from quantum Monte Carlo, Phys. Rev. B 94 (22) (2016) 220102.
[215] Y. Zhu, F. Wang, J. Bai, X.C. Zeng, H. Wu, AB-stacked square-like bilayer ice in graphene nanocapillaries, Phys. Chem. Chem. Phys. 18 (32) (2016) 22039–22046.
[216] Y. Zhu, F. Wang, J. Bai, X.C. Zeng, H. Wu, Formation of trilayer ices in graphene nanocapillaries under high lateral pressure, J. Phys. Chem. C 120 (15) (2016) 8109–8115.
[217] Y. Zhu, F. Wang, H. Wu, Superheating of monolayer ice in graphene nanocapillaries, J. Chem. Phys. 146 (13) (2017) 134703.
[218] S. Jiao, C. Duan, Z. Xu, Structures and thermodynamics of water encapsulated by graphene, Sci. Rep. 7 (1) (2017) 2646.
[219] Y. Zhu, F. Wang, H. Wu, Structural and dynamic characteristics in monolayer square ice, J. Chem. Phys. 147 (4) (2017) 044706.
[220] Z. Gao, N. Giovambattista, O. Sahin, Phase diagram of water confined by graphene, Sci. Rep. 8 (1) (2018) 6228.
[221] M.S.F. Mario, M. Neek-Amal, F.M. Peeters, AA-stacked bilayer square ice between graphene layers, Phys. Rev. B 92 (24) (2015) 245428.
[222] M.S. Fernández, F.M. Peeters, M. Neek-Amal, Electric-field-induced structural changes in water confined between two graphene layers, Phys. Rev. B 94 (4) (2016) 045436.
[223] V. Satarifard, M. Mousaei, F. Hadadi, J. Dix, M.S. Fernandez, P. Carbone, J. Beheshtian, F.M. Peeters, M. Neek-Amal, Reversible structural transition in nanoconfined ice, Phys. Rev. B 95 (6) (2017) 064105.
[224] W. Zhu, Y. Zhu, L. Wang, Q. Zhu, W.-H. Zhao, C. Zhu, J. Bai, J. Yang, L.-F. Yuan, H. Wu, X.C. Zeng, Water confined in nanocapillaries: two-dimensional bilayer squarelike ice and associated solid-liquid-solid transition, J. Phys. Chem. C 122 (12) (2018) 6704–6712.
[225] K. Koga, X.C. Zeng, H. Tanaka, Freezing of confined water: a bilayer ice phase in hydrophobic nanopores, Phys. Rev. Lett. 79 (26) (1997) 5262–5265.
[226] P. Bampoulis, V.J. Teernstra, D. Lohse, H.J.W. Zandvliet, B. Poelsema, Hydrophobic ice confined between graphene and MoS_2, J. Phys. Chem. C 120 (47) (2016) 27079–27084.
[227] S. Sharma, P.G. Debenedetti, Evaporation rate of water in hydrophobic confinement, Proc. Natl. Acad. Sci. 109 (12) (2012) 4365–4370.
[228] P. Först, F. Werner, A. Delgado, The viscosity of water at high pressures–especially at subzero degrees centigrade, Rheol. Acta 39 (6) (2000) 566–573.
[229] M. Neek-Amal, F.M. Peeters, I.V. Grigorieva, A.K. Geim, Commensurability effects in viscosity of nanoconfined water, ACS Nano 10 (3) (2016) 3685–3692.
[230] H. Ye, H. Zhang, Z. Zhang, Y. Zheng, Size and temperature effects on the viscosity of water inside carbon nanotubes, Nanoscale Res. Lett. 6 (1) (2011) 87.
[231] J.S. Babu, S.P. Sathian, The role of activation energy and reduced viscosity on the enhancement of water flow through carbon nanotubes, J. Chem. Phys. 134 (19) (2011) 194509.
[232] C. Fang, X. Wu, F. Yang, R. Qiao, Flow of quasi-two dimensional water in graphene channels, J. Chem. Phys. 148 (6) (2018) 064702.
[233] J. Teixeira, J.-M. Zanotti, M.-C. Bellissent-Funel, S.-H. Chen, Water in confined geometries, Phys. B Condens. Matter 234 (1997) 370–374.
[234] U. Raviv, P. Laurat, J. Klein, Fluidity of water confined to subnanometre films, Nature 413 (6851) (2001) 51.
[235] U. Raviv, J. Klein, Fluidity of bound hydration layers, Science 297 (5586) (2002) 1540–1543.
[236] Y. Leng, P.T. Cummings, Shear dynamics of hydration layers, J. Chem. Phys. 125 (10) (2006) 104701.
[237] G.H. Findenegg, S. Jähnert, D. Akcakayiran, A. Schreiber, Freezing and melting of water confined in silica nanopores, ChemPhysChem 9 (18) (2008) 2651–2659.
[238] S. Perkin, R. Goldberg, L. Chai, N. Kampf, J. Klein, Dynamic properties of confined hydration layers, Faraday Discuss 141 (2009) 399–413.
[239] D.T. Limmer, D. Chandler, Phase diagram of supercooled water confined to hydrophilic nanopores, J. Chem. Phys. 137 (4) (2012) 044509.
[240] F.G. Alabarse, J. Haines, O. Cambon, C. Levelut, D. Bourgogne, A. Haidoux, D. Granier, B. Coasne, Freezing of water confined at the nanoscale, Phys. Rev. Lett. 109 (3) (2012) 035701.
[241] T.-D. Li, J. Gao, R. Szoszkiewicz, U. Landman, E. Riedo, Structured and viscous water in subnanometer gaps, Phys. Rev. B 75 (11) (2007) 115415.
[242] S. Romero-Vargas Castrillon, N. Giovambattista, I.A. Aksay, P.G. Debenedetti, Effect of surface polarity on the structure and dynamics of water in nanoscale confinement, J. Phys. Chem. B 113 (5) (2009) 1438–1446.
[243] C. Sendner, D. Horinek, L. Bocquet, R.R. Netz, Interfacial water at hydrophobic and hydrophilic surfaces: slip, viscosity, and diffusion, Langmuir 25 (18) (2009) 10768–10781.
[244] A.A. Milischuk, B.M. Ladanyi, Structure and dynamics of water confined in silica nanopores, J. Chem. Phys. 135 (17) (2011) 174709.
[245] R. Schmidt, E.W. Hansen, M. Stoecker, D. Akporiaye, O.H. Ellestad, Pore size determination of MCM-51 mesoporous materials by means of ^{1}H NMR spectroscopy, N_2 adsorption, and HREM. a preliminary study, J. Am. Chem. Soc. 117 (14) (1995) 4049–4056.
[246] A. Schreiber, I. Ketelsen, G.H. Findenegg, Melting and freezing of water in ordered mesoporous silica materials, Phys. Chem. Chem. Phys. 3 (7) (2001) 1185–1195.
[247] M. Sliwinska-Bartkowiak, M. Jazdzewska, L.L. Huang, K.E. Gubbins, Melting behavior of water in cylindrical pores: carbon nanotubes and silica glasses, Phys. Chem. Chem. Phys. 10 (32) (2008) 4909–4919.
[248] G. Zhao, Q. Tan, L. Xiang, D. Cai, H. Zeng, H. Yi, Z. Ni, Y. Chen, Structure and properties of water film adsorbed on mica surfaces, J. Chem. Phys. 143 (10) (2015) 104705.
[249] A. Malani, K.G. Ayappa, S. Murad, Influence of hydrophilic surface specificity on the structural properties of confined water, J. Phys. Chem. B 113 (42) (2009) 13825–13839.
[250] I. Fedyanin, A. Pertsin, M. Grunze, Quasistatic computer simulations of shear behavior of water nanoconfined between mica surfaces, J. Chem. Phys. 135 (17) (2011) 174704.
[251] J.N. Israelachvili, G.E. Adams, Measurement of forces between two mica surfaces in aqueous electrolyte solutions in the range 0–100 nm, J. Chem. Soc. Faraday. Trans. 1 74 (1978) 975–1001.
[252] R.M. Pashley, Hydration forces between mica surfaces in aqueous electrolyte solutions, J. Colloid Interface Sci. 80 (1) (1981) 153–162.
[253] R.M. Pashley, DLVO and hydration forces between mica surfaces in Li+, Na+, K+, and Cs+ electrolyte solutions: a correlation of double-layer and hydration forces with surface cation exchange properties, J. Colloid Interface Sci. 83 (2) (1981) 531–546.
[254] R.G. Horn, D.T. Smith, W. Haller, Surface forces and viscosity of water measured between silica sheets, Chem. Phys. Lett. 162 (4–5) (1989) 404–408.
[255] R.M. Pashley, J.N. Israelachvili, Molecular layering of water in thin films between mica surfaces and its relation to hydration forces, J. Colloid Interface Sci. 101 (2) (1984) 511–523.
[256] M. Acik, C. Mattevi, C. Gong, G. Lee, K. Cho, M. Chhowalla, Y.J. Chabal, The role of intercalated water in multilayered graphene oxide, ACS Nano 4 (10) (2010) 5861–5868.
[257] M. Hu, B. Mi, Enabling graphene oxide nanosheets as water separation membranes, Environ. Sci. Technol. 47 (8) (2013) 3715–3723.
[258] Q. Xu, H. Xu, J. Chen, Y. Lv, C. Dong, T.S. Sreeprasad, Graphene and graphene oxide: advanced membranes for gas separation and water purification, Inorg. Chem. Front. 2 (5) (2015) 417–424.
[259] R.R. Nair, H.A. Wu, P.N. Jayaram, I.V. Grigorieva, A.K. Geim, Unimpeded permeation of water through helium-leak–tight graphene-based membranes, Science 335 (6067) (2012) 442–444.
[260] P. Sun, M. Zhu, K. Wang, M. Zhong, J. Wei, D. Wu, Z. Xu, H. Zhu, Selective ion penetration of graphene oxide membranes, ACS Nano 7 (1) (2012) 428–437.
[261] R.K. Joshi, P. Carbone, F.-C. Wang, V.G. Kravets, Y. Su, I.V. Grigorieva, H.A. Wu, A.K. Geim, R.R. Nair, Precise and ultrafast molecular sieving through graphene oxide membranes, Science 343 (6172) (2014) 752–754.
[262] J. Shen, G. Liu, K. Huang, Z. Chu, W. Jin, N. Xu, Subnanometer two-dimensional graphene oxide channels for ultrafast gas sieving, ACS Nano 10 (3) (2016) 3398–3409.
[263] D.W. Boukhvalov, M.I. Katsnelson, Y.-W. Son, Origin of anomalous water permeation through graphene oxide membrane, Nano Lett. 13 (8) (2013) 3930–3935.
[264] H. Dai, Z. Xu, X. Yang, Water permeation and ion rejection in layer-by-layer stacked graphene oxide nanochannels: a molecular dynamics simulation, J. Phys. Chem. C 120 (39) (2016) 22585–22596.
[265] J.A.L. Willcox, H.J. Kim, Molecular dynamics study of water flow across multiple layers of pristine, oxidized, and mixed regions of graphene oxide, ACS Nano 11 (2) (2017) 2187–2193.
[266] M. Ghosh, L. Pradipkanti, V. Rai, D.K. Satapathy, P. Vayalamkuzhi, M. Jaiswal, Confined water layers in graphene oxide probed with spectroscopic ellipsometry, Appl. Phys. Lett. 106 (24) (2015) 241902.
[267] K. Erickson, R. Erni, Z. Lee, N. Alem, W. Gannett, A. Zettl, Determination of the local chemical structure of graphene oxide and reduced graphene oxide, Adv. Mater. 22 (40) (2010) 4467–4472.
[268] D. Pacilé, J.C. Meyer, A.F. Rodríguez, M. Papagno, C. Gomez-Navarro, R.S. Sundaram, M. Burghard, K. Kern, C. Carbone, U. Kaiser, Electronic properties and atomic structure of graphene oxide membranes, Carbon 49 (3) (2011) 966–972.
[269] H. He, J. Klinowski, M. Forster, A. Lerf, A new structural model for graphite oxide, Chem. Phys. Lett. 287 (1) (1998) 53–56.
[270] A.V. Talyzin, T. Hausmaninger, S. You, T. Szabó, The structure of graphene oxide membranes in liquid water, ethanol and water–ethanol mixtures, Nanoscale 6 (1) (2014) 272–281.
[271] H. Li, Z. Song, X. Zhang, Y. Huang, S. Li, Y. Mao, H.J. Ploehn, Y. Bao, M. Yu, Ultrathin, molecular-sieving graphene oxide membranes for selective hydrogen separation, Science 342 (6154) (2013) 95–98.
[272] B. Rezania, N. Severin, A.V. Talyzin, J.P. Rabe, Hydration of bilayered graphene oxide, Nano Lett. 14 (7) (2014) 3993–3998.
[273] T. Ohta, A. Bostwick, T. Seyller, K. Horn, E. Rotenberg, Controlling the electronic structure of bilayer graphene, Science 313 (5789) (2006) 951–954.
[274] F. Schedin, A.K. Geim, S.V. Morozov, E.W. Hill, P. Blake, M.I. Katsnelson, K.S. Novoselov, Detection of individual gas molecules adsorbed on graphene, Nat. Mater. 6 (2007) 652.

[275] T.O. Wehling, K.S. Novoselov, S.V. Morozov, E.E. Vdovin, M.I. Katsnelson, A.K. Geim, A.I. Lichtenstein, Molecular doping of graphene, Nano Lett. 8 (1) (2008) 173–177.

[276] H.E. Romero, N. Shen, P. Joshi, H.R. Gutierrez, S.A. Tadigadapa, J.O. Sofo, P.C. Eklund, n-type behavior of graphene supported on Si/SiO_2 substrates, ACS Nano 2 (10) (2008) 2037–2044.

[277] P.L. Levesque, S.S. Sabri, C.M. Aguirre, J. Guillemette, M. Siaj, P. Desjardins, T. Szkopek, R. Martel, Probing charge transfer at surfaces using graphene transistors, Nano Lett. 11 (1) (2011) 132–137.

[278] S. Schumacher, T.O. Wehling, P. Lazić, S. Runte, D.F. Förster, C. Busse, M. Petrović, M. Kralj, S. Blügel, N. Atodiresei, V. Caciuc, T. Michely, The backside of graphene: manipulating adsorption by intercalation, Nano Lett. 13 (11) (2013) 5013–5019.

[279] T. Tsukamoto, K. Yamazaki, H. Komurasaki, T. Ogino, Effects of surface chemistry of substrates on Raman spectra in graphene, J. Phys. Chem. C 116 (7) (2012) 4732–4737.

[280] S. Tongay, J. Suh, C. Ataca, W. Fan, A. Luce, J.S. Kang, J. Liu, C. Ko, R. Raghunathanan, J. Zhou, F. Ogletree, J. Li, J.C. Grossman, J. Wu, Defects activated photoluminescence in two-dimensional semiconductors: interplay between bound, charged, and free excitons, Sci. Rep. 3 (2013) 2657.

[281] M. Bernardi, C. Ataca, M. Palummo, J.C. Grossman, Optical and electronic properties of two-dimensional layered materials, Nanophotonics 6 (2) (2017) 479–493.

[282] W. Kim, A. Javey, O. Vermesh, Q. Wang, Y. Li, H. Dai, Hysteresis caused by water molecules in carbon nanotube field-effect transistors, Nano Lett. 3 (2) (2003) 193–198.

[283] O. Leenaerts, B. Partoens, F.M. Peeters, Adsorption of H_2O, NH_3, CO, NO_2, and NO on graphene: a first-principles study, Phys. Rev. B 77 (12) (2008) 125416.

[284] O. Leenaerts, B. Partoens, F.M. Peeters, Water on graphene: hydrophobicity and dipole moment using density functional theory, Phys. Rev. B: Condens. Matter 79 (23) (2009) 235440.

[285] T. Wehling, M. Katsnelson, A. Lichtenstein, Adsorbates on graphene: impurity states and electron scattering, Chem. Phys. Lett. 476 (4) (2009) 125–134.

[286] M. Lafkioti, B. Krauss, T. Lohmann, U. Zschieschang, H. Klauk, K. v. Klitzing, J.H. Smet, Graphene on a hydrophobic substrate: doping reduction and hysteresis suppression under ambient conditions, Nano Lett. 10 (4) (2010) 1149–1153.

[287] T. Koyama, T. Inaba, K. Komatsu, S. Moriyama, M. Shimizu, Y. Homma, Effect of interfacial water formed between graphene and SiO_2/Si substrate, Appl. Phys. Express 10 (7) (2017) 075102.

[288] K. Nagashio, T. Yamashita, T. Nishimura, K. Kita, A. Toriumi, Electrical transport properties of graphene on SiO_2 with specific surface structures, J. Appl. Phys. 110 (2) (2011) 024513.

[289] T.R.J. Bollmann, L.Y. Antipina, M. Temmen, M. Reichling, P.B. Sorokin, Hole-doping of mechanically exfoliated graphene by confined hydration layers, Nano Res. 8 (9) (2015) 3020–3026.

[290] J. Moser, A. Verdaguer, D. Jiménez, A. Barreiro, A. Bachtold, The environment of graphene probed by electrostatic force microscopy, Appl. Phys. Lett. 92 (12) (2008) 123507.

[291] B. Kleine Bussmann, O. Ochedowski, M. Schleberger, Doping of graphene exfoliated on $SrTiO_3$, Nanotechnology 22 (2011) 265703.

[292] Y. Pascal-Levy, E. Shifman, M. Pal-Chowdhury, E.M. Hajaj, O. Shtempluck, A. Razin, V. Kochetkov, Y.E. Yaish, Gate-induced modification of water adsorption on dielectrics probed by EFM and carbon nanotube FETs, ChemPhysChem 13 (18) (2012) 4202–4206.

[293] T. Gowthami, G. Tamilselvi, G. Jacob, G. Raina, The role of ambient ice-like water adlayers formed at the interfaces of graphene on hydrophobic and hydrophilic substrates probed using scanning probe microscopy, Phys. Chem. Chem. Phys. 17 (2015) 13964–13972.

[294] G.L. Hao, X. Qu, J. Li, L.W. Yang, L.L. Yin, F. Lu, J.X. Zhong, Surface potentials of few-layer graphene films in high vacuum and ambient conditions, Solid State Commun. 151 (2011) 818.

[295] S.J. Goncher, L. Zhao, A.N. Pasupathy, G.W. Flynn, Substrate level control of the local doping in graphene, Nano Lett. 13 (4) (2013) 1386–1392.

[296] V. Frolov, P. Pivovarov, E. Zavedeev, V. Konov, Influence of laser irradiation on local electronic properties of graphene in the presence of water adsorbate, Optic Laser. Technol. 90 (2017) 216–221.

[297] H. Bluhm, T. Inoue, S. Miquel, Formation of dipole-oriented water films on mica substrates at ambient conditions, Surf. Sci. 462 (2000) L599–L602.

[298] J.H. Hwang, H. Lee, S. Kwon, J.H. Jeong, H.C. Song, J.I.J. Choi, J.Y. Park, Local conductance mapping of water-intercalated graphene on mica, Appl. Phys. Lett. 109 (24) (2016) 241602.

[299] C. Zheng, Z.-Q. Xu, Q. Zhang, M.T. Edmonds, K. Watanabe, T. Taniguchi, Q. Bao, M.S. Fuhrer, Profound effect of substrate hydroxylation and hydration on electronic and optical properties of monolayer MoS_2, Nano Lett. 15 (5) (2015) 3096–3102.

[300] J.O. Varghese, P. Agbo, A.M. Sutherland, V.W. Brar, G.R. Rossman, H.B. Gray, J.R. Heath, The influence of water on the optical properties of single-layer molybdenum disulfide, Adv. Mater. 27 (17) (2015) 2734–2740.

[301] P. Atkin, D.W.M. Lau, Q. Zhang, C. Zheng, K.J. Berean, M.R. Field, J.Z. Ou, I.S. Cole, T. Daeneke, K. Kalantar-Zadeh, Laser exposure induced alteration of WS_2 monolayers in the presence of ambient moisture, 2D Mater. 5 (1) (2018) 015013.

[302] N. Manini, G. Mistura, G. Paolicelli, E. Tosatti, A. Vanossi, Current trends in the physics of nanoscale friction, Adv. Phys.: X 2 (3) (2017) 569–590.

[303] Q. Li, C. Lee, R.W. Carpick, J. Hone, Substrate effect on thickness-dependent friction on graphene, Phys. Status Solidi B 247 (11–12) (2010) 2909–2914.

[304] D. Berman, A. Erdemir, A.V. Sumant, Graphene: a new emerging lubricant, Mater. Today 17 (1) (2014) 31–42.

[305] L. Yang, Y. Guo, D. Diao, Structure and dynamics of water confined in a graphene nanochannel under gigapascal high pressure: dependence of friction on pressure and confinement, Phys. Chem. Chem. Phys. 19 (2017) 14048–14054.

[306] D.-H. Cho, L. Wang, J.-S. Kim, G.-H. Lee, E.S. Kim, S. Lee, S.Y. Lee, J. Hone, C. Lee, Effect of surface morphology on friction of graphene on various substrates, Nanoscale 5 (2013) 3063–3069.

[307] A.S. de Wijn, L.G.M. Pettersson, How square ice helps lubrication, Phys. Rev. B 95 (16) (2017) 165433.

[308] W. Gao, A. Tkatchenko, Sliding mechanisms in multilayered hexagonal boron nitride and graphene: the effects of directionality, thickness, and sliding constraints, Phys. Rev. Lett. 114 (9) (2015) 096101.

[309] G. Paolicelli, M. Tripathi, V. Corradini, A. Candini, S. Valeri, Nanoscale frictional behavior of graphene on SiO_2 and Ni(111) substrates, Nanotechnology 26 (5) (2015) 055703.

[310] K. Falk, F. Sedlmeier, L. Joly, R.R. Netz, L. Bocquet, Molecular origin of fast water transport in carbon nanotube membranes: superlubricity versus curvature dependent friction, Nano Lett. 10 (10) (2010) 4067–4073.

[311] G. Tocci, L. Joly, A. Michaelides, Friction of water on graphene and hexagonal boron nitride from Ab initio methods: very different slippage despite very similar interface structures, Nano Lett. 14 (12) (2014) 6872–6877.

[312] W. Xiong, J.Z. Liu, M. Ma, Z. Xu, J. Sheridan, Q. Zheng, Strain engineering water transport in graphene nanochannels, Phys. Rev. E 84 (5) (2011) 056329.

[313] J. Lee, M. Atmeh, D. Berman, Effect of trapped water on the frictional behavior of graphene oxide layers sliding in water environment, Carbon 120 (2017) 11–16.

[314] H. Cai, Y. Guo, W. Guo, Friction induced structural transformations of water monolayers at graphene/Cu interfaces, Phys. Chem. Chem. Phys. 20 (2018) 4137–4143.

[315] M. Paliy, O.M. Braun, S. Consta, The friction properties of an ultrathin confined water film, Tribol. Lett. 23 (2006) 7–14.

[316] H. Lee, J.-H. Ko, J.S. Choi, J.H. Hwang, Y.-H. Kim, M. Salmeron, J.Y. Park, Enhancement of friction by water intercalated between graphene and mica, J. Phys. Chem. Lett. 8 (15) (2017) 3482–3487.

[317] H. Lee, J.-H. Ko, H.C. Song, M. Salmeron, Y.-H. Kim, J.Y. Park, Isotope- and thickness-dependent friction of water layers intercalated between graphene and mica, Tribol. Lett. 66 (2018) 36.

[318] K. Morgenstern, K.-H. Rieder, Dissociation of water molecules with the scanning tunnelling microscope, Chem. Phys. Lett. 358 (2002) 250–256.

[319] M. Mehlhorn, H. Gawronski, K. Morgenstern, Electron damage to supported ice investigated by scanning tunneling microscopy and spectroscopy, Phys. Rev. Lett. 101 (2008) 196101.

[320] M. Cheng, D. Wang, Z. Sun, J. Zhao, R. Yang, G. Wang, W. Yang, G. Xie, J. Zhang, P. Chen, C. He, D. Liu, L. Xu, D. Shi, E. Wang, G. Zhang, A route toward digital manipulation of water nanodroplets on surfaces, ACS Nano 8 (4) (2014) 3955–3960.

[321] N. Choudhury, B.M. Pettitt, On the mechanism of hydrophobic association of nanoscopic solutes, J. Am. Chem. Soc. 127 (10) (2005) 3556–3567.

[322] S.F. Braga, V.R. Coluci, S.B. Legoas, R. Giro, D.S. Galvão, R.H. Baughman, Structure and dynamics of carbon nanoscrolls, Nano Lett. 4 (5) (2004) 881–884.

[323] S.P. Surwade, S.N. Smirnov, I.V. Vlassiouk, R.R. Unocic, G.M. Veith, S. Dai, S.M. Mahurin, Water desalination using nanoporous single-layer graphene, Nat. Nanotechnol. 10 (5) (2015) 459–464.

[324] D. Cohen-Tanugi, J.C. Grossman, Water desalination across nanoporous graphene, Nano Lett. 12 (7) (2012) 3602–3608.

[325] S.C. O'Hern, M.S.H. Boutilier, J.-C. Idrobo, Y. Song, J. Kong, T. Laoui, M. Atieh, R. Karnik, Selective ionic transport through tunable subnanometer pores in single-layer graphene membranes, Nano Lett. 14 (3) (2014) 1234–1241.

[326] S.C. O'Hern, D. Jang, S. Bose, J.-C. Idrobo, Y. Song, T. Laoui, J. Kong, R. Karnik, Nanofiltration across defect-sealed nanoporous monolayer graphene, Nano Lett. 15 (5) (2015) 3254–3260.

[327] S.C. O'Hern, C.A. Stewart, M.S.H. Boutilier, J.-C. Idrobo, S. Bhaviripudi, S.K. Das, J. Kong, T. Laoui, M. Atieh, R. Karnik, Selective molecular transport through intrinsic defects in a single layer of CVD graphene, ACS Nano 6 (11) (2012) 10130–10138.

[328] R.R. Nair, H.A. Wu, P.N. Jayaram, I.V. Grigorieva, A.K. Geim, Unimpeded permeation of water through helium-leak–tight graphene-based membranes, Science 335 (6067) (2012) 442–444.

[329] B. Mi, Graphene oxide membranes for ionic and molecular sieving, Science 343 (6172) (2014) 740–742.

[330] H. Liu, H. Wang, X. Zhang, Facile fabrication of freestanding ultrathin reduced graphene oxide membranes for water purification, Adv. Mater. 27 (2) (2014) 249–254.

[331] J. Abraham, K.S. Vasu, C.D. Williams, K. Gopinadhan, Y. Su, C.T. Cherian, J. Dix, E. Prestat, S.J. Haigh, I.V. Grigorieva, et al., Tunable sieving of ions using graphene oxide membranes, Nat. Nanotechnol. 12 (6) (2017) 546.

[332] J.R. Werber, C.O. Osuji, M. Elimelech, Materials for next-generation desalination and water purification membranes, Nat. Rev. Mat. 1 (5) (2016) 16018.

[333] J. Feng, M. Graf, K. Liu, D. Ovchinnikov, D. Dumcenco, M. Heiranian, V. Nandigana, N.R. Aluru, A. Kis, A. Radenovic, Single-layer MoS_2 nanopores as nanopower generators, Nature 536 (7615) (2016) 197.

[334] M.I. Walker, K. Ubych, V. Saraswat, E.A. Chalklen, P. Braeuninger-Weimer, S. Caneva, R.S. Weatherup, S. Hofmann, U.F. Keyser, Extrinsic cation selectivity of 2D membranes, ACS Nano 11 (2) (2017) 1340–1346.

[335] A. Siria, P. Poncharal, A.-L. Biance, R. Fulcrand, X. Blase, S.T. Purcell, L. Bocquet, Giant osmotic energy conversion measured in a single transmembrane boron nitride nanotube, Nature 494 (7438) (2013) 455.
[336] A. Siria, M.-L. Bocquet, L. Bocquet, New avenues for the large-scale harvesting of blue energy, Nat. Rev. Chem. 1 (11) (2017) 0091.
[337] C.H.Y.X. Lim, A. Sorkin, Q. Bao, A. Li, K. Zhang, M. Nesladek, K.P. Loh, A hydrothermal anvil made of graphene nanobubbles on diamond, Nat. Commun. 4 (2013) 1556.
[338] C.H.Y.X. Lim, M. Nesladek, K.P. Loh, Observing high-pressure chemistry in graphene bubbles, Angew. Chem. Int. Ed. 53 (1) (2014) 215–219.
[339] A. Kayal, A. Chandra, Infrared spectral and dynamical properties of water confined in nanobubbles at hybrid interfaces of diamond and graphene: a molecular dynamics study, J. Phys. Chem. C 121 (42) (2017) 23455–23462.
[340] E. Dollekamp, P. Bampoulis, B. Poelsema, H.J.W. Zandvliet, E.S. Kooij, Electrochemically induced nanobubbles between graphene and mica, Langmuir 32 (26) (2016) 6582–6590.
[341] H. An, B.H. Tan, J.G.S. Moo, S. Liu, M. Pumera, C.-D. Ohl, Graphene nanobubbles produced by water splitting, Nano Lett. 17 (5) (2017) 2833–2838.
[342] D. Shin, J.B. Park, Y.-J. Kim, S.J. Kim, J.H. Kang, B. Lee, S.-P. Cho, B.H. Hong, K.S. Novoselov, Growth dynamics and gas transport mechanism of nanobubbles in graphene liquid cells, Nat. Commun. 6 (2015) 6068.
[343] J.B. Park, D. Shin, S. Kang, S.-P. Cho, B.H. Hong, Distortion in two-dimensional shapes of merging nanobubbles: evidence for anisotropic gas flow mechanism, Langmuir 32 (43) (2016) 11303–11308.
[344] Q. Chen, J.M. Smith, J. Park, K. Kim, D. Ho, H.I. Rasool, A. Zettl, A.P. Alivisatos, 3D motion of DNA-Au nanoconjugates in graphene liquid cell electron microscopy, Nano Lett. 13 (9) (2013) 4556–4561.
[345] C.-M. Seah, B. Vigolo, S.-P. Chai, A.R. Mohamed, Transfer of wafer-scale graphene onto arbitrary substrates: the steps towards the reuse and recycle of the catalyst, 2D Mater. 5 (4) (2018) 042001.
[346] G.F. Schneider, V.E. Calado, H. Zandbergen, L.M.K. Vandersypen, C. Dekker, Wedging transfer of nanostructures, Nano Lett. 10 (5) (2010) 1912–1916.
[347] A. Gurarslan, Y. Yu, L. Su, Y. Yu, F. Suarez, S. Yao, Y. Zhu, M. Ozturk, Y. Zhang, L. Cao, Surface-energy-assisted perfect transfer of centimeter-scale monolayer and few-layer MoS_2 films onto arbitrary substrates, ACS Nano 8 (11) (2014) 11522–11528.
[348] Y. Wang, Y. Zheng, X. Xu, E. Dubuisson, Q. Bao, J. Lu, K.P. Loh, Electrochemical delamination of CVD-grown graphene film: toward the recyclable use of copper catalyst, ACS Nano 5 (12) (2011) 9927–9933.
[349] L. Gao, W. Ren, H. Xu, L. Jin, Z. Wang, T. Ma, L.-P. Ma, Z. Zhang, Q. Fu, L.-M. Peng, Repeated growth and bubbling transfer of graphene with millimetre-size single-crystal grains using platinum, Nat. Commun. 3 (2012) 699.
[350] E. Koren, E. Sutter, S. Bliznakov, F. Ivars-Barcelo, P. Sutter, Isolation of high quality graphene from Ru by solution phase intercalation, Appl. Phys. Lett. 103 (12) (2013) 121602.
[351] G. Kim, A.-R. Jang, H.Y. Jeong, Z. Lee, D.J. Kang, H.S. Shin, Growth of high-crystalline, single-layer hexagonal boron nitride on recyclable platinum foil, Nano Lett. 13 (4) (2013) 1834–1839.
[352] Y. Gao, W. Ren, T. Ma, Z. Liu, Y. Zhang, W.-B. Liu, L.-P. Ma, X. Ma, H.-M. Cheng, Repeated and controlled growth of monolayer, bilayer and few-layer hexagonal boron nitride on Pt foils, ACS Nano 7 (6) (2013) 5199–5206.
[353] P. Gupta, P.D. Dongare, S. Grover, S. Dubey, H. Mamgain, A. Bhattacharya, M.M. Deshmukh, A facile process for soak-and-peel delamination of CVD graphene from substrates using water, Sci. Rep. 4 (2014) 3882.
[354] K. Verguts, K. Schouteden, C.-H. Wu, L. Peters, N. Vrancken, X. Wu, Z. Li, M. Erkens, C. Porret, C. Huyghebaert, C. Van Haesendonck, S. De Gendt, S. Brems, Controlling water intercalation is key to a direct graphene transfer, ACS Appl. Mater. Interfaces 9 (42) (2017) 37484–37492.
[355] E. Dollekamp, P. Bampoulis, D.P. Faasen, H.J.W. Zandvliet, E.S. Kooij, Charge induced dynamics of water in a graphene-mica slit pore, Langmuir 33 (43) (2017) 11977–11985.
[356] K. Verguts, J. Coroa, C. Huyghebaert, S. De Gendt, S. Brems, Graphene delamination using 'electrochemical methods': an ion intercalation effect, Nanoscale 10 (12) (2018) 5515–5521.
[357] V. Nicolosi, M. Chhowalla, M.G. Kanatzidis, M.S. Strano, J.N. Coleman, Liquid exfoliation of layered materials, Science 340 (6139) (2013) 1226419.
[358] D.R. Dreyer, S. Park, C.W. Bielawski, R.S. Ruoff, The chemistry of graphene oxide, Chem. Soc. Rev. 39 (1) (2010) 228–240.
[359] C.-J. Shih, A. Vijayaraghavan, R. Krishnan, R. Sharma, J.-H. Han, M.-H. Ham, Z. Jin, S. Lin, G.L. Paulus, N.F. Reuel, Q. Hua Wang, D. Blankschtein, M.S. Strano, Bi-and trilayer graphene solutions, Nat. Nanotechnol. 6 (7) (2011) 439.
[360] G. Eda, H. Yamaguchi, D. Voiry, T. Fujita, M. Chen, M. Chhowalla, Photoluminescence from chemically exfoliated MoS_2, Nano Lett. 11 (12) (2011) 5111–5116.
[361] Y.A. Nikitin, M.L. Pyatkovskii, Formation and properties of materials based on thermally expanded graphite, Powder Metall. Metal. C+ 36 (1) (1997) 41–45.
[362] R. Ma, T. Sasaki, Nanosheets of oxides and hydroxides: ultimate 2D charge bearing functional crystallites, Adv. Mater. 22 (45) (2010) 5082–5104.
[363] Y. Hernandez, V. Nicolosi, M. Lotya, F.M. Blighe, Z. Sun, S. De, I.T. McGovern, B. Holland, M. Byrne, Y.K. Gun'Ko, J.J. Boland, P. Niraj, G. Duesberg, S. Krishnamurthy, R. Goodhue, J. Hutchison, V. Scardaci, A.C. Ferrari, J.N. Coleman, High-yield production of graphene by liquid-phase exfoliation of graphite, Nat. Nanotechnol. 3 (9) (2008) 563–568.
[364] J.N. Coleman, M. Lotya, A. O'Neill, S.D. Bergin, P.J. King, U. Khan, K. Young, A. Gaucher, S. De, R.J. Smith, I.V. Shvets, S.K. Arora, G. Stanton, H.-Y. Kim, K. Lee, G.T. Kim, G.S. Duesberg, T. Hallam, J.J. Boland, J.J. Wang, J.F. Donegan, J.C. Grunlan, G. Moriarty, A. Shmeliov, R.J. Nicholls, J.M. Perkins, E.M. Grieveson, K. Theuwissen, D.W. McComb, P.D. Nellist, V. Nicolosi, Two-dimensional nanosheets produced by liquid exfoliation of layered materials, Science 331 (6017) (2011) 568–571.
[365] C.-Y. Su, A.-Y. Lu, Y. Xu, F.-R. Chen, A.N. Khlobystov, L.-J. Li, High-quality thin graphene films from fast electrochemical exfoliation, ACS Nano 5 (3) (2011) 2332–2339.
[366] Z.Y. Xia, S. Pezzini, E. Treossi, G. Giambastiani, F. Corticelli, V. Morandi, A. Zanelli, V. Bellani, V. Palermo, The exfoliation of graphene in liquids by electrochemical, chemical, and sonication assisted techniques: a nanoscale study, Adv. Funct. Mater. 23 (37) (2013) 4684–4693.